Quantitative characterisation of a blocky peperite: 2D image analysis of clast shape and distribution in an andesite sill at Honister, Cumbria

Aidan Robinson

Supervised by Prof Hugh Tuffen and Dr Thomas Jones

This thesis is submitted for the degree of MSc by Research in Environmental Science

Lancaster Environment Centre
Lancaster University
December 2025

Quantitative characterisation of a blocky peperite: 2D image analysis of clast shape and distribution in an andesite sill at Honister, Cumbria

Aidan Robinson

Abstract

Peperites record complex interactions between magma and wet sediments that are fundamental to hydromagmatic volcanism. However, interpretations of these processes have historically been limited by a reliance on qualitative field descriptions. We present the first quantification of clast shape and distribution in a peperite exposure, applying a novel morphometric approach to a well-exposed upper margin of a peperitic andesite sill at Honister, Cumbria, England. Here, blocky peperite formed where magma intruded and mingled with a wet and unconsolidated volcaniclastic sediment during the Ordovician volcanism that formed the Borrowdale Volcanic Group. We applied Structure-from-Motion photogrammetry to create a high-resolution 2D image of the exposure, enabling outcrop-scale quantification of clast characteristics through image analysis. Based on our field observations and a complementary dataset of clast morphological and textural characteristics, we identify four syn-magmatic processes governing peperite formation at Hopper Quarry: (1) shallow emplacement of poorly vesicular magma into wet, unconsolidated sediment, with magma propagation accommodated by non-brittle processes and the formation of a vapour film at the interface, as evidenced by fluidisation cross-cutting undisturbed sediment; (2) localised vesiculation of the sill margin driven by a volatile saturation gradient at the magma-wet sediment interface, recorded by heterogenous clast vesicularity unrelated to clast dimensions; (3) brittle cooling-contraction granulation of the sill margin, forming an initial population of closely-packed blocky, in situ clasts characterised by angular margins and jigsaw-fit arrangements, with fine fragmentation driven by localised instabilities of the vapour film; (4) clast dispersion driven by fluidisation of the host sediment and bulk magma-sediment density contrasts, producing a transition from framework-supported to matrix-supported clast domains with distance from the sill. A quantitative baseline for blocky peperite clast shape and distribution has been established here, providing abundant scope for comparison with a broader suite of peperites and blocky lavas.

Acknowledgments

I would like to start with a huge thank you to my supervisors, Hugh Tuffen and Thomas Jones, for the opportunity to undertake this project, their support throughout, and for helping me reach my next steps. I owe a great deal to Hugh for his expertise and guidance on the geology - and our many discussions on the volcanology of various holiday destinations. Equally, I owe many thanks to Thomas, not only for his support on my project, but for invaluable mentorship regarding my next steps and help with the many applications for my future ambitions. Beyond the volcanology, I really feel I've learnt and grown a lot through all the experiences offered to me this year.

Thanks to the team at Honister Slate Mine for access to the quarries and providing an exciting impromptu tour of the working mine. I am also grateful for the technical guidance provided by Mike James through our discussions on photogrammetry and methodologies.

And of course, a huge thank you to the volcanology group here at Lancaster – not only for the supportive academic community but for the lunchtime crosswords, pub quizzes, and Lake District hikes. They have been welcoming and made me feel a part of the team from the start. I owe a special thanks to Natalia Lipiejko for connecting me with my prospective PhD supervisor in New Zealand, an opportunity I never imagined pursuing at the start of the year.

Equally, a great thank you to my parents for supporting my time in Lancaster, the encouragement, and for believing in my ambitions.

Last but certainly not least, I would like to thank my examiners, Mike Branney and Steve Lane, for their time reading my work and for our engaging discussions during my viva.

Declaration

I declare that, except where the contribution of others is specified, this thesis is to the best of my knowledge original and my own work. It has not been submitted for any other degree or professional qualification elsewhere.

The word count for this thesis is **21529**. Excluded from the word count are the title page, abstract, acknowledgements, declaration, contents, references, and appendices.

Aidan Robinson
19th December 2025

Contents

Chapter 1

Introduction

This introductory chapter presents the motivation for this research, identifies key research objectives based on the literature review provided in Chapter 2, and provides a summary of every chapter in the thesis.

1.1 Motivation and scope of the research

Interaction between magma and unconsolidated, wet sediments commonly forms a volcaniclastic rock termed peperite. This rock consists of igneous material originating directly from the magma, termed juvenile clasts, mingled within a sedimentary host. Peperite deposits provide a frozen record of the numerous dynamic and often simultaneous processes involved in their genesis, including fragmentation of the magma, fluidisation of the host sediment, and magma-sediment mingling. Therefore, the description and interpretation of peperite morphologies and textures provide important insights into these genetic processes, as well as to broader themes of magma-water interaction and the mixing mechanisms that precede explosive hydrovolcanic eruptions (Skilling et al. 2002).

Peperite is exposed in Ordovician rock (~455 Ma) on quarry faces at Honister, Cumbria. Here, andesite sills intruded reworked volcaniclastic sediments deposited in a lacustrine environment (Suthren 1977; Petterson et al. 1992; Millward 2004b). As fully discussed within my literature review (Chapter 2), several questions arise from the morphological, textural, and spatial features visible within the Honister peperite. Key features of interest include clast size and shape, which inform our understanding of fragmentation processes and clast evolution; variations in clast vesicularity, which provide a chronology of volatile exsolution; and clast dispersal across the exposure, which offers insights into the timing and degree of mixing between magmtic fragments and sediment. Ultimately, the sizes, shapes, and spatial arrangements of clasts and vesicles can be linked to the physical processes that drive peperite genesis.

Similar features and relationships have been observed across a number of peperite exposures worldwide (e.g., Busby-Spera and White 1987; Brooks 1995; Hanson and Hargrove 1999; Martin and Nemeth 2007). Formation mechanisms have been inferred though detailed qualitative geological surveys of these sites, including interpretations of the peperite exposures at Honister (Branney and Suthren 1988). However, no focus has been placed on the quantitative analysis of peperite. This is despite numerical analysis being a frequent and valuable aspect of understanding the origin and evolution of other volcanic products, especially pyroclasts, over the past three

decades (e.g., Dellino and La Volpe 1996; Maria and Carey 2002; Alfano et al. 2011; Dürig et al. 2018). Consequently, a research gap - the quantitative analysis of peperite morphologies and textures - presents itself not only at Honister, but in general across all studies of peperite. This study aims to address this gap, demonstrating that this is not a limitation of technology, but rather its absence of application to clast-scale data.

1.2 Research objectives

The primary aim of this research is to enhance the understanding of peperite genesis through reconstruction of the peperite formation processes at Honister, Cumbria. Alongside the geological interpretation, a central aspect of this thesis is the application of quantitative techniques to peperite studies, moving beyond traditional qualitative techniques. Through image processing techniques and subsequent numerical analysis, this research focuses on quantifying peperite morphologies, textures, and the overarching spatial relationships observed at Honister. Subsequently, these data are used in conjunction with geological interpretations to constrain the physical processes involved in peperite genesis. The following objectives have been identified to support the overarching thesis aim.

1. **Quantification of clast shape**
   Quantify the variability of juvenile clast shape using morphometric techniques, enabling systematic comparison between individual clasts and clast populations, and relating clast shape to primary fragmentation mechanisms.
2. **Spatial trends of clast shape**
   Investigate how juvenile clast morphologies vary spatially both with respect to the sill margin and within local clast clusters, in order to assess the dispersion and mingling dynamics associated with peperite formation.
3. **Association of juvenile clast shape and spatial trends with fragmentation mechanism**
   Relate juvenile clast morphologies and spatial trends to specific fragmentation mechanisms, to constrain the fragmentation processes responsible for peperite formation.
4. **Characterisation of clast vesicles**
   Characterise the size, shape, and distribution of vesicles in juvenile clasts across the peperite exposure to inform on the magma properties at the point of fragmentation.

1.3 Thesis outline

This thesis is composed of 6 chapters, including this introductory chapter (Chapter 1). The following chapters are outlined as follows.

Chapter 2 ***Literature review*** defines peperite, discusses the physical processes related to peperite formation, examines methodologies for analysing volcanic products, reviews current knowledge on peperite morphologies and formations mechanisms, and concludes with a geological background to the specific field site at Honister.

Chapter 3 ***Methodology*** provides a detailed methodology for the field photography and subsequent digital image analysis employed to study peperite clast and vesicle morphometry.

Chapter 4 ***Results*** first presents qualitative field observations from Hopper Quarry, Honister, providing a contextual basis for the following numerical results of juvenile clast morphology and vesicle texture. The chapter finishes with the composition of an andesite sample from Hopper Quarry, alongside estimates of viscosity at the time of intrusion.

Chapter 5 ***Discussion*** reconstructs the processes of peperite genesis at Hopper Quarry by combining morphological and textural field evidence with the quantitative dataset. This chapter also evaluates the application and implications of applying quantitative morphometric techniques to peperite studies.

Chapter 6 ***Conclusions*** summarises the findings and significance of this study and my thoughts on future work in this field.

Chapter 2

Literature review

2.1 What is peperite?

Magmatic intrusions are typically described as bodies of magma emplaced into lithified and cohesive country rock. However, in the case of a high-level intrusion, the magma may enter wet, unconsolidated sediments. In this environment, interaction between magma and wet sediments can form a volcaniclastic rock termed peperite.

Peperite consists of juvenile clasts, which are fragments of igneous material originating directly from the magma, mingled with a sedimentary host (Figure 2.1). Magma-wet sediment interactions are abundant where volcanism coincides with the deposition of thick sedimentary sequences. This is especially common in subaqueous environments located along volcanic arcs (e.g., Hanson and Hargrove 1999), where intrusions interact with unlithified volcanogenic sediments. Peperite can, however, occur in any setting where magma and unconsolidated, wet sediments interact, with previous work showing an abundant range of geological settings, compositions, and sediment types (Figure 2.2). Examples of peperite have been described, and their formation mechanisms inferred, at many localities worldwide (e.g., Busby-Spera and White 1987; Branney and Suthren 1988; Kano 1989; Hanson and Wilson 1993; Brooks 1995; Goto and McPhie 1996; Hanson and Hargrove 1999; Doyle 2000; Dadd and Van Wagoner 2002; Donaire et al. 2002; Martin and Nemeth 2007; Chen et al. 2013).

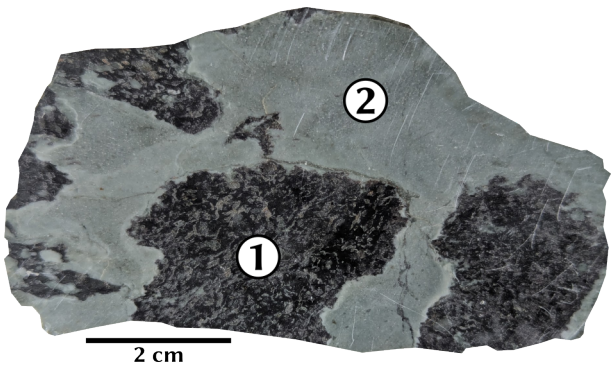

Figure 2.1 Polished hand specimen of peperite from Honister, Cumbria, showing juvenile igneous material **(1)** within a sedimentary host **(2)**.

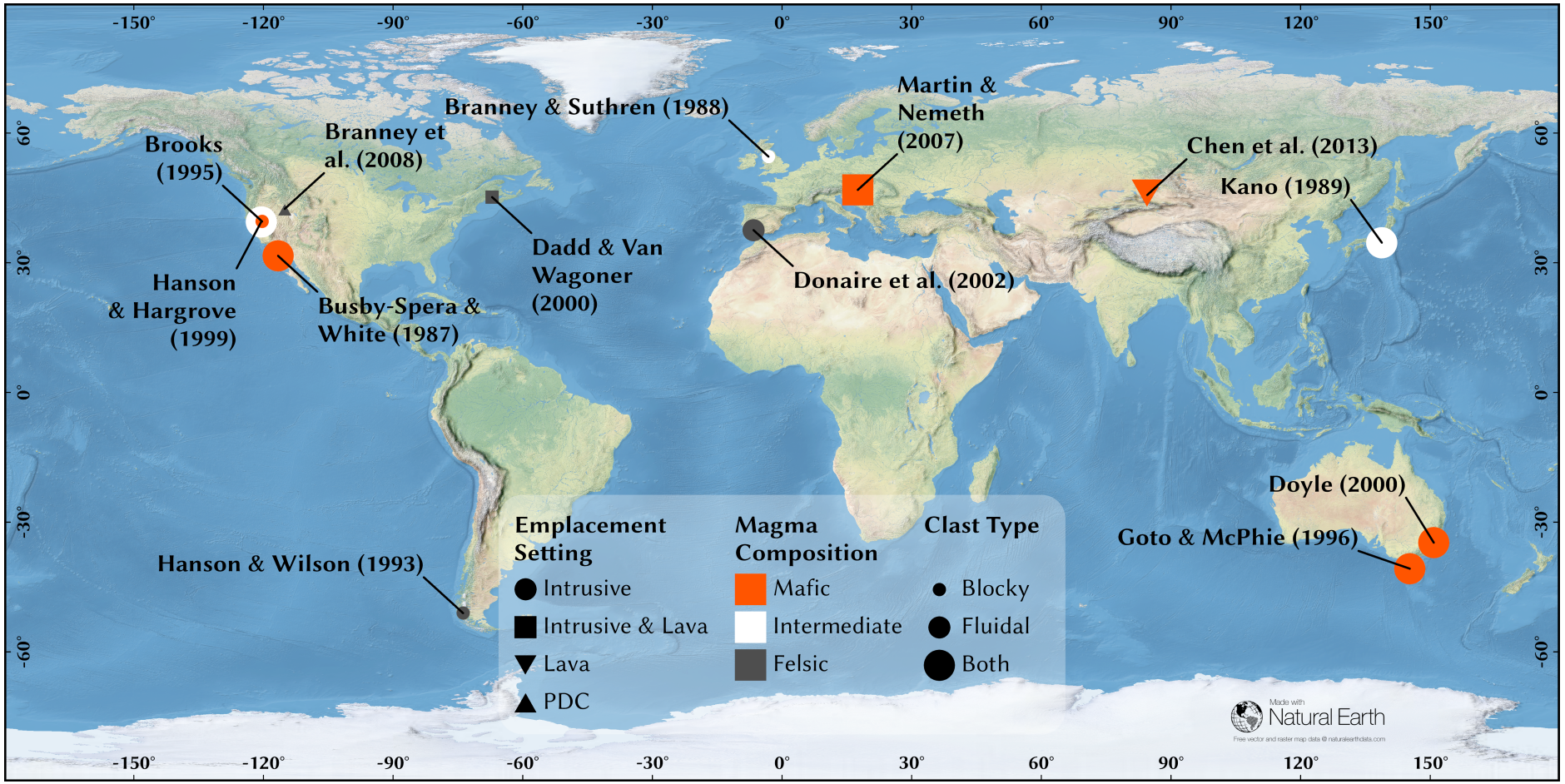

Figure 2.2 Map of reviewed peperite localities showing a global distribution and variation in emplacement setting, magma composition, and morphology.

Peperites were established in the literature in the early 19th century by George P. Scrope, who used the term peperino to describe a clastic rock composed of basalt fragments cemented in a limestone matrix (Scrope 1827). The name refers to a texture reminiscent of ground pepper. Since then, the term *peperite* has been defined both descriptively, based on its physical characteristics, and genetically, in terms of its formation. A descriptive definition of peperite refers to any rock comprising a mixture of sedimentary and igneous components. However, it is argued that suitable descriptive terms for such rocks already exist, and that *peperite* should be reserved to identify magma/sediment facies formed through a specific set of criteria. Scrope (1858) interpreted the formation of peperites as "a violent and intimate union" of the igneous and sedimentary components "while yet in a soft state", first hinting at peperite's origin of magma interaction with unconsolidated or poorly consolidated sediments. A contemporary and widely recognised definition by White et al. (2000) defines *peperite* in a genetic sense as:

> **peperite:** "a rock formed essentially in situ by disintegration of magma intruding and mingling with unconsolidated or poorly consolidated, typically wet sediment"

While the majority of literature describes peperites on the margins of intrusions, similar occurrences have been reported at the contacts of domes, lava flows, and pyroclastic density currents (PDCs). Where lava has flowed over or locally burrowed into underlying wet sediments, peperites are described to have formed by the same processes as their intrusive counterparts (Dadd and Van Wagoner 2002; Chen et al. 2013). Peperites that develop at the base of PDC deposits are termed *ignimbrite peperites* (Branney et al. 2008). Peperite-like textures have also been observed in the absence of water, where lava has dynamically interacted with unconsolidated aeolian sands (Jerram and Stollhofen 2002). It is argued that the distinctive textures resulting from magma-sediment interactions are what makes peperite unique. Hence, Jerram and Stollhofen (2002) use the term *peperite* to describe deposits of juvenile clasts mixed with sediment. Additionally, questions arise regarding whether peperite formation strictly requires unconsolidated sediment, or if water-saturated lithified or partially lithified rock may also serve as a host. Peperite has been described to form in coal, which possesses physical characteristics distinct from most documented peperite hosts. In this environment, disaggregation of the coal during magma intrusion forms a coal-water slurry allowing mingling with the magma (McClintock and White 2002). This thesis follows the genetic definition offered by White et al. (2000), while acknowledging that the unconsolidated nature of the host volcaniclastic sediment may be a product of the intrusion process itself.

The description and interpretation of peperite field examples is fundamental for reconstructing the complex subsurface interactions of many volcanic systems. Peperites provide a "frozen" record of processes that are otherwise impossible to observe directly, such as those which may occur during the initial stages of hazardous, explosive hydrovolcanism (Kokelaar 1983; Wohletz 1986; Skilling et al. 2002). Specifically, certain types of peperite are described as natural records of molten fuel coolant interactions (MFCIs) that may precede phreatomagmatic eruptions (Kokelaar 1986; White 1996; Hanson and Hargrove 1999). Additionally, the recognition of peperite in the rock record provides valuable insights into the chronology of magmatism and sedimentation through their overall morphologies, clast textures, and spatial relationships (Busby-Spera and White 1987; Brooks 1995). Despite these insights, uncertainty remains regarding the transition from non-explosive passive mingling of magma and wet sediment to highly explosive scenarios. Consequently, further studies of peperite are important for a greater understanding of the processes that govern magma-wet sediment interactions; fragmentation, fluidisation, and mixing of juvenile clasts within a host sediment.

This review begins with an overview of magma fragmentation, the underpinning process of peperite genesis. This is followed by a discussion on how morphometric methods are used to infer the formation mechanisms of volcanic products, and how this framework may be applied to peperite studies. Next, the review discusses peperite morphology described in existing literature, considering both the large-scale geometry of peperite domains and small-scale characteristics of juvenile clasts. Consequently, these morphologies are related to formation mechanisms. The review closes with the geological setting of Honister, Cumbria. Here, peperite has formed from the intrusion of Ordovician andesitic sills into wet, unconsolidated volcaniclastic sediments.

2.2 Mechanisms of magma fragmentation

Magma fragmentation refers to the breakup of a contiguous volume of molten rock into discrete clasts (Gonnermann 2015). It is a process fundamental to understanding volcanic activity at all depths, with conditions under which fragmentation occurs controlling eruption styles and, importantly, hazard extent (Jones et al. 2022).

Fragmentation can occur in either a viscous (ductile fragmentation) or elastic (brittle fragmentation) deformation regime. The concept of the glass transition represents the reversible threshold at which a material's deformation regime changes from viscous to elastic behaviour (Dingwell 1996; Gonnermann 2015; Jones et al. 2022), and can be represented by a curve in temperature-time space (Figure 2.3). Below the glass transition, at high temperatures and low strain rates, magma deforms viscously. Fragmentation in this regime is governed by fluid dynamics (Jones et al. 2019). Above the glass transition, lower temperatures and higher strain rates produce an elastic response, and brittle failure will occur if the magma cannot achieve an elastic equilibrium. The timescale of this equilibrium response, termed the structural relaxation timescale, varies both among different materials and between the components of a multiphase magma (Dingwell and Webb 1989).

Fragmentation is categorised by its driving mechanism: magmatic (dry) and hydromagmatic (wet) (e.g., Wohletz 1983; Gonnermann 2015). Magmatic fragmentation occurs in the absence of external water. It is driven by internal pressures from decompression and the subsequent exsolution of magmatic volatiles from the melt as it rises. Hydromagmatic fragmentation, in contrast, results from magma interacting with external water at or near the surface of the Earth. Interaction with water can range from minor water/melt ratios to dominantly water controlled (Wohletz et al. 2013). Because these mechanisms may operate simultaneously (Gonnermann 2015), they are both relevant to peperite formation processes.

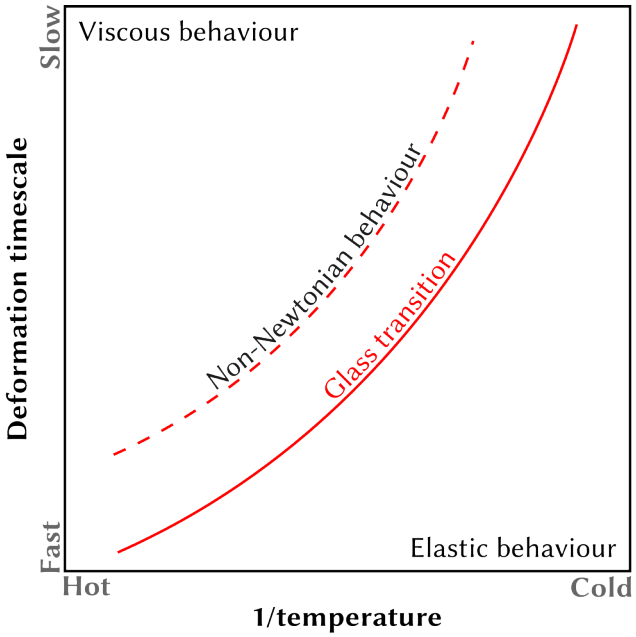

Figure 2.3 The glass transition as a function of deformation timescale and reciprocal temperature. Strain rates slower than the structural relaxation timescale allow for a viscous flow of the melt. Close to the glass transition, flow becomes non-Newtonian; the response is elastic storage at low strain rates and brittle failure at high strain rates. Based on Dingwell (1996) and Gonnermann (2015).

2.2.1 Magmatic fragmentation

Magmatic (dry) fragmentation is driven solely by the volatile component of the melt (Cashman and Scheu 2015). At depth, these magmatic gases are dissolved in the melt. On ascent, the pressure-dependent solubility of the volatiles decreases, resulting in their exsolution and diffusion into bubbles within the melt (Gonnermann 2015). Bubble growth is initially accommodated by viscous deformation of the melt. The internal pressure within the bubbles may exceed the magmatic pressure, causing overpressure. It is this overpressure of these now entrapped gases that provides the high strain rates that drive fragmentation (Figure 2.4). Overpressure is primarily associated with the rapid ascent of the magma, which allows little time for degassing. It can also be met by the rapid decompression of stationary magma through processes including unloading during edifice sector collapse, dome collapse, or plug removal (Spieler et al. 2004; Gonnermann 2015). When the force exerted by gas overpressure of the bubbles exceeds the tensile strength of the melt, bubble walls fail, and the magma is torn apart. This critical minimum pressure difference required for fragmentation is defined as the fragmentation threshold (Spieler et al. 2004). The fragmentation threshold is strongly dependent on porosity (i.e. the gas volume fraction in the melt) and permeability, with magma composition having little effect. Higher porosity magmas fragment at lower pressure differentials (Spieler et al. 2004).

If confining pressure is high enough, the exsolution of volatiles is restricted, thereby suppressing magmatic explosivity (McBirney and Murase 1970). In the context of magma-wet sediment interactions, both hydrostatic and lithostatic pressures are relevant to the overall confining pressure. Two mechanisms of magmatic fragmentation are described: (1) brittle fragmentation, and (2) fluid dynamic breakup (Gonnermann 2015).

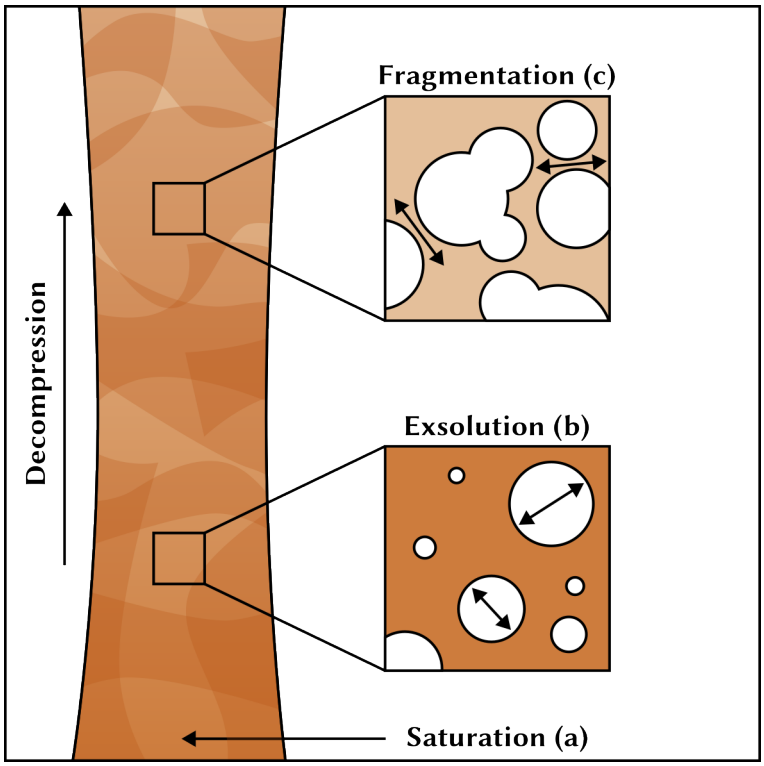

Figure 2.4 Illustration of the decompression process behind magmatic fragmentation. **(a)** Magma is saturated with dissolved volatiles at depth. **(b)** Volatiles diffuse into bubbles which grow with decreasing magma pressure. **(c)** Bubble growth and coalescence causes deformation and fragmentation of the melt.

(1) Brittle fragmentation

For high viscosity silica-rich melts, fragmentation occurs in the elastic deformation regime by crossing the glass transition (Figure 2.3) (Dingwell 1996). Close to this transition, stress may be accommodated by reversible elastic strain. However, within a highly viscous melt, resistance to bubble growth leads to excess gas pressure, and the violent release of this pressure generates high stress (Gonnermann 2015). At sufficiently high stress, large strain causes non-Newtonian behaviour as bonds within the silicate network break. Above the glass transition, structural relaxation (the elastic equilibrium response to stress) is prevented, leading to further disruption of the magma's molecular structure and causing brittle fracture (Gonnermann 2015).

(2) Fluid dynamic breakup

For lower silica, lower viscosity melts such as basalts, fragmentation via crossing the glass transition requires very high strain rates unobserved in terrestrial eruptions (Jones et al. 2019). Therefore, fragmentation of these melts must occur by a fundamentally different, non-brittle process: fluid dynamic induced breakup. This process also occurs during decompression and bubble growth, but the lower viscosity melt allows for viscous deformation, i.e. stretching and extension of the melt (Jones et al. 2019). The magma is stretched and subsequently pulled apart by hydrodynamic stresses and instabilities (Gonnermann 2015). Fluid dynamic induced breakup occurs in, but is not limited to, filament formation and extension by bubble growth and expansion, fluid dynamic instabilities at the edge of a magma jet, the bursting of bubbles at the magma's surface, and secondary fragmentation during extension within a fountain (Jones et al. 2019).

2.2.2 Hydromagmatic fragmentation

Hydromagmatic fragmentation occurs as a result of magma contacting external water. Such interactions are commonplace in Earth's environments, and drive effusive to highly explosive volcanism (Wohletz et al. 2013). Water may be present in a liquid state as groundwater, hydrothermal, sea, or lake water, or in its solid state as glacial ice (Jones et al. 2022). Such interactions fall under an umbrella of terms that are often used interchangeably, including hydrovolcanic, hydromagmatic, phreatomagmatic, and Surtseyan. Sheridan and Wohletz (1983) define hydrovolcanism as all events of magma interacting with external water, and hydromagmatism as the general processes driving these events. Hence, hydromagmatic fragmentation describes the processes of melt fragmentation when in contact with external water. Phreatomagmatic interactions occur in the phreatic zone (groundwater) and commonly refer to explosive magma-water interactions (Sheridan and Wohletz 1983; Zimanowski et al. 2015; Jones et al. 2022). Such interactions are ubiquitous with sediment (White 1996). Surtseyan eruptions are a highly explosive type of hydrovolcanism that takes place in shallow waters with rapidly rising magma (Kokelaar 1983; Colombier et al. 2019).

Water is an excellent thermodynamic working fluid, capable of efficiently converting thermal energy into mechanical energy through the production of high-pressure steam that may explosively decompress (Zimanowski et al. 2015). These interactions are commonly referred to as the natural equivalent of industrial Molten Fuel-Coolant Interactions (MFCI) (e.g., Buchanan 1974; Sheridan and Wohletz 1983; Zimanowski et al. 1991; White 1996; Wohletz 2002). MFCI, alternatively termed vapour explosions or thermal explosions (Buchanan 1974; Dullforce et al. 1976), is a phenomenon concerning the interaction between two fluids, in which the fuel (magma) has a higher temperature than the vaporisation temperature of the coolant (water). While the term MFCI is frequently reserved for violent, explosive events, in the context of magma-water interaction MFCI refers to a broader spectrum of phenomena (Wohletz 1986). This ranges from passive, non-explosive quenching by an insulating vapour film to dynamic, explosive vaporisation and expansion of the coolant. These interactions are not the result of chemical change; the energy is derived solely from the excess heat in the fuel (Dullforce et al. 1976; Zimanowski et al. 2015). Heat energy is translated into work by the expansion of the liquid coolant to the vapour phase; thus, these processes are constrained in depth by the phase behaviour of water. As pressure increases with depth, the boiling point rises until the critical point (approximately 374°C and 22 MPa). Beyond this limit, water becomes a supercritical fluid where a discrete liquid-to-vapour phase change, and associated explosive volume expansion, cannot occur (Wohletz 1986; Cas 1992).

Determining where a magma-water interaction falls on this spectrum depends on the coupling of the thermal energy to the surroundings (i.e., the heat flux). Zimanowski et al. (1991) distinguish between non-explosive interactions, involving a lower heat flux and coarse-grained fragmentation, and explosive interactions, involving a higher heat flux and fine-grained fragmentation. This critical heat flux is controlled by the presence of a thermally insulating vapour film that forms when the molten magma contacts and vaporises the water (Kokelaar 1986; White 1996). This phenomenon is known as the Leidenfrost effect or film boiling, and occurs when a high temperature difference causes almost instantaneous vaporisation of the water. Formation of this vapour film generally prevents immediate explosive interaction during this initial contact (Dullforce et al. 1976; Zimanowski et al. 1991).

In contrast, explosive interactions occur when the heat transfer is rapid due to direct contact between the melt and water, coupled with an increased surface area available for heat transfer. Initially, a high temperature difference forms a vapour film at the magma-water interface, but instability causes a cyclic process of vapour film generation and collapse on a micro to millisecond

time scale (Wohletz 1983). These oscillations result in fluid instabilities, water jet penetration of the melt, and stress waves propagating into the melt, which drives fine fragmentation (Sheridan and Wohletz 1983; Wohletz 1983; Kokelaar 1986). The dominant form of heat transfer from the melt to the water is assumed to be conductive (Wohletz 1983). Hence, extensive fragmentation promotes rapid heat transfer due to the greatly increased surface area of melt, and the short conduction path from the pyroclast interior. This causes heat transfer at a rate much greater than the vaporisation of water; the water is vaporised homogenously and its consequent expansion is explosive (Zimanowski et al. 1991). Explosive interactions may be self-perpetuating, where small scale explosions drive further fine fragmentation and mixing (Zimanowski et al. 1991).

The relative proportion of water that interacts with magma is quantified as the water-magma mass ratio (Hajimirza et al. 2022). There is an optimum mass ratio for the efficient conversion of thermal energy into mechanical energy, i.e., an explosive release of energy, termed the fragmentation efficiency. This has been theoretically suggested as between 0.3 and 0.4 (Wohletz 1986). In contrast, experimental work has shown an optimal ratio for basaltic melts as a range between 0.1 and 0.3 (Sheridan and Wohletz 1983). However, it is important to note that most work on water-magma mass ratios have used single-phase melts, and hence the added effects of bubbles and magmatic fragmentation are not accounted for (Jones et al. 2022). Additionally, this relationship assumes idealised, simultaneous mixing of the magma and water, which is limited in nature.

The extent of hydromagmatic fragmentation is governed by the conversion of thermal to mechanical energy, with the efficiency of this conversion controlled by the magma-water mass ratio, interface area, and temperature contrast (Wohletz 1986; Wohletz et al. 2013; Gonnermann 2015; Hajimirza et al. 2022). Fragmentation occurs through thermal granulation during direct melt-water contact or cyclic instabilities in vapour film formation (Sheridan and Wohletz 1983; Kokelaar 1986; Hajimirza et al. 2022). Additional secondary fragmentation can occur within the turbulent explosion in the case of explosive fragmentation (Gonnermann 2015). These processes can be described by four clast-forming mechanisms recognised to occur during hydromagmatic fragmentation (Figure 2.5): water vapour formation, which causes (1) contact-surface interaction and (2) bulk interaction, (3) cooling-contraction granulation, and (4) dynamic stressing (Kokelaar 1986). These processes commonly occur simultaneously and can mutually enhance one another.

(1) Contact-surface interaction

The first type of fragmentation driven by steam formation is contact-surface interaction (Figure 2.5a), which occurs at the interface between the magma and water. The degree of explosivity is a result of the heat flux between the two, as well as the confining pressure that governs the boiling point and expansion ratio of water from the liquid to vapour phase. Fragmentation occurs non-explosively with the formation of an insulating vapour layer as steam bubbles coalesce at the interface (Kokelaar 1986; White 1996). In the event of explosive contact-surface interaction, the vapour layer is unstable, and undergoes a rapid, cyclic process of expansion and collapse. Through this, direct contact accompanied by rapid heat transfer occurs between the magma and water. These rapid oscillations in the vapour layer finely fragment and turbulently mix the magma with the water (Kokelaar 1986). Fine fragmentation greatly increases the heat-transferring surface of the melt, resulting in a positive feedback causing more fragmentation (Zimanowski et al. 1991).

(2) Bulk interaction

This is an explosive result of water vapour formation that occurs when liquid water is enclosed or trapped close to magma. The clast forming processes of bulk interaction are the tearing apart of magma surrounding the explosively expanding water vapour (Figure 2.5b) (Kokelaar 1986), as well as the shattering of chilled margins by the associated pressure waves (Brooks 1995). As with magmatic explosivity, the explosive expansion of the liquid to vapour water phase change depends on the confining pressure, with the overall volumetric expansion being subdued at greater depths and pressures.

(3) Cooling-contraction granulation

Cooling-contraction granulation (Figure 2.5c), also referred to as thermal granulation or quench fragmentation, is a non-explosive fragmentation mechanism that occurs when magma cools too rapidly for its reduction in volume to be accommodated by ductile deformation. During cooling, contraction of the outer layer of a magma body may be accommodated by viscous flow. Once the outer layer becomes rigid and the interior of the magma cools, the thermal stresses induced by this cooling overcome the tensile strength of the melt (Kokelaar 1986; Colombier et al. 2019).

Water is a far more efficient cooling medium than air, enabling magma to cool rapidly upon contact. This rapid heat loss in contact with water, known as quenching, can cause the surface of the magma to cool almost instantaneously to the ambient water temperature, often producing glassy margins (Lamur et al. 2018; Colombier et al. 2019). The presence of jigsaw-fit textures in subaqueous settings is generally attributed to in situ thermal granulation (Colombier et al. 2019). In this process, unlike explosive fragmentation mechanisms, granulation occurs without particle dispersal; the clasts remain at or near their site of formation.

The effectiveness of cooling-contraction is strongly influenced by the physical properties of the magma. The process is not limited by pressure, so can occur at any depth, but at shallow levels may be replaced by explosive contact-surface interaction (Kokelaar 1986). A key control on the onset of granulation is the tensile strength of the magma, which determines the maximum stress the magma can endure through elastic deformation before fracturing. Therefore, factors influencing the tensile strength of the magma affect the granulation; vesicularity, vesicle size, and the permeability and crystallinity of the magma influence the tensile strength (Heap et al. 2014; Colombier et al. 2019). When fragmentation does occur, it can proceed extremely rapidly, with crack propagation expected to be in the range of hundreds to thousands of metres per second (Otterloo et al. 2015).

(4) Dynamic stressing

Dynamic stressing (Figure 2.5d) is a brittle, in situ granulation process that also results from cooling of a magma body margin. The terms mechanical stress and autobrecciation also refer to this mechanism (Skilling et al. 2002). In this case, continued movement of fluid magma within the parent body breaks apart a margin that has rapidly chilled and is no longer ductile (Kokelaar 1986).

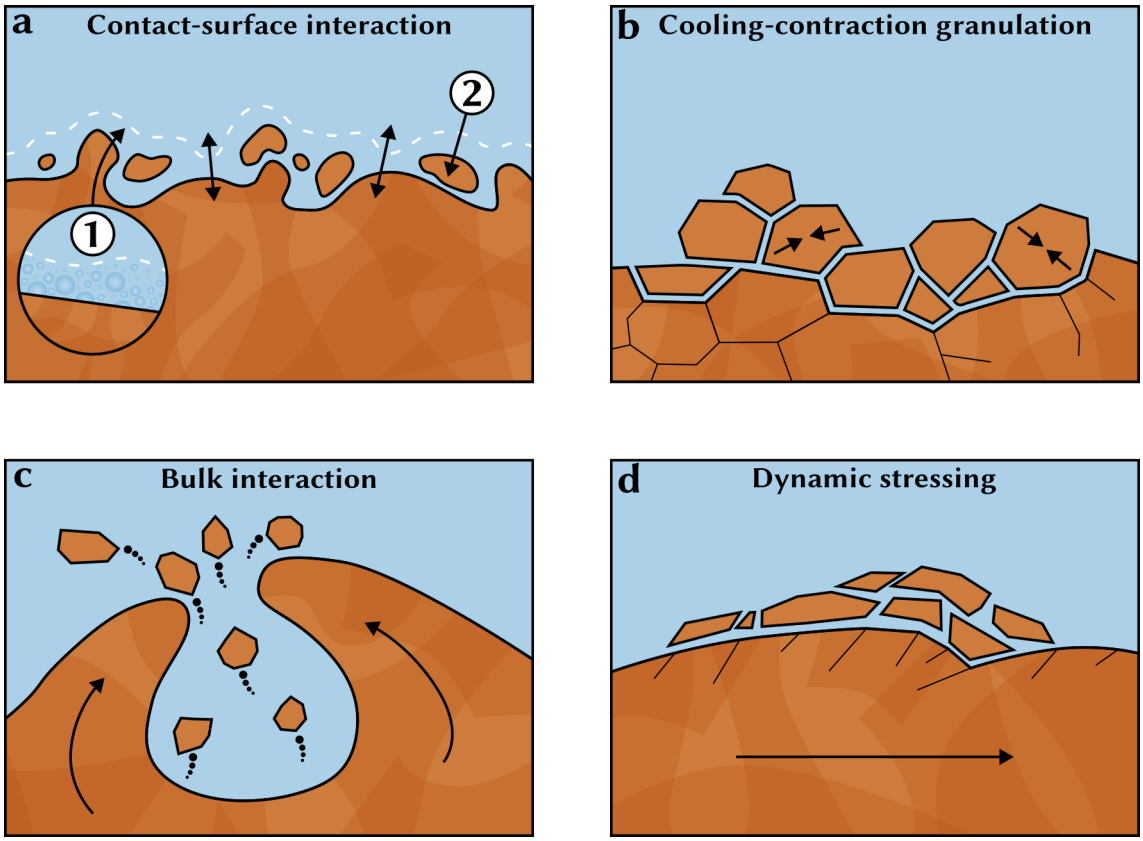

Figure 2.5 Mechanisms of fragmentation that occur during magma-water interactions. **(a)** Contact-surface interaction, with rapid oscillations of a vapour film **(1)** driving fine-scale fragmentation **(2)**. **(b)** Cooling-contraction granulation of quenched magma. **(c)** Bulk interaction of magma surrounding water. **(d)** Dynamic stressing of chilled magma margins. Based on Skilling et al. (2002).

The mixing of magma with wet sediments is likely a ubiquitous process, fundamental to peperite genesis and the conduit dynamics of phreatomagmatism and emergent volcanism (Kokelaar 1983). It is suggested through comparable textures, structures, and shapes formed, that the mechanisms of fragmentation during magma-water interaction and magma-wet sediment interaction are similar (Doyle 2000). However, critical differences exist between pure water and water-saturated sediments, including density, viscosity, bubble nucleation sites, and other fluid properties (White 1996). While increased nucleation sites may enhance potential explosivity, the higher density and viscosity of a wet sediment act to inhibit explosivity, favouring a coarse mixing of the two. This greatly increased degree of pre-detonation mixing provides a setting for potential more voluminous, energetic interactions (White 1996).

2.3 Reading volcanic processes through morphology and texture

Because it is impossible to directly observe magma ascent, vesiculation, and fragmentation, these processes must be inferred indirectly. Records of volcanic processes are often preserved in the morphologies and textures of their erupted or emplaced products. Consequently, the interpretation of these characteristics has become a fundamental practice across the discipline of volcanology.

Morphological features (form, shape, and structure) reflect key parameters in magma dynamics including viscosity, volatile content, degree of interaction with external water, and subsequent

transport and sedimentation processes (e.g., Wohletz 1983; Dellino and La Volpe 1996; Zimanowski et al. 1997). Accordingly, shape measurements provide a means of constraining the origin, evolution, and behaviour of volcanic products (e.g., Dellino and La Volpe 1996; Büttner et al. 1999; Shea et al. 2010). Morphological interpretations have been applied to a broad range of volcanic features, including extrusive lava flows (e.g., Hulme 1974), intrusive bodies such as sills (e.g., Schofield et al. 2012), and most extensively, pyroclastic deposits (e.g., Dellino and La Volpe 1996; Büttner et al. 1999; Alfano et al. 2011). Textural features also preserve information on magmatic and eruptive conditions. Vesicles, for example, represent frozen records of degassing processes in magmas (Shea et al. 2010).

Together, the study of morphology and texture offers a means to reconstruct the complex mechanisms that govern magma fragmentation, transport, and emplacement of pyroclastic deposits. This framework can be extended to peperite, where the morphologies and textures of juvenile clasts record the fragmentation and mingling processes that accompany magma-wet sediment interaction. These features are explored in detail in the following sections of this review.

2.3.1 Quantifying volcanic morphology and texture

Morphological and textural characterisation can be approached through either qualitative descriptions or quantitative numerical methods. Qualitative descriptions provide a straightforward means of recognising geological features in the field, but they are inherently subjective and difficult to compare across studies. Quantitative approaches offer several advantages: they remove subjectivity by allowing objective, reproducible characterisation based on measurable metrics (Dellino and La Volpe 1996). Such metrics can be statistically analysed and compared between datasets, offering a robust methodology for linking form to process. Despite these advantages, peperite studies have relied on qualitative descriptions of clasts and sediment, while quantitative methods commonly applied to other volcanic particles remain unused. This disparity may stem from the inherent difficulty in quantifying lithified particles, in which particle visibility and isolation is often hindered.

Particle morphology is analysed across many physical sciences to link form and process. In volcanology, quantitative characterisation of particles began with 2D shape analysis of pyroclastic deposits (Dellino and La Volpe 1996) and is now widely used; virtually all studies of pyroclastic deposits include quantitative descriptions of particle shape (Dürig et al. 2018). Such analyses are reproducible, avoid subjectivity, and allow direct comparisons between particles and particle populations to be made (Liu et al. 2015).

The shape parameters (SPs) circularity, elongation, and rectangularity used by Dellino and La Volpe (1996) have since been refined to identify those that best capture variations in particle shape (Liu et al. 2015). Unlike basic geometric measurements such as area or perimeter, SPs are non-dimensional ratios derived from these measurements. While simple, regular shape geometry can often be captured by a single measurement (such as a circle by its diameter), complex, irregular shapes like pyroclasts require multiple. Combining these into SPs enables quantitative comparisons of complex shapes, and as a ratio, are independent of particle size (Liu et al. 2015).

Selecting an appropriate set of SPs for quantifying particle shape is important to ensure shape is fully and unbiasedly described. More than one parameter is required to allow reliable comparisons between particles, since most SPs are relevant to one category of morphology only (Nurfiani and Bouvet de Maisonneuve 2018). Therefore, too few SPs, and the shape may be insufficiently described, while too many can result in computational inefficiency. Many SPs are sensitive to the same underlying aspects of shape complexity or irregularity; therefore, SPs

should be chosen to avoid unnecessary redundancy and prevent biases towards specific shape properties.

Liu et al. (2015) identify three morphometric categories to which SPs are sensitive and tend to cluster: form, morphological roughness, and textural roughness. *Form* describes gross shape, *morphological roughness* captures particle-scale irregularities in shape outline, and *textural roughness* the small-scale complexities (relative to particle dimensions) in shape outline. Three SPs - solidity (SLD), convexity (CVX), and axial ratio (AxlR) - effectively account for the variance within these categories. SLD measures the difference in area between a particle and its convex hull (morphological roughness), while CVX quantifies the excess perimeter of a particle relative to its convex hull (textural roughness). Normalised to the convex hull, they are independent of form. AxlR is a measure of form, comparing the major and minor axis of a particle's best fit ellipse. These SPs are equivalently scaled between 0 and 1, where a perfect circle equals 1, and are independent of particle orientation. Including more than one SP per morphometric category offers little additional insight and may introduce bias. Form factor (FF) is also recommended, as it is sensitive to both elongation (form) and roughness, so is well suited for assessing overall irregularity (Liu et al. 2015).

In addition to particle morphology, the internal textures of particles - such as vesicularity and mineral content - provide insights into the physical processing governing volcanic activity. In particular, vesicle textures record the chronology and extent of magma degassing and ascent dynamics (Shea et al. 2010). Quantitative analysis of these textures, through measurements of vesicle size distributions, spatial arrangements, and shapes, therefore complements morphological studies by offering further understanding of the processes that shape volcanic materials.

2.4 Peperite morphologies

Peperites can be identified, described, and interpreted by examining the textural and structural characteristics of the juvenile clasts, as well as the spatial relationships between the clasts, intrusion, and host sediment. These characteristics make it possible to reconstruct the peperite-forming processes of a locality largely from field observations alone (Brooks 1995).

2.4.1 Peperite architecture

The architecture of peperite domains encompasses their overall geometry, internal organisation, and the relationships with the surrounding host sediment. Domains exhibit significant variability in overall extent, ranging from volumes of less than a few m^3 to several km^3 (Skilling et al. 2002). For example, Hanson and Wilson (1993) describe a peperite domain with an exposed areal extent of 3 km^2, representing a total volume of several cubic kilometres. The Honister peperites are suspected to be on a similar cubic kilometre scale.

Peperite domains can be categorised into either closely packed or dispersed types based on the degree of separation between juvenile clasts (Hanson and Wilson 1993). Closely packed peperite occurs broadly parallel to the intrusion contact. At its most extreme, there is little or no displacement between the tightly interlocking clasts, indicating complete in situ brecciation of the intrusion margin. Overall texture is termed *jigsaw-fit*, where clast margins neatly align, and host sediment fills joints and fractures to define clast boundaries. Doyle (2000) describes similar morphologies of a blocky coherent intrusion merging into domains of closely packed peperite where sedimentary material occupies fractures between jointed blocks. Closely packed

peperite transitions to dispersed peperite as the amount of host sediment between the clasts increases. This transition is typically accompanied with increasing distance from the intrusion and a more chaotic clast fit, with Martin and Nemeth (2007) describing a sharp decrease in clast/host sediment ratio within a few metres from the intrusion contact. Peperites can also be classed into either coarse grained or fine grained in reference to the size of clasts, with a transition from larger to smaller clasts nearer the contact with the parent intrusion (Brooks 1995).

The contact between the intrusion and host sediment frequently displays complex, bulbous geometries. Kokelaar (1982) and Kano (1989) describe these as lobate or finger-like protrusions extending from the primary intrusion with no preferred orientation. They vary in shape from globular to highly elongate, and their interiors are predominantly massive - that is, they lack internal structures. Protrusions are surrounded by, and grade into, closely packed and dispersed peperite (Hanson and Wilson 1993). While lobes and pods often appear as isolated coherent bodies within the peperite domain, they are commonly interpreted as cross-sections of fingers connected to the primary intrusion in three-dimensional space (e.g., Hanson and Wilson 1993; Doyle 2000). The formation of these protrusions challenges elastic models of magma intruding into a solid, lithified sediment, in which tabular shaped intrusions are more likely to form in response to brittle fracture of the country rock. Instead, these morphologies describe a mechanism where magma intrusion is accommodated by viscous deformation of the host (Schofield et al. 2012; Galland et al. 2019). Kano (1989) describes these interactions as contact between two viscous liquids and reports sedimentary beds that have been dragged in a ductile state by the intrusive material.

Adjacent to peperite domains, sedimentary structures of the host sequence are generally well preserved. This is in stark contrast to the sedimentary matrix within the peperite, where there is complete destruction of sedimentary structures (e.g., Hanson and Wilson 1993; Hanson and Hargrove 1999; Martin and Nemeth 2007). Within dispersed peperite, there is nearly complete homogenisation of large volumes of sediment. This is a result of complex, thorough intermixing between the igneous material and disrupted sediment, and indicates a highly mobile sediment during peperite genesis (Hanson and Wilson 1993). On a smaller scale, lamination of fine-grained host sediments is often truncated at the margins of intrusive bodies. This is the result of sediment being homogenised in a narrow band around the intrusion margin. Martin and Nemeth (2007) describe this homogenisation as a 'halo'. Halos of homogenised sediment are described as narrow in areas where fluidal peperite has formed, and up to a metre wide in areas of blocky peperite (Martin and Nemeth 2007).

Undeformed host bedding presents an apparent space problem. Branney and Suthren (1988) and Brooks (1995) describe discordance between intrusive material and the bedding of the host sediment, which has been well preserved. These features suggest that magma has physically displaced the host sediment, with an active process of sediment removal from the site of intrusion. Such processes can be explained by fluidisation of a wet and unconsolidated host sediment (Kokelaar 1982). Fluidisation is a mechanism explored later in this review (Subsection 2.6.1).

2.4.2 Characteristics of juvenile clasts

The igneous components of a peperite breccia, the juvenile clasts, are monomict. All clasts are derived from, and are compositionally identical to, the parent intrusion. However, textures and morphologies of individual clasts can vary significantly. Clasts can range in size from metres to millimetres, and shape, vesicularity, and groundmass texture can all vary (Skilling et al. 2002). Specific textures provide evidence for the host sediment being wet and unconsolidated at the time of intrusion. These include: glassy quenched clast rims, fractures consistent with cooling-

contraction granulation, homogenised host sediment surrounding clasts or infilling fractures and vesicles (Goto and McPhie 1996).

Peperites are generally classified by the dominant shape of the juvenile clasts (Figure 2.6). Busby-Spera and White (1987) describe two types with reference to their shape: (1) fluidal clasts, which are globular in shape, and (2) blocky clasts, which are angular in shape. While blocky peperites have been described most frequently, followed by fluidal clasts, significant variation exists outside of these end-member definitions. (3) Platy clasts, for example, are frequently described (Brooks 1995; Goto and McPhie 1996; Doyle 2000). Additional morphologies include tapered, ragged (Skilling et al. 2002), mesoblocky, and strongly vesicular clasts (Doyle 2000). Peperite domains often consist of a mixture of clast types, and individual clasts can display both fluidal and blocky margins (Skilling et al. 2002). Intermixed peperite is termed mixed blocky and fluidal peperite (Hanson and Hargrove 1999).

(1) Fluidal clasts

Fluidal clasts have curvy and bulbous margins (Figure 2.6a). They take on a wide range of shapes, from globules, to elongated, high-aspect-ratio lobes, and highly irregular, complex amoeboids (Skilling et al. 2002). Hanson and Hargrove (1999) describe fluidal clasts connected by thin necks, likely in three dimensions and resembling larger coherent lobes and tongues of igneous material.

(2) Blocky clasts

Blocky clasts have planar to sub-planar margins, generally polygonal in shape when described in 2D (Figure 2.6b). Clast placement can be chaotic, with high dispersion of clasts within a disrupted host sediment. Equally, blocky clasts can be closely packed. A key characteristic of closely-packed blocky clasts is the widespread preservation of in situ (jigsaw-fit) fragmentation textures, which occur across a range of extents, from entire outcrops to individual thin sections (Hanson and Wilson 1993; Hanson and Hargrove 1999; Doyle 2000). Textures of this type consist of clasts separated by sediment with outlines that can be closely matched like pieces of a jigsaw puzzle.

(3) Platy clasts

Morphologically similar to blocky clasts, platy clasts are elongate in shape with planar to curviplanar margins (Figure 2.6c). They are more common in closely packed peperite, typically parallel and adjacent to the parent intrusion (Brooks 1995). Platy clasts generally form jigsaw-fit aggregates separated by minor amounts of the sedimentary host (Doyle 2000). Goto and McPhie (1996) describe platy clasts as curved splinters arranged subparallel and continuous with spherical fractures at the intrusion margins.

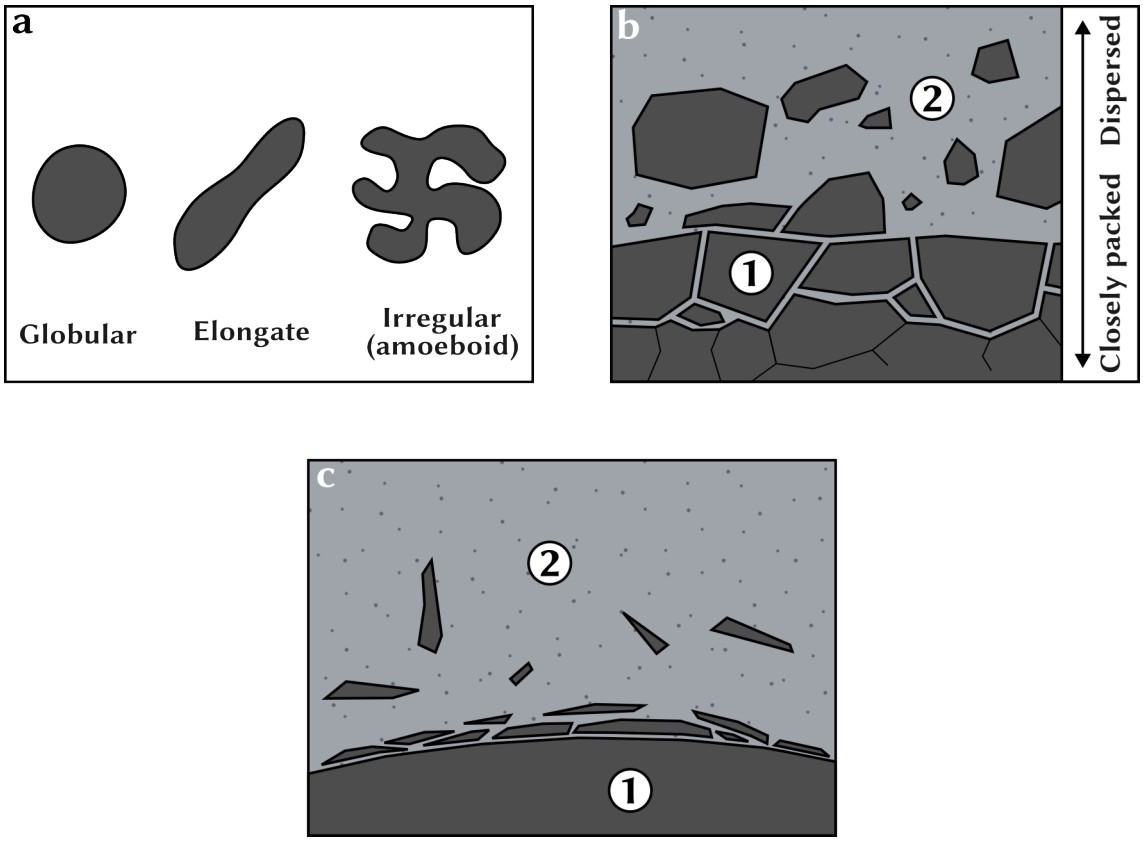

Figure 2.6 Primary textures of juvenile clasts. **(a)** Fluidal clasts and the associated complex morphologies. **(b)** blocky clasts, with closely packed (in situ) placement **(1)** and dispersed placement within the host sediment **(2)**. **(c)** Platy clasts parallel to the intrusion **(1)** and dispersed a short distance **(2)**. Based on Skilling et al. (2002).

2.5 Formation mechanisms of juvenile clasts

Whether a peperite texture is blocky, fluidal, or mixed, and its clasts closely packed or widely dispersed, is determined by the factors influencing the fragmentation process of the clasts, and their subsequent mingling with the host sediment. Fragmentation occurs on a scale from ductile to brittle, with fluidal clasts forming in the ductile regime and blocky clasts in the brittle regime. The factors influencing fragmentation include local stresses, confining pressure, the amount and rate of magma emplacement, magma rheology, pore water content, and type of host sediment (Kano 1989). The presence of mixed peperite within the same host sediment indicates a change in the fragmentation mechanism (Martin and Nemeth 2007); fluidal behaviour during initial contact may be followed by brittle behaviour in the later stages of intrusion, although post-fragmentation shape change may also be relevant to mixed peperite. Changes such as the cooling of magma throughout its intrusion, or a reduction in pore water content and increased sediment lithification can explain the transition from the ductile to brittle regime (Kano 1989; Hanson and Hargrove 1999).

2.5.1 Formation of fluidal peperite

Fluidal juvenile clasts form in the ductile regime (Figure 2.7a), allowing the development of complex fluidal geometries without undergoing brittle fragmentation from quenching. For

magma to remain ductile, direct contact between the magma and host sediment pore water must be prevented through the formation of a stable insulating vapour film (Skilling et al. 2002). This process has been interpreted to represent styles of coarse mixing during MFCI that do not result in explosive interaction (Kokelaar 1986; Busby-Spera and White 1987; White 1996). The vapour film oscillates in thickness (Wohletz 1986). These repeated oscillations of the vapour film may cause small-scale instabilities, with detachment of fluidal droplets of fuel (magma) and intermixing with the adjacent coolant (wet sediment). The clasts are shaped by the effects of surface tension (Busby-Spera and White 1987). Fluidal intrusion of magma may be accompanied by fluidisation of host sediment in the vapour film (Kokelaar 1982), a process discussed further below. This process is also responsible for the formation of fluidal pods and lobes of magma.

2.5.2 Formation of blocky peperite

Blocky juvenile clasts are evidence of magma fragmentation in the brittle regime (Figure 2.7b), producing clasts of several morphologies, including blocky and platy (Skilling et al. 2002). Additionally, blocky clasts are indicative of limited post-fragmentation deformation. Brittle fragmentation is favoured when magma viscosity and/or strain rates are high. Along with jigsaw-fit textures suggesting in situ fragmentation mechanisms, this implies fragmentation by cooling-contraction granulation (quench fragmentation) and dynamic stressing are most important during blocky peperite formation (Kokelaar 1986; Hanson and Wilson 1993; Skilling et al. 2002). Chilled margins may be present on blocky clasts (e.g., Goto and McPhie 1996). These provide direct evidence that the clasts were molten on fragmentation and that their surfaces were quenched rapidly, though may be difficult to observe in older peperites. While these processes account for closely packed peperite domains, where clasts are developed in situ or transported only short distances, they cannot account for the longer-range transport of blocky clasts present in dispersed peperite domains.

The disruption and dispersal of blocky juvenile clasts is likely a result of hydromagmatic explosions (e.g., Busby-Spera and White 1987; Branney and Suthren 1988; Hanson and Hargrove 1999), coinciding with the fragmentation mechanisms explosive contact-surface interaction and bulk interaction. Explosions are more likely to occur during the initial intrusion of magma when heat transfer and volatile release rates are highest; however, later explosions can also occur, causing secondary fragmentation of pre-existing peperite (Skilling et al. 2002). Confining pressure is an important limiter of explosive contact-surface interaction; higher pressures limit water's expansion ratio at the liquid-gas phase transition, therefore influencing explosivity and clast dispersion (Kokelaar 1986). Localities of blocky peperite scattered within the primary intrusive body likely represent pods of wet sediment being enveloped during bulk interaction (Branney and Suthren 1988; Brooks 1995). As hydromagmatic explosions require rapid heat transfer, the development of a stable insulating vapour film is unlikely to have occurred (Skilling et al. 2002) (Skilling, White and McPhie, 2002).

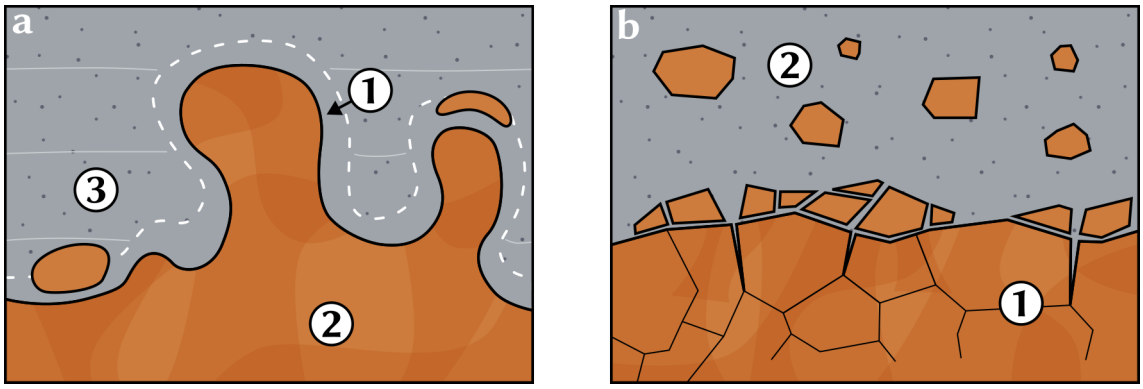

Figure 2.7 Processes involved in the formation of fluidal and blocky peperite textures. **(a)** Formation of fluidal peperite. Development of a thin, stable vapour film **(1)** at the contact between the magma **(2)** and wet sediment **(3)**. Note host sedimentary structures remains relatively undisturbed and are truncated at contact margins. **(b)** Formation of blocky peperite. Development of an insulating vapour film does not occur. Relatively rapid heat transfer promotes cooling-contraction and dynamic stressing of the intrusion **(1)**. Dispersal of clasts through explosive hydromagmatic processes (explosive cooling-contraction, bulk interaction) causes disruption and homogenisation of the host sediment **(2)**. Based on Hanson and Hargrove (1999).

2.5.3 Controls on peperite texture

Several controls on peperite texture have been described at peperite localities worldwide. Busby-Spera and White (1987) concluded that variations in peperite texture within the Alisitos Group, Mexico, were a result of the contrasting physical properties of the host sediments the magma intruded into. Fluidal peperite formed in well sorted, fine-grained, and low permeability sediment where a sustained vapour film at the magma-wet sediment interface facilitated ductile fragmentation. In contrast, blocky peperite formed in poorly sorted, coarse-grained, and relatively more permeable sediment, which disrupted the development of a vapour film and caused brittle fragmentation.

Comparable relations between host sediment and peperite texture are present in the Tuttle Lake Formation of northern California (Hanson and Hargrove 1999). Busby-Spera and White (1987) concluded that higher permeability was the primary factor of the coarser host sediment responsible for blocky peperite formation. A higher permeability facilitates a faster escape of heated pore water, in turn preventing a stable vapour film. In contrast, the sediments of the Tuttle Lake Formation (Hanson and Hargrove 1999) have similarly low permeability. Hence, grain size is suggested as the main control of blocky vs fluidal peperite at this locality, with coarser particles physically disrupting the formation of a vapour film. Additionally, Hanson and Hargrove (1999) suggest coarser-grained clasts may impede the advance of the intrusion. This leads to a thicker chilled margin, promoting brittle fragmentation, and the formation of blocky clasts.

Busby-Spera and White (1987) demonstrated that, assuming intrusion properties remain constant, interaction with different host sediments should produce a predictable range of peperite textures. However, the presence of both fluidal and blocky clasts within the same peperite domain, as well as many individual clasts displaying both fluidal and blocky margins (Skilling et al. 2002), indicates factors beyond host sediment properties must also influence the peperite textures formed. Such textural mixtures imply that different fragmentation processes must be occurring, either simultaneously or sequentially. Magma viscosity is presented as a key control: fluidal peperites are typically associated with relatively low-viscosity magma, while blocky peperites are favoured when magma viscosity increases due to cooling, crystallisation, or variations in

magmatic composition (Chen et al. 2013). In this case, magma viscosity during fragmentation is controlled by the presence of a vapour film, which in turn is controlled by the type of host sediment.

Peperite textures formed in the Stanley beds of northwestern Tasmania, Australia, were controlled by factors other than the physical properties of the host sediment (Goto and McPhie 1996). Here, a two-stage intrusion with varying viscosities is proposed to explain the coexistence of fluidal apophyses and blocky clasts in the same poorly sorted, coarse-grained sediments. An earlier, hotter, lower viscosity stage likely produced fluidal clasts through ductile fragmentation, while a later, cooler, and higher viscosity stage formed blocky clasts under a more brittle fragmentation regime. Chen et al. (2013) similarly attributes differences in peperite texture in the Tailegula Formation, China, to changes in magma viscosity over the course of intrusion. Fluidal clasts truncated by planar surfaces, often broken in a jigsaw-fit fashion, indicate that individual clasts have undergone two distinct fragmentation regimes sequentially. This viscosity change is suggested to result from magma cooling and/or the breakdown of vapour films. Additionally, confining pressure is described as an influence on magma viscosity, with Chen et al. (2013) describing fluidal peperites in the middle and lower sections of the succession, and blocky textures in the upper sections. This transition from fluidal to blocky textures could reflect increasing magma viscosity due to lower confining pressure at shallower depths.

2.6 Clast-sediment mingling dynamics

Mingling of the juvenile clasts and host sediment is promoted by a number of mechanisms: transient mobilisation of the host sediment through fluidisation, hydromagmatic explosions, liquefaction, and other processes including the forceful intrusion of magma and magma-sediment density contrasts (Figure 2.8) (Skilling et al. 2002).

2.6.1 Fluidisation of the host sediment

Fluidisation was established as a geological term by Reynolds (1954), and describes a process in which solid particles behave like fluid when suspended in a gas or liquid with a critical flow velocity. At or above this flow velocity, the hydrodynamic drag force on the particles balances or exceeds their weight.

Fluidisation is a key process in peperite formation, as it is a mechanism by which large volumes of sediment can be discordantly replaced by igneous material with minimum disturbance to the remaining host (Kokelaar 1982). As magma propagates into wet sediments, the host material may become entrained into and fluidised by pore water vapour. This vapour is generated either through heating of pore water at the magma/wet-sediment interface or by rapid pressure release during fracture opening (Kokelaar 1982). Water-rich sediments fluidised by expanding pore water vapour offer little resistance, providing a rapid pathway for the intruding magma (Brooks 1995).

Two types of fluidisation have been described in the context of wet sediment fluidisation: (1) continuous, large volume and (2) momentary, small volume. Fluidisation is dependent on the attainment of a minimum vapour flow velocity. This threshold is itself dependent on factors such as vapour density, sediment particle size, and particle distribution (Kokelaar 1982).

(1) Continuous fluidisation

Continuous fluidisation occurs where a sustained heat source prevents condensation, providing persistent vapour generation. This is evident along magma/wet sediment contacts, where large volumes of sediment can be transported considerable distances. Here, vapour generation can persist when a stable vapour layer is formed (Kokelaar 1986). Vapour will flow due to its buoyancy, transporting entrained sediment from areas of high to low pressure, typically parallel to the interface (Kokelaar 1982). Water vapour movement parallel to the intrusion is preferentially preserved as movement away from the intrusion results in cooling and condensation (Busby-Spera and White 1987). Because this process is confined to the magma/wet-sediment contact, the surrounding host sediment remains largely undisturbed. Hence, evidence for fluidisation is seen where intrusions have propagated into wet sediments with minimal disruption to the remaining host (e.g., Kokelaar 1982; Branney and Suthren 1988; Brooks 1995; Martin and Nemeth 2007). This includes the termination of the bedding or laminae in the host sediment against the bands of homogenised sediment around the intrusion (Hanson and Hargrove 1999).

(2) Momentary fluidisation

Momentary fluidisation results in local sediment reconstitution and transport (Kokelaar 1982). This type of fluidisation is evident where the host sediment has been injected into fractures in the intrusive body. Brooks (1995) describes shrinkage fractures, formed through quenching of the intrusion margin, which have been filled with homogenised sediment. Hanson and Wilson (1993) describe these fractures as 'dyke like injections' and record widths of up to several centimetres wide and considerable lengths. The fractures contain small, blocky and platy peperite clasts broken from the adjacent intrusion in situ (Hanson and Wilson 1993; Brooks 1995). The use of the term *dyke* is perhaps misleading, implying the sediment is actively intruding the magma, as opposed to passive infilling. It is thought that shrinkage fractures open abruptly, resulting in an instantaneous drop in pressure and explosive expansion of pore water vapour and fluidised entrained sediment into the cavity. This mechanism was first clearly described by Walton and O'Sullivan (1950). Brooks (1995) describes synclines within laminated host sediment that are aligned with these fractures. They are interpreted to have formed by ductile deformation of the non-fluidised host sediment being pulled into the upper sections of the fractures.

In addition to fluidisation into fractures of the intrusion, fluidisation can be propagated along irregular pipes into the host sediment. This occurs where host sediments become sufficiently hot, potentially at localised points along the interface (Kokelaar 1982). Vapour generated at these points 'drills' outward into the host sediment producing elutriation pipes; finer material is removed, leaving behind a pipe filled with a concentration of larger clasts and contact-derived material (Kokelaar 1982; Busby-Spera and White 1987). Such structures range in size from sub-mm to dm in width (Skilling et al. 2002).

Further evidence for fluidisation is recorded by orientated crystals, glass shards, and quartz grains within the fluidised margins (Martin and Nemeth 2007), and sediment filling vesicles and hairline cracks in volcanic clasts (Kokelaar 1982).

2.6.2 Other mingling mechanisms

As discussed in the section on blocky peperite formation, hydromagmatic explosions are inferred to account for domains of widely dispersed clasts. These explosions can be responsible for

the initial mingling of clasts and sediment, as well as secondary dispersion and mingling of pre-existing peperite (Skilling et al. 2002).

Whereas fluidisation describes sediment particles being suspended by a moving fluid (pore-water vapour in this case), liquefaction is a process by which a liquid-saturated material exhibits fluidal behaviour by application of stress, without the addition of more fluid volume (Zimanowski and Büttner 2002). Fluidisation requires a critical flow velocity, and is hard to achieve in poorly sorted or cohesive sediments (Skilling et al. 2002). When conditions for fluidisation are not met, liquefaction of water-saturated host sediments can result in the hydrodynamic mingling of the magma and liquified sediments in some peperites (Zimanowski and Büttner 2002).

Mingling may also be driven by the forceful intrusion of magma into the host sediment, and magma-sediment density contrasts, although the relative importance of these mechanisms is lesser known (Skilling et al. 2002). Buoyancy mechanisms have been described for the mingling process of low density fluidal peperites with their host sediments (Donaire et al. 2002).

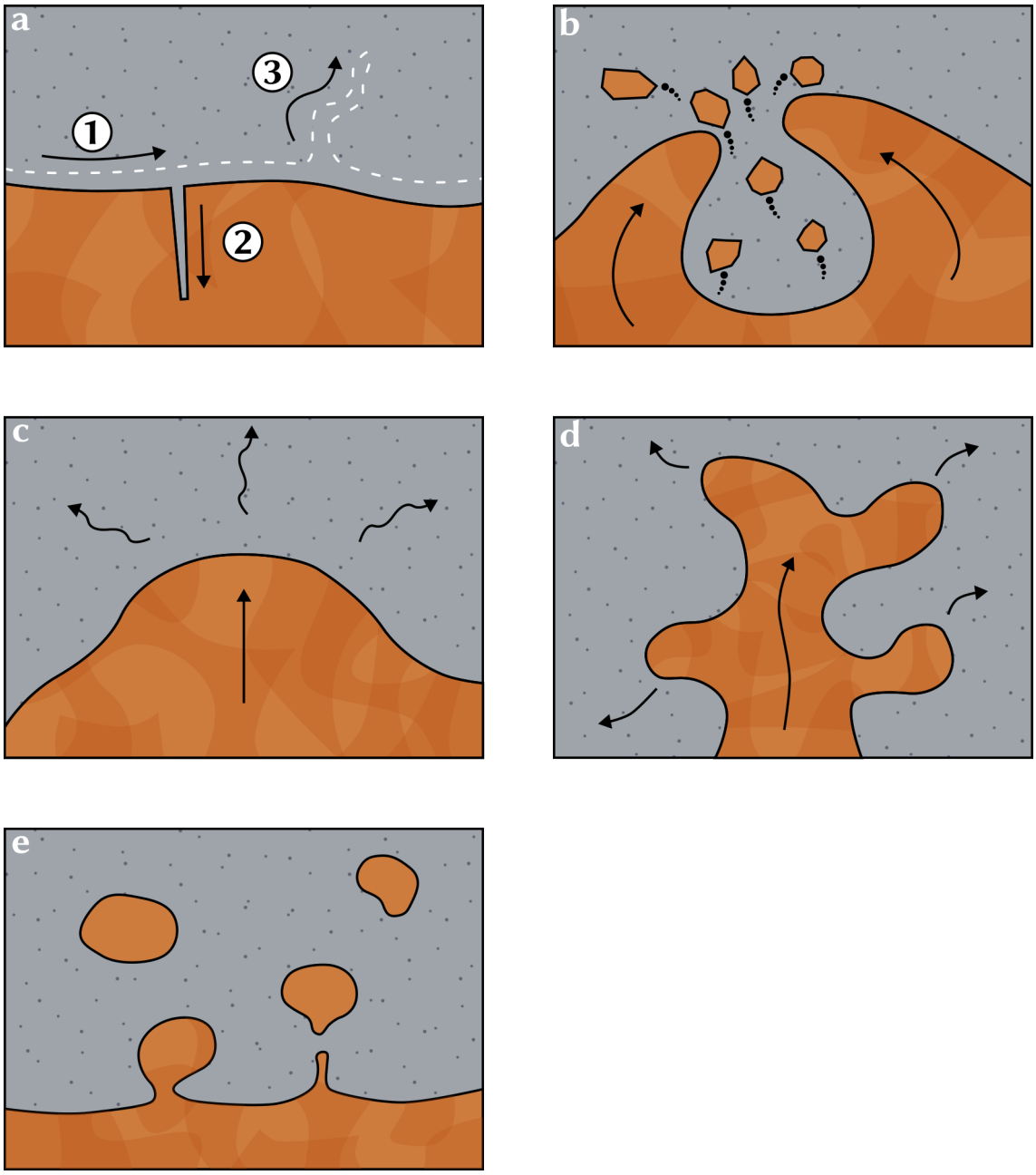

Figure 2.8 Mechanisms of juvenile clast and host sediment mingling. **(a)** Fluidisation and transport of the host parallel to the contact **(1)**, into fractures in the intrusion **(2)**, and 'drilling' of elutriation pipes outward into the host **(3)**. **(b)** Hydromagmatic explosions (e.g. bulk interaction). **(c)** Saturated sediment liquefaction in response to stress from the intruding magma. **(d)** Forceful intrusion of magma into the host. **(e)** Magma-wet sediment density contrasts. Based on Skilling et al. (2002).

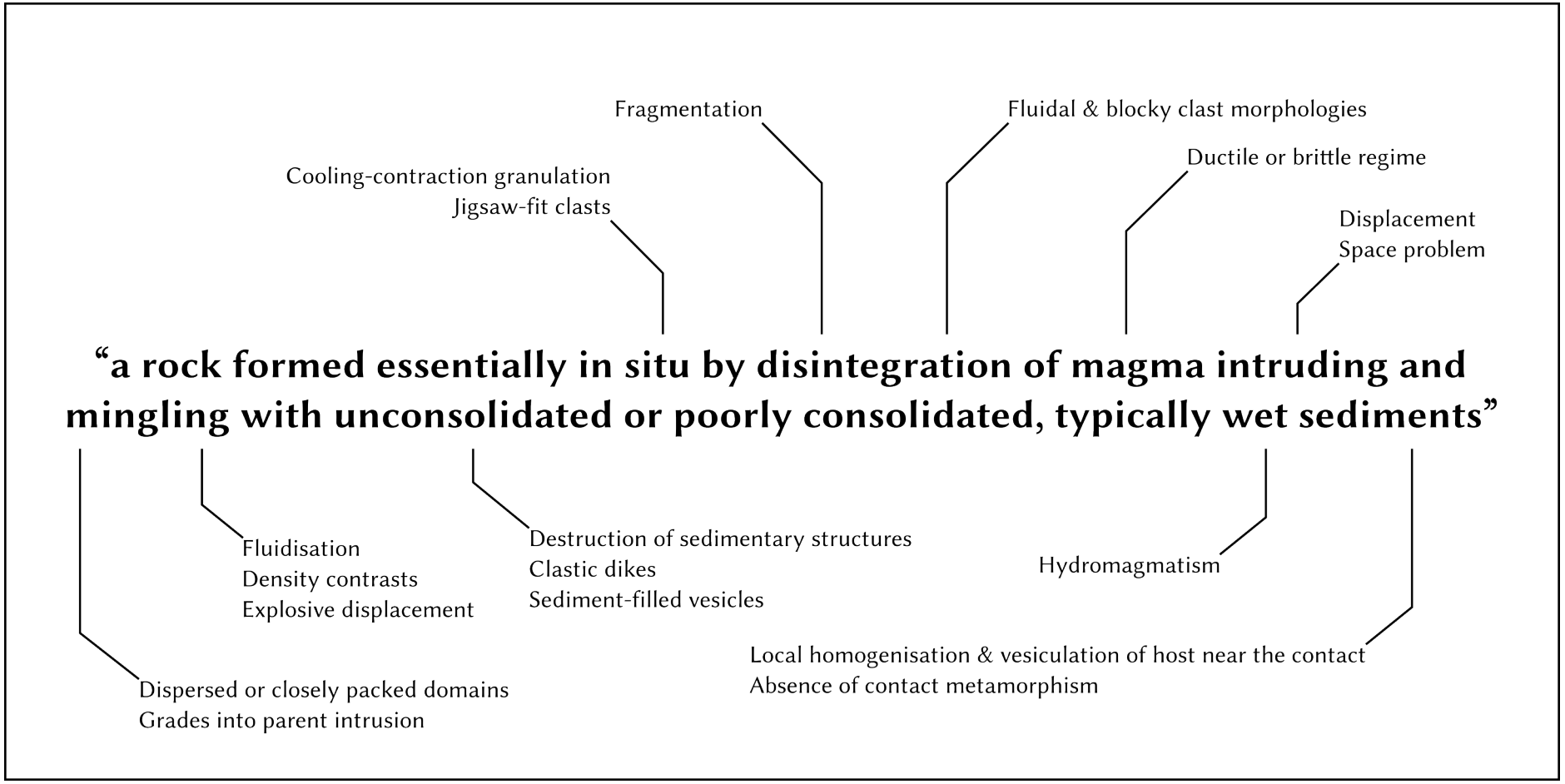

Figure 2.9 A summary of the key characteristics and formation processes of peperite, as discussed in the above sections, in relation to the definition of peperite described by White, McPhie and Skilling (2000).

2.7 Geological setting

The Ordovician Borrowdale Volcanic Group (BVG) of the central English Lake District represents one of the most intense episodes of volcanism in the geological history of the British Isles. The study area, Honister, is located in the north-west of this group (Figure 2.10). The BVG is a thick and rapidly emplaced succession of early Caradoc age (~455 Ma). It comprises more than 6 km of medium- to high-K calc-alkaline basaltic to rhyolitic lavas, sills, and pyroclastic rocks (Petterson et al. 1992; Beddoe-Stephens et al. 1995; Millward 2004b). These igneous rocks were emplaced within a continental arc on the eastern margin of Avalonia, with magmatism attributed to the subduction and closure of the Iapetus Ocean along the Solway Line (Figure 2.10 locator map) (Fitton et al. 1982). The ensuing collision with Laurentia-Baltica led to the Acadian Orogeny (Millward 2004a).

Stratigraphically, the BVG separates two thick marine, mainly turbiditic sedimentary successions (Beddoe-Stephens et al. 1995); it is underlain unconformably by the Skiddaw Group, and overlain, again unconformably, by the Windermere Supergroup. In contrast, the BVG was predominantly subaerially erupted (Branney 1988), though there is abundant evidence of volcaniclastic sediments that have been extensively reworked and deposited by non-marine water. While the neighbouring groups accumulated over about 40 Ma, palaeomagnetic evidence (Piper et al. 1997) and U-Pb zircon radiometric dating (Millward and Evans 2003) indicate that the BVG volcanism spanned less than 5 Ma.

The BVG is subdivided into a lower 2.2-2.7 km thick pre-caldera succession and an upper ~3 km thick caldera-related succession (Branney and Soper 1988; Petterson et al. 1992). The lower BVG can be described as a single stratigraphical unit, the Birker Fell Andesite Formation (BFA). This formation represents the remnants of a predominantly effusive low-topography volcanic field consisting of basaltic to andesitic lavas, sills, and intercalations of volcaniclastic sediments (Petterson et al. 1992; McConnell and Kneller 1993; Millward 2004b). Within the BFA, the Eagle Crag Sandstone Member (EAGC) encompasses the Honister study area; the EAGC is an extensive and thick sequence of reworked volcaniclastic sediments and hosts numerous peperitic sills (McConnell and Kneller 1993).

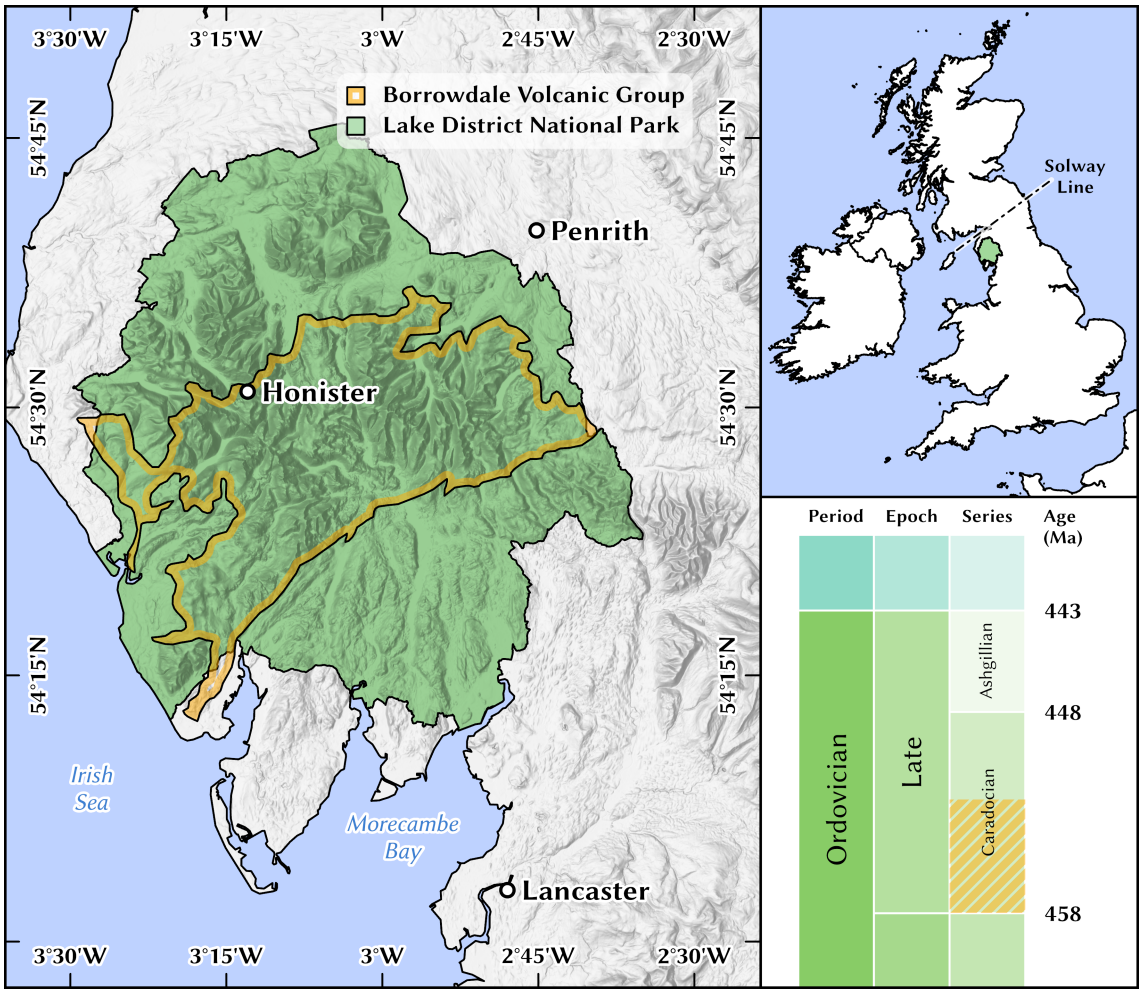

Figure 2.10 Location of Honister within the Borrowdale Volcanic Group (BVG) of the central English Lake District. Locator map shows the relation to the Solway Line. The chronostratigraphic chart highlights the short time frame of volcanism (yellow hatch) that formed the BVG during the late Ordovician.

2.7.1 Peperitic sills of the Borrowdale Volcanic Group

High-level sills are abundant in the BVG and often display peperitic margins. Branney and Suthren (1988) describe eight sills of andesitic composition within the BVG, which share characteristics present in many other peperite formations; the sills are concordant or subconcordant with the host bedding, there is a gradational increase in brecciation and mixing with distance from the sills (e.g., Martin and Nemeth 2007), and brecciation extends locally throughout some sheets (e.g., Hanson and Wilson 1993; Doyle 2000). The andesitic sheets were identified as sills, as opposed to lavas, as they contain matrix supported clasts and vesiculated hosts at the upper margins (Branney and Suthren 1988). These features could only develop at the base of a lava flowing across a wet sediment.

The degree of brecciation in these sills resembles that of block lavas, characterised by angular clasts indicative of brittle fragmentation (autobrecciation or cooling-contraction granulation) (Branney and Suthren 1988). However, fragmentation appears complex, with numerous additional mechanisms involving interaction with the wet host, particularly contact-surface interaction and bulk interaction. The authors discount magmatic fragmentation as playing a major role due to the low vesicularity of the sills. Instead, dispersed blocky clasts within homogenised sediment provide evidence of turbulent mixing driven by small-scale steam explosivity. Any explosivity

was limited and not self-perpetuating, as brecciation remains largely confined to the sill margins.

2.7.2 Peperite exposures at Honister

Peperites are well exposed in disused slate quarries on Fleetwith Pike (Figure 2.11), overlooking Honister Pass, Cumbria. Here, the EAGC is exposed as an alternating sequence of reworked andesitic volcaniclastic sediments and intrusive andesite sheets with a combined thickness of approximately 420 m (McConnell and Kneller 1993).

The sediments of the EAGC exhibit a wide range of lithologies: coarse-grained breccias, pebbly sandstones, and finely laminated siltstones (McConnell and Kneller 1993). Metamorphism of the finest grained sediments has produced a strongly cleaved slate known as 'Westmorland Slate' that has been quarried from either side of Honister Pass. These deposits originated as subaerially erupted pyroclastic fall-out and pyroclastic density current deposits that underwent extensive reworking and redeposition in a shallow subaqueous environment (Woodhall 2000; Millward 2004b). Hyaloclastites and rip-up clasts describe an environment with rapid sediment supply, in addition to turbidites and laminated siltstones representing turbidity current and suspension fallout sedimentation (Branney 1988; McConnell and Kneller 1993). Crucially, the absence of marine fossils and sedimentary facies indicates a non-marine setting (Branney 1988), with a shallow fluvio-lacustrine basin environment interpreted instead (Suthren 1977; Petterson et al. 1992; Millward 2004b).

This sedimentary sequence has been intruded by andesite sills, with eight such sills identified on Fleetwith Pike (McConnell and Kneller 1993). They are described as having various thicknesses, from 5 to 45 m, with massive to jointed interiors transitioning into brecciated peperitic margins. The sequence dips approximately 30° to the south east, the sills intruding roughly parallel to this dip. This dip does not represent an emplacement angle, but rather post-emplacement tectonic deformation. The inter-layered sediments and sheets are topped by a stack of andesite sheets with sediment present only between blocks at the stack margins. These sheets may be interpreted as either sills that have intruded in direct contact with one another, or as a lava cap to the underlain sequence (McConnell and Kneller 1993). This igneous component of the peperite has also been subject to metamorphism, exhibiting a chlorite-rich mineral assemblage and overprinted composition.

Two of the most accessible peperite-bearing exposures are at Hopper Quarry (NY 213 138) and Dubbs Quarry (NY 212 138). Both sites are accessible by a track leading from the Honister Slate Mine buildings and car park (Figure 2.11). On the north-west face of Hopper Quarry, a sequence of silt-to-sand grade sedimentary rock tops the peperitic upper margin of a sill. The top of the sill immediately below the peperite layer is not exposed here. However, the smaller Dubbs Quarry provides exposure on its north-east face of a thinner peperitic margin at the base of a sill approximately 10 m thick. The two quarry exposures relate to two different sills. These exposures provide key localities for examining peperitic sill margins within the Borrowdale Volcanic Group, with Hopper Quarry forming the primary focus of this study.

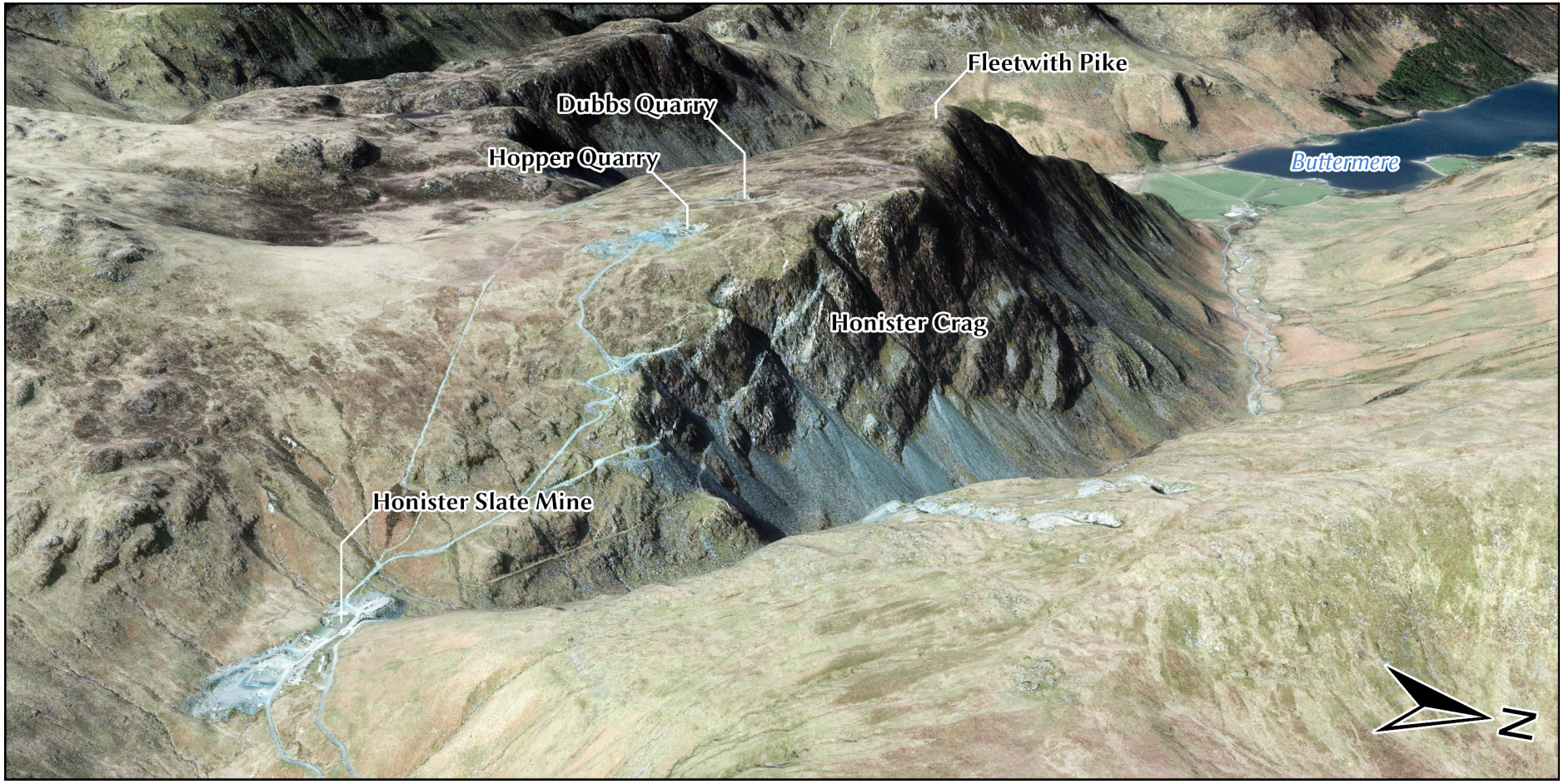

Figure 2.11 Locations of interest at Fleetwith Pike, overlooking Honister Pass, Cumbria. Peperitic margins of andesite sills are exposed on walls in Hopper Quarry and Dubbs Quarry.

Chapter 3

Methodology

This study focused on Hopper Quarry, which provides the most extensive exposure of a peperitic sill margin at Honister. The quality and accessibility of this quarry face provided a favourable setting to address each research objective through field observations, photography, and subsequent image analysis. Quantitative studies of volcanic particles typically involve the collection of unconsolidated field samples for laboratory or field-based analysis. However, peperite exposures are lithified rocks where physical sampling of individual particles is not viable. Consequently, outcrop-scale analysis of particles was required.

To achieve objectives 1-3 (quantification of clast shape, analysis of spatial trends, and association with fragmentation mechanisms), a high-resolution orthomosaic of the peperitic margin was generated from a photographic survey. This allowed individual clasts to be accurately delineated while preserving their relative spatial positions within the quarry face. Shape analysis of these clasts was carried out within the software FIJI, a distribution of ImageJ (Schindelin et al. 2012). Objective 4, characterisation of clast vesicles, was accomplished by outlining vesicles within a subsample of individual clast images, followed by analysis in FIJI. Field observations were performed alongside quantitative morphometry to produce a chronology of peperite formation, with quantitative results used to support these interpretations. The following sections describe the methodologies used to acquire, process, and analyse the imagery used in this study. An overview of the complete workflow is presented in Figure 3.5.

3.1 Imaging and photogrammetry

3.1.1 Quarry-scale photogrammetry

On the north-west face of Hopper Quarry, peperite is primarily exposed in a 22 m wide by 6 m high area, hereafter referred to as Locality A. To enable high-resolution delineation of individual peperite clasts within this exposure, and capture their spatial relationships for subsequent analysis, a systematic photographic survey was conducted to generate an exposure-wide photogrammetric model. Dry, bright, and overcast conditions were chosen for diffuse lighting and minimal shadows. All images were captured using a Canon EOS 1300D DSLR camera. A fixed focal length of 41 mm and aperture set to f/7.1 was used to maintain a consistent depth of field. The shutter speed was adjusted automatically to accommodate varied lighting conditions across the quarry face. ISO was fixed at 400, and exposure compensation set at -0.7. Maintaining consistent lens parameters,

especially focal length and aperture, was important for photogrammetry processing in Agisoft Metashape.

Photographs were captured while walking along a transect parallel to the quarry face at a ~5 m distance, as much as site conditions allowed. At each ~1 m step along the transect, an array of overlapping photographs was taken to capture the area of quarry face visible from that position (Figure 3.1). A high degree of overlap was required for the images to be matched successfully during photogrammetric processing. Reference objects for scaling the model - metre sticks and a 30 m length tape measure - were positioned across the length of the exposure.

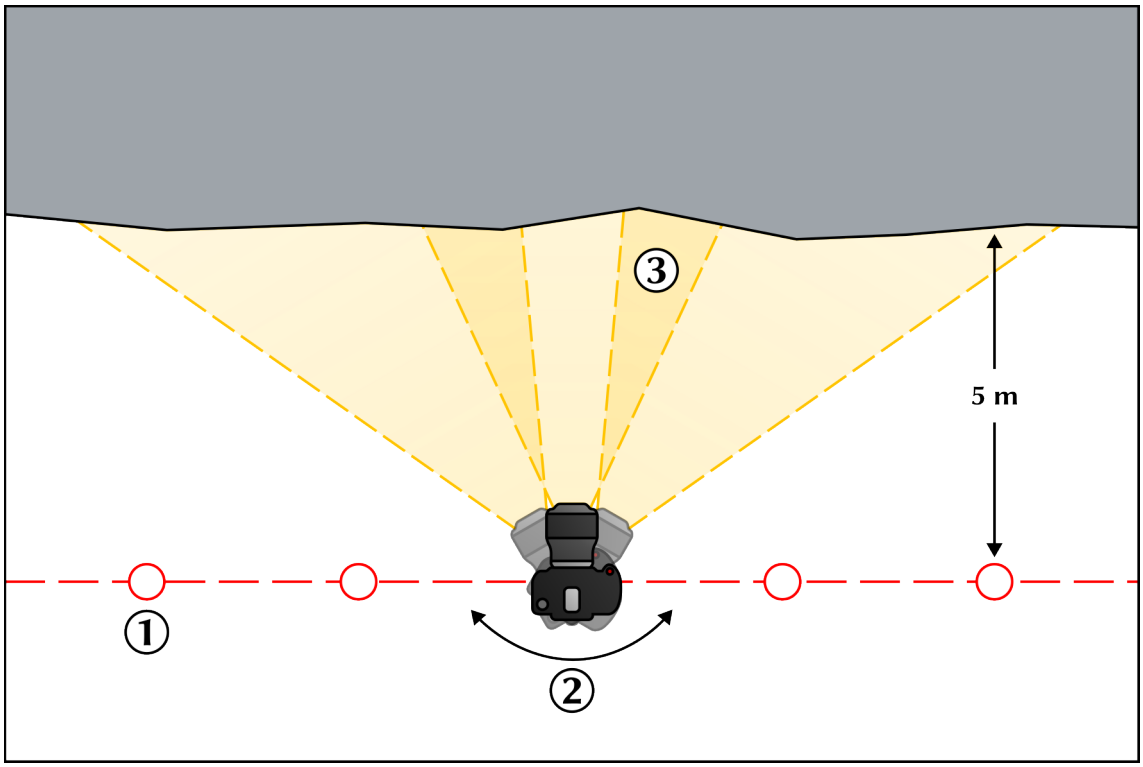

Figure 3.1 Top-down diagram of the field photography setup. **(1)** Positions along the transect, parallel to the quarry face, where photographs were taken. **(2)** Array of images taken at each step. **(3)** Image overlap required for photogrammetry matching.

The field photographs were processed using Agisoft Metashape Professional (version 2.2.1) to create a scaled and correctly orientated orthomosaic of the peperitic margin. The workflow followed a standard structure-from-motion photogrammetry (SfM) procedure. SfM is a low-cost, user-friendly photogrammetry technique that resolves three-dimensional structure from a sequence of overlapping, offset images (e.g., Westoby et al. 2012). It has previously been applied to a volcanic setting in reconstructing lava flows (Farquharson et al. 2015). Unlike conventional photogrammetry approaches, SfM automatically solves for scene geometry and camera orientation without the need to specify known three-dimensional locations. All photographs were imported into Metashape and aligned to derive a tie point cloud; each set of points representing the same physical feature in overlapping images. A mesh model was processed from these points, in which a true colour texture could be applied.

To scale the model, the reference objects placed in the field were identified in the aligned images. Markers were manually inserted at points on these references, for example, at each end of a metre rule. Scale bars of known length were defined between these markers. The accuracy of each scale bar was weighted based on the estimated uncertainty when placing the markers,

estimated at ±1 mm for the metre rules, and ±5 mm for the tape measure.

Metashape defaults to an arbitrary coordinate system for model orientation. The model was reorientated to define the quarry face as the XY plane, allowing an orthomosaic to be exported with the quarry face as the horizontal reference. Since the exposure is approximately planar but has significant irregularities, the XY plane was defined by calculating a best-fit plane through markers placed at random across the face. An orthomosaic view was produced from the scaled and orientated model and was exported as a TIFF (Figure 3.2). For a detailed visual overview of the photogrammetric workflow in Metashape, see Appendix A.

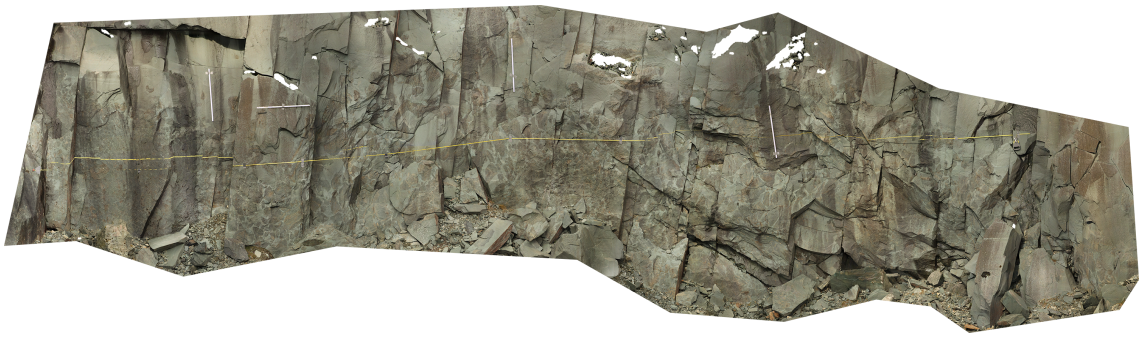

Figure 3.2 Low-resolution example orthomosaic of the main peperite exposure (Locality A) at Hopper Quarry, generated from a photographic survey processed in Agisoft Metashape. White areas show regions with insufficient data for image reconstruction. The metre rules and tape measure visible were used to scale the model.

3.1.2 Vesiculated clast imaging

A subsample of six juvenile clasts from Locality A was selected for detailed vesicle analysis. These clasts were chosen based on the availability of high-quality field imagery and are representative of the range of vesicle textures observed in the outcrop. This subsample includes: coarsely vesicular clasts, dominated by large vesicles; finely vesicular clasts, dominated by small vesicles; and mixed clasts, which display an intermediate range of both small and large vesicles. Close-up photographs were captured using the same DSLR and lens used for the quarry-scale imaging. Unlike the photogrammetry, where consistent camera settings were required to aid reconstruction, these images were captured using automatic exposure settings to prioritise individual image quality, lighting, and contrast. These images were subsequently used to produce vesicle size distributions.

3.2 Image Analysis

3.2.1 Clast outline delineation

Clasts were manually outlined from the orthomosaic of Locality A using Adobe Photoshop. Only clasts that were clearly visible and distinguishable from the surrounding matrix and other clasts were outlined, producing a large, spatially distributed sample of 798 individual particles. The Magnetic Lasso tool was used with the following settings: width set to 15 px, contrast at 10%, frequency at 80, and anti-aliasing disabled. Clasts were categorised into two groups based on the difficulty of outlining: Group A includes clasts with clear, well-defined geometries that could be traced unambiguously, while Group B includes clasts with more complex outlines, often requiring

subjective judgement during tracing. A map of the full distribution of clasts, including grouping, is shown in Figure 3.3.

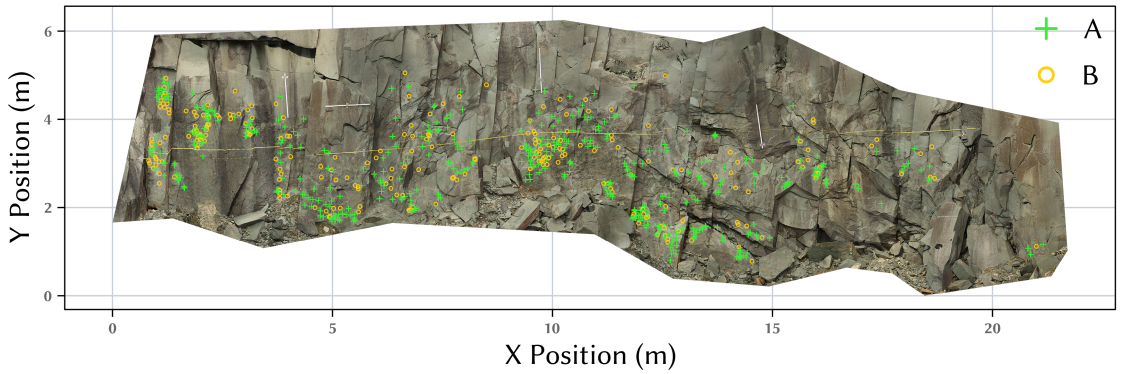

Figure 3.3 Map of clast coordinates, defined by the centroid, overlaid on the orthomosaic of Locality A at Hopper Quarry, providing a representative sample of the overall clast distribution. Group A represents clasts with clearly defined margins. Group B represents those with more ambiguous margins.

3.2.2 Clast shape analysis

The clast outline image was imported into FIJI, a distribution of ImageJ (Schindelin et al. 2012) for shape analysis. Image preparation involved converting the image to 8-bit greyscale, applying a threshold to isolate clasts, and setting the image scale. The spatial resolution was set to 0.35 mm px^{-1} based on the orthomosaic. Both primary geometric measurements (Table 3.1) and shape parameters, SPs, (Table 3.2) derived from them were used to quantify the shapes of clasts within the peperite exposure at Hopper Quarry. Additionally, the centroid of each clast was calculated to provide a local coordinate relative to the orthomosaic reference frame. The SPs measured were form factor (FF), solidity (SLD), convexity (CVX), and axial ratio (AxlR), following the methods of Liu et al. (2015). For more information on the SPs used, see Subsection 2.3.1.

The ImageJ macro provided in Liu et al. (2015) was modified for this study to improve convex hull calculations and customise scale setting and measurement outputs. The original macro relies on well-spaced particles; however, the crowded clast distribution inherent to the Hopper Quarry outcrop resulted in processing errors. Further details, along with the modified macro, are provided in Appendix C. A total of 798 clasts were outlined, however only clasts larger than a minimum critical pixel area defined by Liu et al. (2015) at 750 px were analysed, resulting in 731 analysed clasts. Of these, 494 were Group A, and 237 Group B. The complete dataset of clast measurements is provided in a supplementary excel file.

Table 3.1 Summary of primary measurements used for clast shape analysis.

Symbol	Definition
A_{clast}	Area of the clast
A_{ch}	Area of the convex hull (smallest convex polygon fully enclosing the clast)
P_{clast}	Perimeter of the clast
P_{ch}	Perimeter of the convex hull
a	Major axis of best-fit ellipse
b	Minor axis of best-fit ellipse

Table 3.2 Summary of shape parameter definitions and formulas used in clast shape analysis. Abbreviations of primary measurements are defined in Table 3.1 Modified from Liu et al. (2015).

Shape Parameter (SP)	Abbreviation	Formula	Definition	Sensitivity
Form Factor	FF	$\frac{4\pi A_{clast}}{{P_{clast}}^2}$	A measure of circularity; deviation from a circle is a result of elongation or increasing roughness	Form and roughness
Solidity	SLD	$\frac{A_{clast}}{A_{ch}}$	A measure of shape convexity. Values closer to 1 indicate a more solid, convex shape.	Roughness (morphological)
Convexity	CVX	$\frac{P_{ch}}{P_{clast}}$	A measure of perimeter smoothness. Values closer to 1 indicate a smoother shape.	Roughness (textural)
Axial Ratio	AxlR	$\frac{b}{a}$	A measure of elongation. Values closer to 1 indicate a more circular shape.	Form

3.2.3 Vesicle delineation and analysis

Vesicle cross-sections within the six individually photographed clasts were manually outlined using Adobe Photoshop. The pencil tool was set to 1 px to trace vesicle boundaries, which were then filled to produce discrete vesicle masks. Vesicle area was the primary metric measured in FIJI. Equally, the major and minor axes were calculated to measure axial ratios and elongation directions for both vesicles and their host clasts. Thus, patterns in vesicle orientation could be assessed. The SPs applied to clasts were not used for vesicle analysis due to image resolution limitations. The requirement to image a full clast resulted in vesicle pixel counts below the minimum critical threshold of 750 px established by Liu et al. (2015). A macro was developed to automate this process for each clast. Further details, along with the macro, are provided in Appendix C. The complete dataset of vesicle measurements is provided in a supplementary excel file.

3.3 Uncertainties and errors in morphometric and textural analyses

Uncertainties related to the morphometric and textural analysis of peperite clasts result from user subjectivity, stereological constraints, technical limitations, sample variability, and possible non-representativeness. These factors influenced both the accuracy of primary measurements and the reliability of metrics derived from them. The following subsections evaluate the magnitude of these uncertainties and the implications and assumptions made during data interpretation.

3.3.1 User-driven uncertainties

Manual outlining of clasts and vesicles in Adobe Photoshop introduced random error into the primary measurements. Such errors resulted from inconsistencies in hand movement and subjective judgements of clast and vesicle boundaries, especially where margins were weathered or poorly defined. These uncertainties were propagated into derived metrics, such as the clast shape parameter values.

To quantify the user-driven uncertainty of manual clast outlining, representative clasts from both Group A (clear, well-defined geometry) and Group B (ambiguous, complex, or weathered outlines) were each traced five times independently. The resulting outlines were analysed in FIJI to calculate primary measurements and shape parameters, and variability between independent tracings was quantified using the coefficient of variation using the sample standard deviation and mean (Equation 3.1). Results are presented in Figure 3.4.

$$CV = \frac{\sigma}{\mu} \times 100\% \tag{3.1}$$

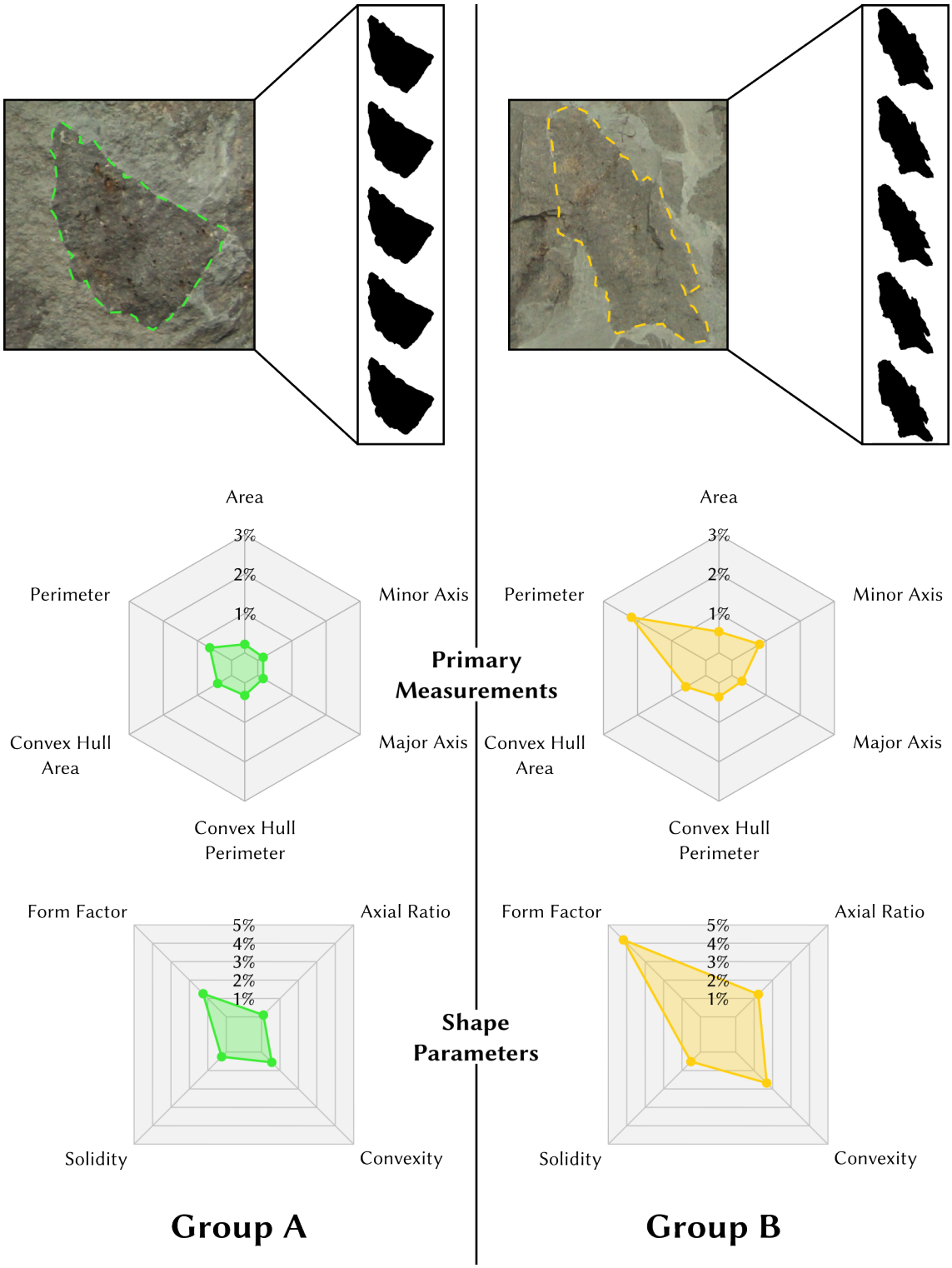

Figure 3.4 Radar charts showing the coefficient of variation for primary measurements and shape parameters of two different clasts that were repeatedly traced, quantifying the uncertainty of manual tracing. The Group A clast represents clasts with clearly defined margins. The Group B clast represents those with more ambiguous margins.

3.3.2 Stereological constraints

A fundamental limitation of image analysis is the use of two-dimensional (2D) imagery to represent three-dimensional (3D) objects. 2D images, whether at thin-section or outcrop scale, may not be representative of particle shape and abundance in the third dimension. Sections cut through polydisperse particles encounter two geometric biases: cut effect dictates how particles are not likely to be cut routinely through their largest area, and intersection probability describes how smaller particles have a lower probability of being intersected than larger ones (Shea et al. 2010). These flaws are exaggerated by elongate particles, where the apparent shape relies heavily on particle orientation. Consequently, inferring 3D morphologies from 2D images requires the assumption that particle morphology is homogenous in all orientations.

3.3.3 Technical limitations

Some uncertainties were independent of the user, and instead are inherent to the image resolution. Due to the limited number of pixels per vesicle when taking an image of a whole clast, the SP metrics calculated for clasts could not be accurately applied; many vesicles fell below the minimum critical pixel area of 750 defined by Liu et al. (2015), with the finest vesicles occupying fewer than ten pixels. Below this value, shape parameter sensitivity to resolution is found to increase significantly. Consequently, vesicle size, calculated as area, was the primary metric measured with confidence.

3.3.4 Sample variability and representativeness

Clasts within Locality A show heterogeneity in size and shape, resulting in sample variability. Due to weathering, not all clasts could be identified uniformly across the exposure. The sample is assumed to be representative of the full clast population due to the large number of recorded clasts (798) and their wide spatial distribution. Additionally, vesicle representation is complicated due to secondary mineralisation, where most are infilled with chlorite or epidote becoming amygdules. Amygdules have greater contrast against the pale groundmass, making vesicle identification and delineation simpler. This introduces a potential preservation bias, favouring the measurement of infilled vesicles.

A broader geological uncertainty exists regarding the location of the sill margin, which is not exposed in Hopper Quarry. To mitigate this, height within the exposure was used as proxy for relative distance from the sill margin during spatial analysis.

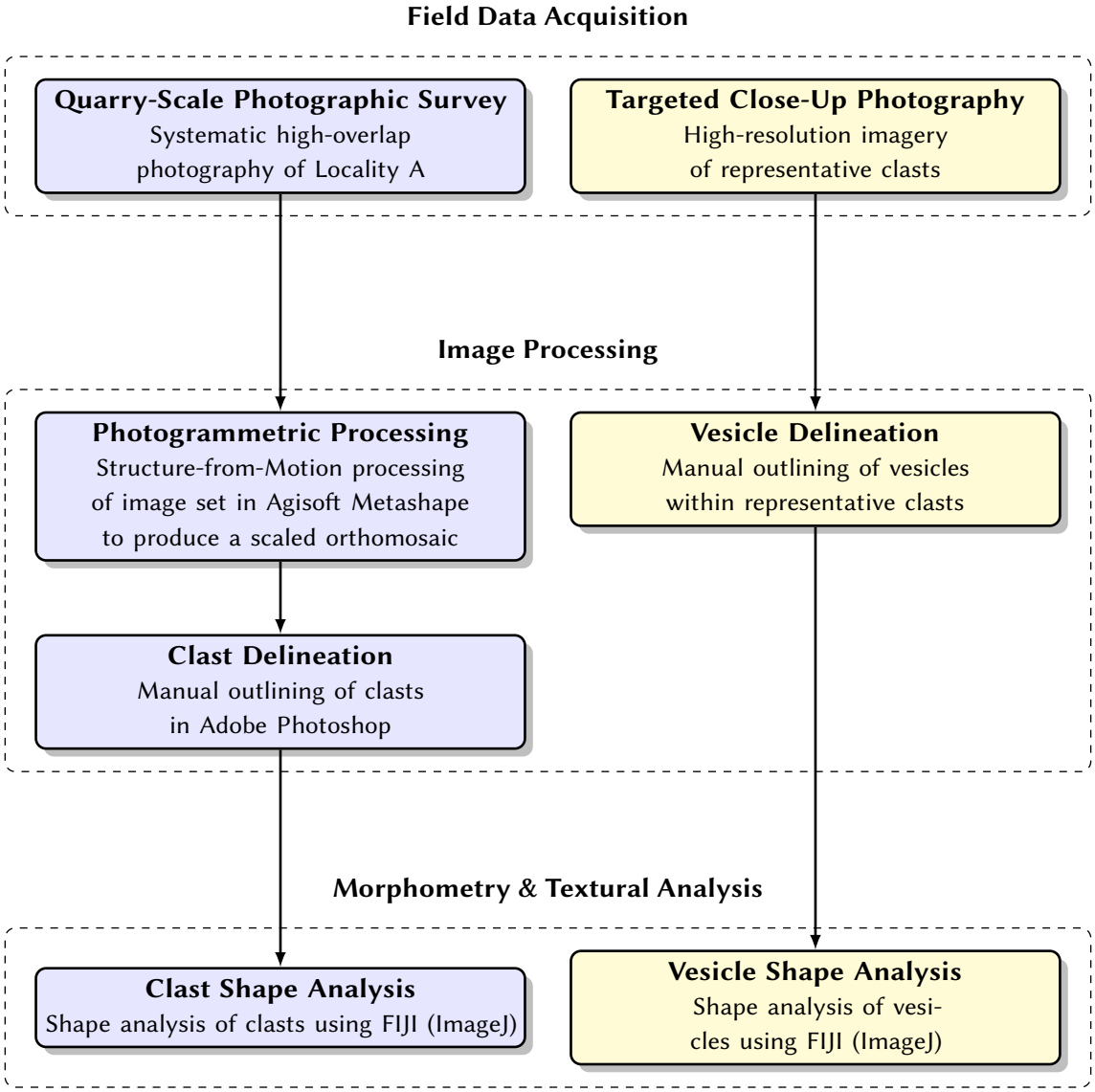

Figure 3.5 Flowchart of the complete methods workflow, divided into clast workflow (blue) and vesicle workflow (yellow).

Chapter 4

Results

This chapter first presents the qualitative field observations from Hopper Quarry, covering peperite morphology, sediment properties, and the overall architecture of the peperite exposure. This provides a contextual basis for the following quantitative results of clast and vesicle morphometry. Also presented is the geochemistry of a clast sample obtained through XRF spectrometry.

4.1 Field observations

4.1.1 Architecture of the peperite exposure

The north-west face of Hopper Quarry, approximately 60 m in width and up to 15 m in height, exposes dark andesitic peperite intruding into a bluish-grey volcaniclastic sandstone host. Within the full extent of the quarry, a section measuring 22 m long and 6 m high provides the clearest display of the peperitic margin (Locality A) (Figure 4.1). This margin is highly irregular relative to the overlying volcaniclastic sandstone bedding; it is lobate and varies in visible thickness, forming the lower 1 to 5 m of the quarry face. The non-brecciated centre of the sill is not exposed but is inferred to lie less than 5 m below the quarry floor. The overlying slate occupies the remaining height of the quarry face and is capped by a white slickenside fault surface displaying slickenlines. Though the dip of the sill cannot be directly measured, it is assumed to be parallel to the sill exposed at Dubbs Quarry, which dips at approximately 40° towards 150°. The principal axis of regional tectonic shortening is interpreted to be perpendicular to the quarry face. Therefore, the visible two-dimensional geometries are assumed to reflect emplacement processes rather than tectonic deformation.

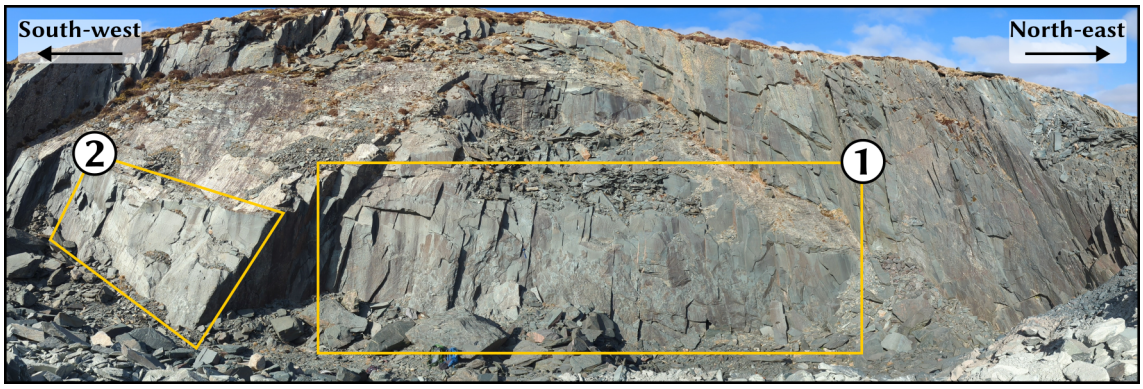

Figure 4.1 Panorama of the north-west face of Hopper Quarry, highlighting the locations of **(1)** Locality A, which shows the clearest peperite margin, and **(2)** Locality B, which shows examples of clast-sediment interaction. The coherent sill body is inferred to be several metres below the quarry floor.

4.1.2 Juvenile clast morphology and texture

Juvenile clasts show a wide range of shape and size. Overall form varies from simple, often geometric shapes (e.g., sub-circular or polygonal) to highly complex. Cross-section diameters range from less than 10 mm to greater than 500 mm, corresponding to a size distribution of lapilli through to large blocks. Clast size does not vary systematically with height above the intrusion, nor are there any other quarry-wide patterns to size distribution visible; however, clasts of a similar size are often locally grouped. Clasts are bound by generally angular, planar to curviplanar margins consistent with descriptions of blocky peperite. Many display sharp, well-defined edges, while some have highly irregular and embayed edges associated with vesiculated margins (Figure 4.2a). Adjacent to some highly irregular clasts are clusters of very small sediment supported clasts.

The exposure includes a mixture of clast vesicularity ranging from non-vesicular to highly vesicular. These can be categorised into three main textures: (1) non-vesicular clasts, which lack macroscopic vesicles; (2) finely vesicular clasts characterised by small vesicles <1-3 mm in diameter; and (3) coarsely vesicular clasts containing larger vesicles up to several tens of millimetres in diameter (Figure 4.3a-c). There is no clear spatial organisation to these textures, with non-, finely, and coarsely vesicular clasts occurring adjacent to one another in a random arrangement (Figure 4.3d).

Vesicle shapes range from spherical or ellipsoidal to complex, coalesced bulbous forms. Most are ellipsoidal, although the degree of elongation will depend strongly on the plane of observation. Within individual clasts, size distributions are generally spatially uniform, typically showing no vesicle zoning. Some heterogeneous distributions occur in which vesicle size grades linearly across the clast, independent of clast margins or geometry (Figure 4.3e). The major axes of most vesicles are aligned preferentially. The vesicles are most often amygdules, infilled with black chlorite and epidote. Coarser vesicles are often empty, having been weathered out or mechanically dislodged. Highly vesicular clasts are typically bounded by vesiculated, highly irregular margins (Figure 4.2a,c). Here, vesicles intersected by the clast margin have been filled with host sediment which is somewhat lighter in colour than the sediment matrix between clasts.

Clast dispersal varies across the exposure but generally displays a grading of less to more dispersed with increasing height, thus increasing distance from the sill. Much of the central to lower exposure is clast-rich and closely packed. While individual clasts appear separated by small distances of sub-cm range in 2D (Figure 4.2d), this is likely an artifact of the viewing plane. In 3D,

these clasts likely form a framework supported texture, where clasts support one another. There are many examples of jigsaw-fit texture in the closely packed peperite (Figure 4.2b). However, most of the exposure appears to be disturbed. Disturbance ranges from slight modification of jigsaw-fit textures by rotation to highly chaotic arrangements where clast margins cannot be matched. Higher in the exposure, clasts are more widely dispersed and are fully sediment supported, with separation distances approaching metre scale.

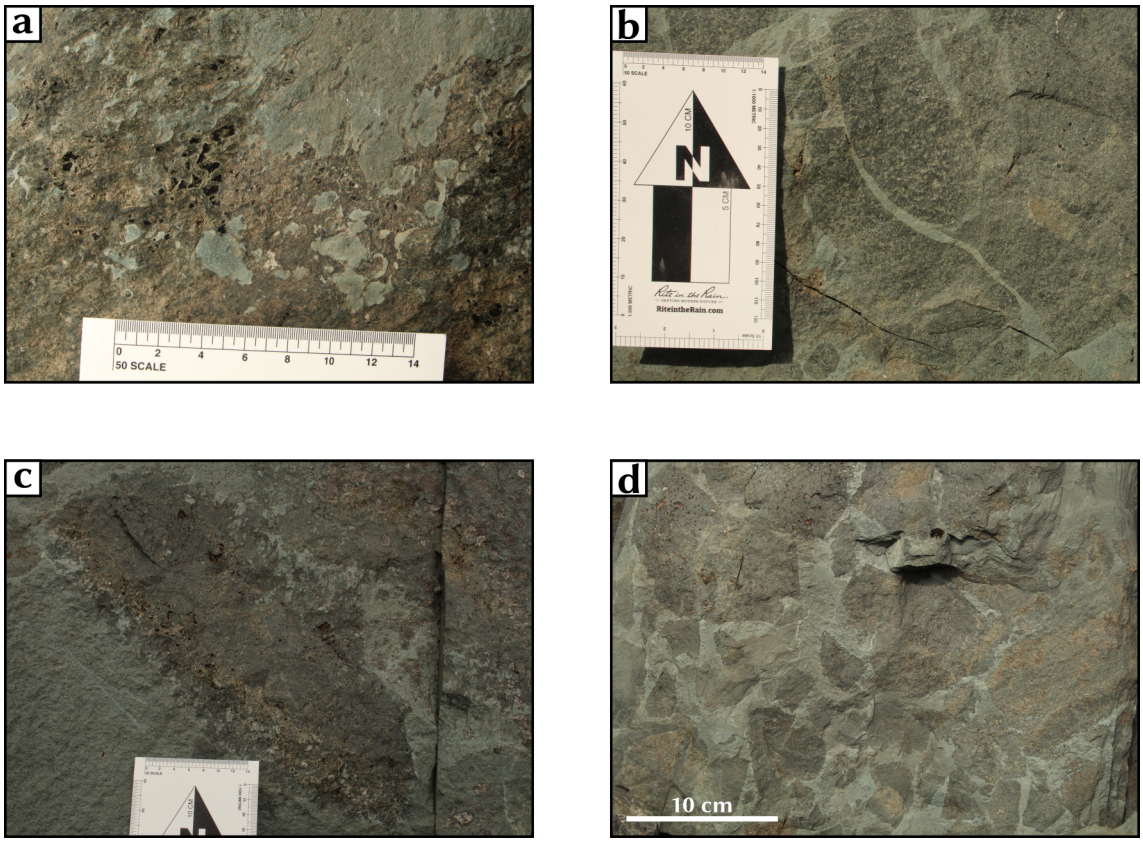

Figure 4.2 Variety of clast margins at Hopper Quarry. **(a)** Highly irregular vesicular margin of an andesite block with sediment filled vesicles, indicating a high degree of host interaction with the magma. **(b)** Jigsaw-fit textures of adjacent clasts with well-defined planar to curviplanar margins; clast margins are matched across narrow, matrix filled fractures typical of in situ brecciation. **(c)** A large block with an irregular, vesiculated margin. Such morphological types appear less frequently than the planar-margined clasts. **(d)** Closely packed angular clasts towards the base of the exposure, typical of a blocky peperite. While separated by small distances in 2D, closely packed clasts are likely framework supported in 3D, with a higher degree of dispersal at increasing distance from the sill.

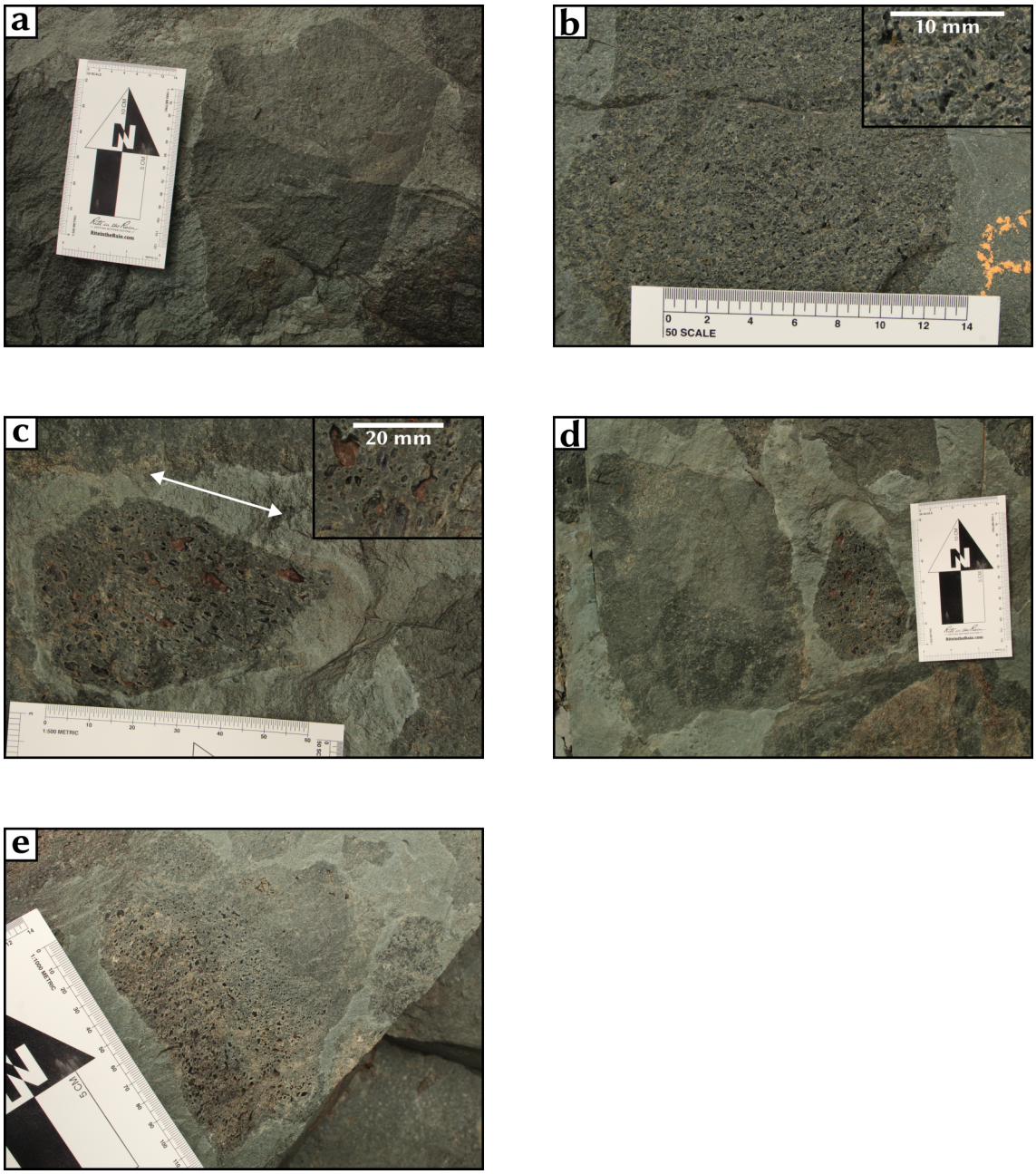

Figure 4.3 Vesicular clast textures. **(a)** Non-vesicular block. **(b)** Finely vesicular block with a magnified inset. **(c)** Coarsely vesicular block with a magnified inset. The majority of vesicles are preserved as black chlorite and epidote filled amygdules, though larger voids appear empty - likely plucked - and brownish in hue. **(d)** Clasts displaying a non-systematic distribution of vesicularity; coarsely and finely vesicular clasts occur adjacently. This trend is visible across the exposure. **(e)** Heterogeneous vesicle size distribution within a clast, with vesicles grading from larger on the left to smaller on the right. White arrow indicates a clearly visible preferred vesicle orientation.

4.1.3 Host sediment relationships

Characteristics of the host sediment are well displayed in a section of the quarry face adjacent to Locality A. This section is hereafter referred to as Locality B (Figure 4.1). Here, interactions between sediment and intrusive material preserve a chronology of events. The margin between the peperite domain and adjacent sediment is generally concordant with bedding; however, bedding is locally truncated where clast clusters have cross-cut the sediment (Figure 4.4c). Within the peperite domain, primary sedimentary structures are absent. Some clasts are surrounded by a rim of homogenised sediment that is lighter in colour than the surrounding matrix. The sediment matrix also shows bulk colour variations, with defined boundaries between areas of contrasting colour (Figure 4.4d).

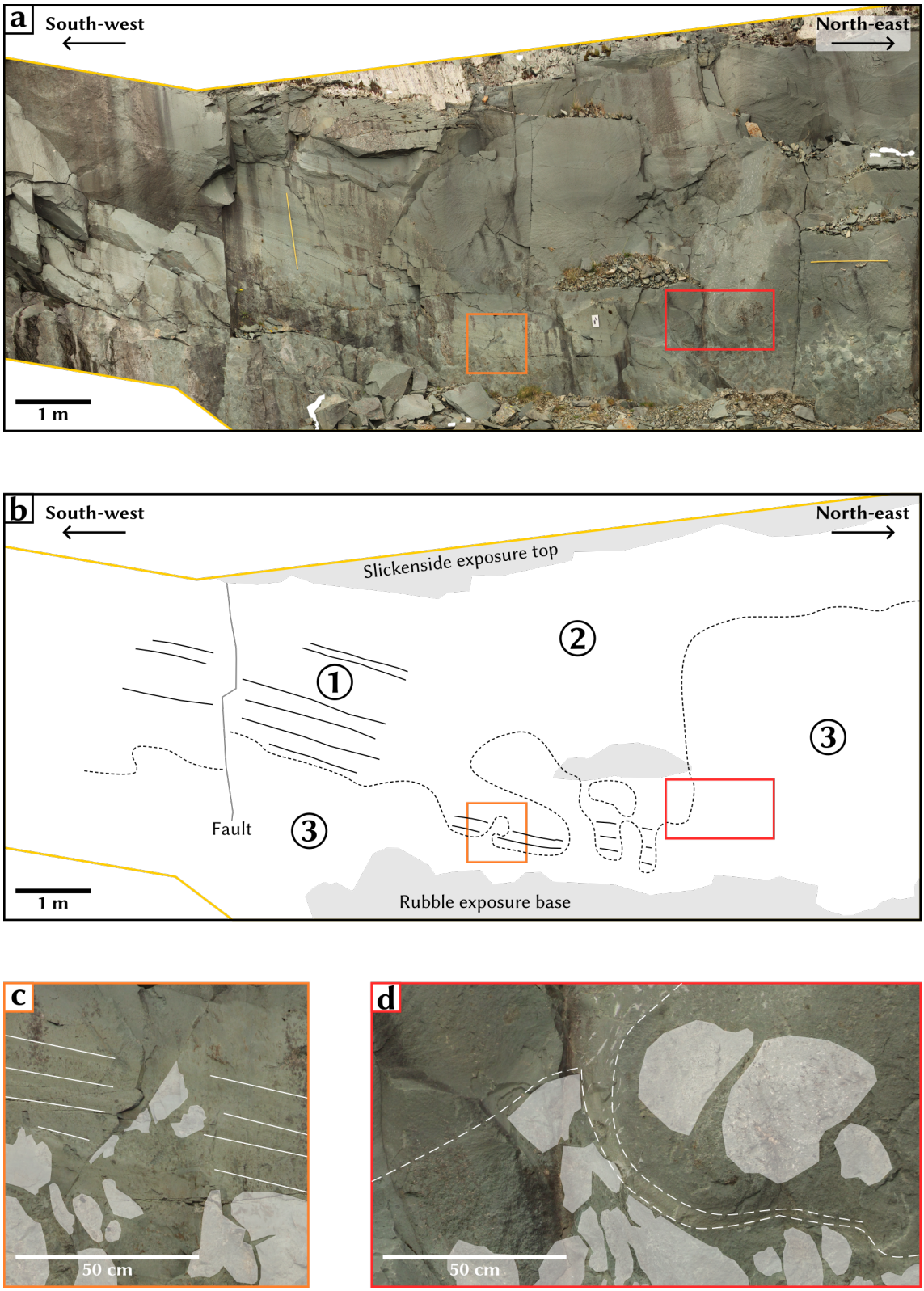

Figure 4.4 Locality B: an exposed peperite margin at Hopper Quarry showing various host sediment relationships. **(a)** Orthomosaic of the locality. **(b)** Field sketch of the exposure showing **(1)** undisturbed bedding (solid lines) above the peperite margin (dashed lines), **(2)** massive slate domain where sedimentary structures are not visible, **(3)** mixed peperite clasts and host sediment. Sedimentary structures adjacent to the peperite have been destroyed, with inset **(c)** displaying bedding truncated by clasts. Inset **(d)** displays three areas with different sediment matrix colour, roughly marked by dashed white lines. The cross-cutting relationships of these areas indicate a multi-stage chronology.

4.2 Clast morphometry

Quantitative morphometry was performed on a sample of 731 peperite clast outlines measured from the orthomosaic of Locality A at Hopper Quarry. The following sections present distributions, relationships, and spatial variations among clast size and shape.

4.2.1 Clast size and shape distributions

Histograms and cumulative frequency plots are used to present the distributions of clast size and shape. Histograms effectively visualise general trends within the data but can introduce bias from bin size selection. Cumulative frequency plots display the raw data directly, removing this bias and allowing cross comparison between datasets.

Figure 4.5 shows the size distribution of clasts represented by two units: area (m^2) and Krumbein phi (ϕ), where $\phi = -\log_2(d\ [\text{mm}])$ (Krumbein 1936). Clast diameter was calculated directly from area, expressed as equivalent circular diameter (mm). Area was binned in $\log_{10}$ space at intervals of 0.25, while phi values were binned at 0.25 ϕ, allowing comparison with other volcanic grain size data. The log-transformed histograms display a broadly unimodal distribution with a dominant peak at approximately 0.004 m^2 or -6 ϕ. The distribution has a moderately positive (right) skew, where the frequency of clasts tapers gradually towards larger sizes. The median clast size is 0.002 m^2 (-5.67 ϕ). The range spans 3.44 orders of magnitude, from a minimum recorded value of 9.58×10^{-5} m^2 to a maximum of 0.265 m^2 (-9.18 ϕ to 3.47 ϕ). The cumulative curve rises generally linearly until the 75th percentile, where slope gradually decreases towards the largest clasts.

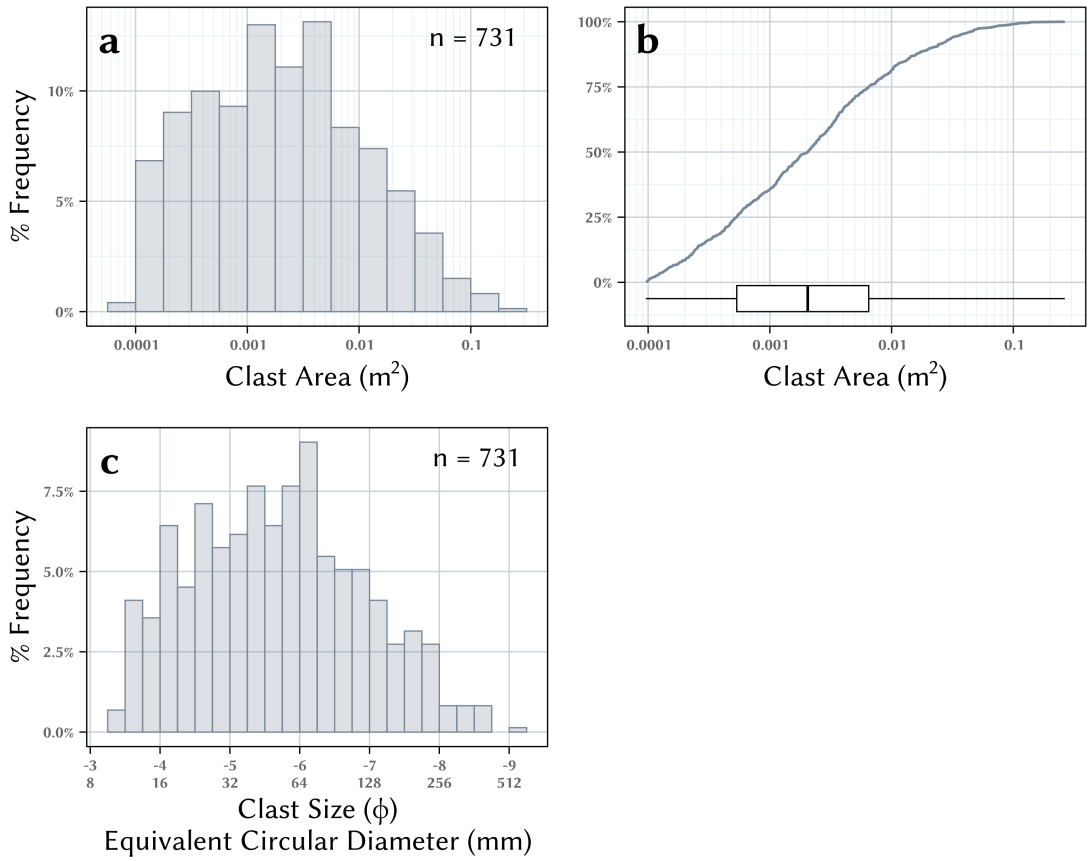

Figure 4.5 Number distribution of clast size measured on a sample of outlined peperite clasts from Hopper Quarry. **(a, b)** show size distributions in area (m²). **(c)** shows size distribution in equivalent circular diameter (mm) and Krumbein phi scale (ϕ). The distribution is characterised by a broad unimodal peak at approximately 0.004 m^2 or -6 ϕ with a positive (right) skew.

A measure of dispersion is provided by Inman's sorting coefficient (Equation 4.1) (Inman 1952), where ϕ_{16} and ϕ_{84} are the 16th and 84th percentiles of the size distribution in phi units. This quantifies the degree of sorting in the clast size distribution, allowing for comparison with other grain size distributions. For the clasts analysed, the Inman sorting coefficient (σ_ϕ) was calculated as 1.3 ϕ. This value denotes a poorly sorted distribution.

$$\sigma_\phi = \frac{1}{2}(\phi_{84} - \phi_{16}) \tag{4.1}$$

Distributions of the four shape parameters (SPs) used to quantify clast shape - form factor (FF), solidity (SLD), convexity (CVX), and axial ratio (AxlR) - are shown in Figure 4.6. As ratios, these parameters are confined between 0 and 1, where 1 represents a perfect circle. FF reflects overall irregularity, being sensitive to both elongation and roughness. SLD is sensitive to large-scale morphological roughness, whereas CVX captures small-scale textural roughness. AxlR describes clast elongation. The distribution of FF is roughly symmetrical, with a range of 0.18 to 0.86. SLD and CVX are both strongly negatively (left) skewed, with respective ranges of 0.54 to 0.97 and 0.92 to 0.99. AxlR shows a roughly symmetrical distribution with a minor negative (left) skew and a range of 0.14 to 0.99. All distributions are unimodal, and the ranges reported refer to the full observed data.

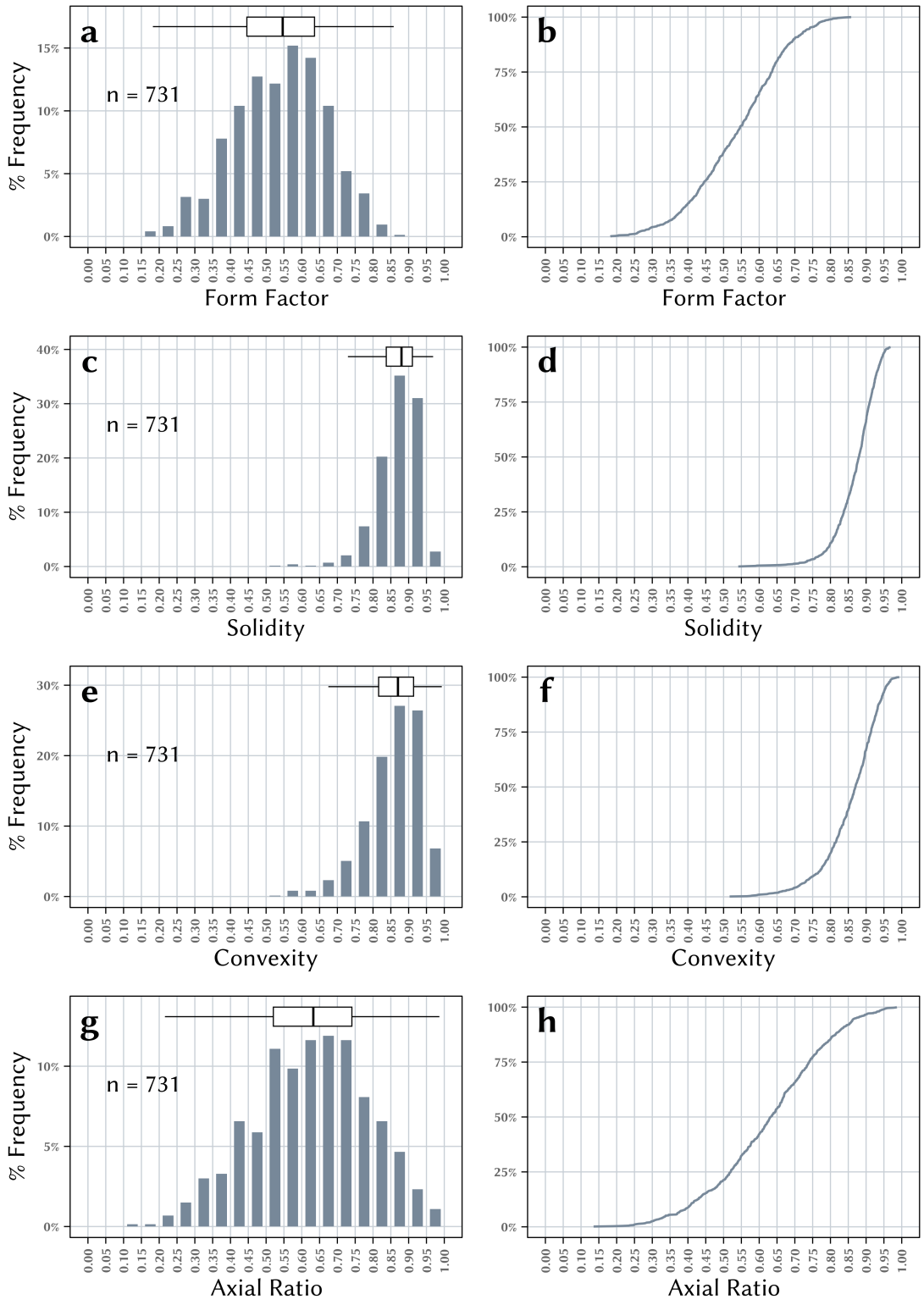

Figure 4.6 Number distributions of the 2D shape parameters **(a, b)** form factor, **(c, d)** solidity, **(e, f)** convexity, and **(g, h)** axial ratio, measured on a sample of outlined peperite clasts from Hopper Quarry. All distributions are unimodal. Form factor and axial ratio are roughly symmetrical, whereas solidity and convexity have a strongly negative (left) skew.

4.2.2 Relationships between clast size and shape

Figure 4.7 compares clast size with the four SPs: FF, SLD, CVX, and AxlR. FF and AXlR show little apparent relationship with clast size. SLD displays a visually slight positive trend, while CVX shows a visually slight negative trend. Linear regressions were applied to the plots of log-transformed clast area against SLD and CVX to assess these visual trends. The coefficient of determination (R^2) for SLD against clast size is 0.011, indicating essentially no relationship. R^2 for CVX against clast size is 0.241, indicating a very weak relationship. Overall, trends are minimal and data points are broadly distributed. Therefore, it can be identified that clast irregularity is not a result of size, but is scale independent; smaller clasts are as irregular as larger clasts, and this thus points towards a common formation process.

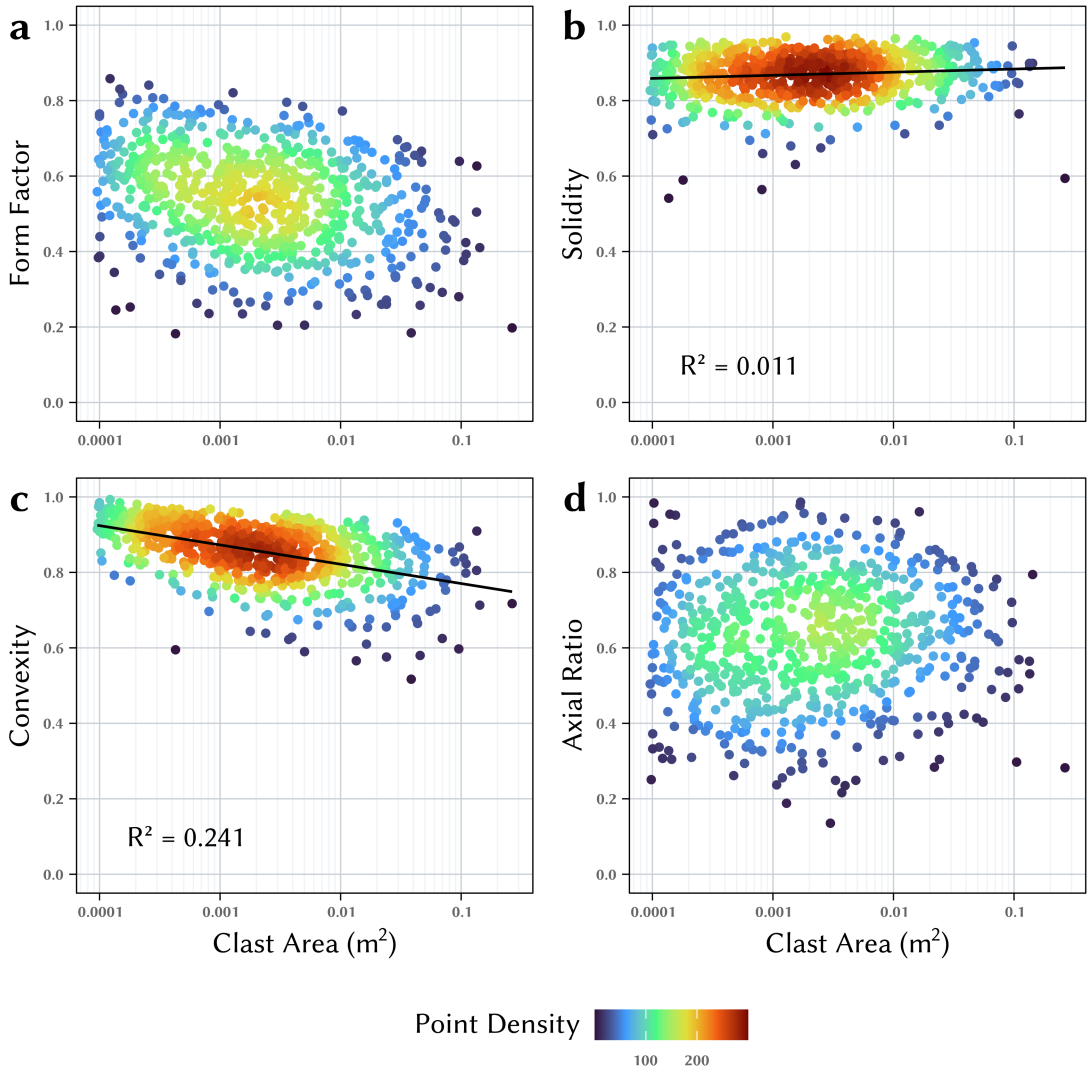

Figure 4.7 The relationship between clast area and four shape parameters: **(a)** form factor, **(b)** solidity, **(c)** convexity, and **(d)** axial ratio, measured on a sample of outlined peperite clasts from Hopper Quarry. Point density visualises the spread of points where many sample outlines overlap. Linear regressions are displayed as black lines. Trends are minimal and data points are broadly distributed.

Figure 4.8 plots clast area against perimeter, with both axes log transformed. The data shows a strong positive linear correlation, with a linear regression R^2 value of 0.979. Therefore, perimeter increases with area according to a power-law relationship, where a change in area results in a proportional change in perimeter. Again, this points towards clast irregularity being scale independent, with smaller clasts as irregular as larger clasts, indicative of a common formation process. The relationship parallels the reference functions for a perfect circle (orange) and an ellipse with aspect ratio 2:1 (blue). All clast data points lie above the function for a perfect circle, and almost all above the ellipse function; for a given area, measured clasts have a longer perimeter than the reference shapes. The gradient of the regression line is slightly steeper than those of the reference functions, i.e., perimeter increases slightly faster with area in the measured clasts compared to the reference shapes. Point colour represents FF, a measure of overall irregularity. Values close to 1 represent near-circular shapes, while values close to 0 correspond to highly irregular shapes; increased irregularity naturally increases perimeter for a given area.

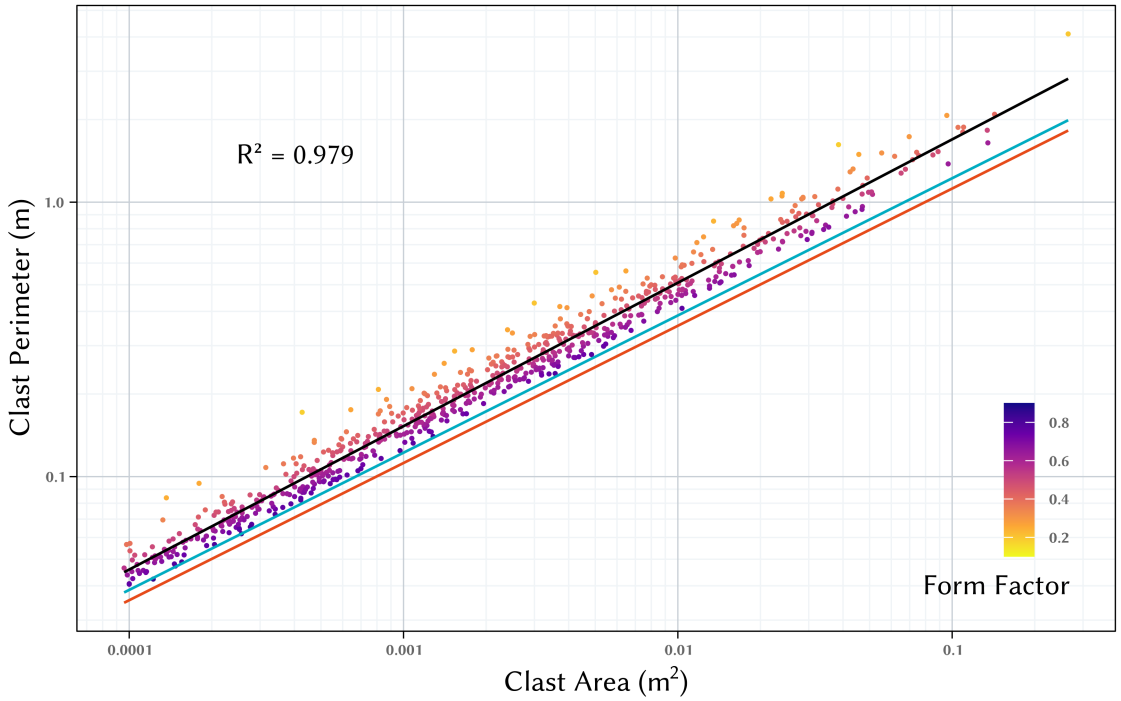

Figure 4.8 Log-log plot of Hopper Quarry clast size and perimeter. A linear regression (black line) highlights a strong power-law relationship. The data trend parallels the functions of a perfect circle (orange) and an ellipse with aspect ratio 2:1 (blue) but is displaced upwards. Point colour denotes Form Factor, a measure of clast irregularity, where 1 is a perfect circle.

Figure 4.9 shows the relationship between clast SLD and CVX, henceforth referred to as a SLD-CVX plot. SLD quantifies large-scale morphological roughness while CVX quantifies small-scale textural roughness. Both parameters are ratios ranging from 0 to 1, with 1 representing a perfectly smooth and convex shape (such as a circle). Values closer to 1 show less irregularity, whereas values closer to 0 show more irregularity. Representative clast outlines are displayed around the edge of the plot, and clearly show the differences in morphological and textural roughness. The distribution of clasts in SLD-CVX space forms a triangular cluster from near-perfectly convex and smooth shapes (SLD $\approx$ 1, CVX $\approx$ 1) towards more complex forms, reaching values just above 0.5 for both SPs. This triangular distribution shows an absence of clasts that have simultaneously high morphological roughness (low SLD) and high textural roughness (low CVX). Most clasts are concentrated at values of SLD $>$ 0.8 and CVX $>$ 0.75. The dashed line represents where SLD =

CVX. While the extent of the data spread is roughly symmetric about this line, the point density is visibly higher below the line, where SLD > CVX.

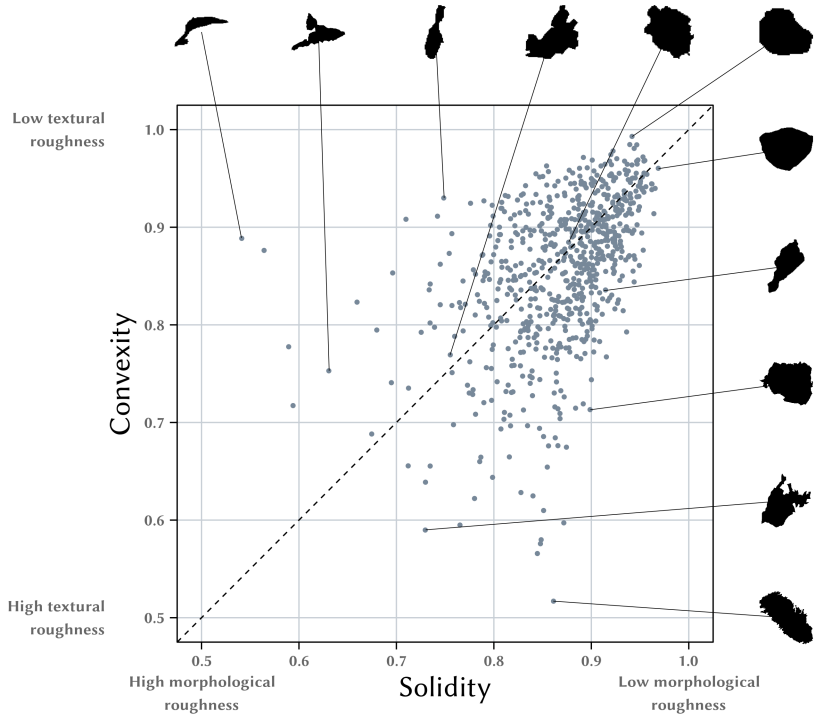

Figure 4.9 The relationship between solidity and convexity in Hopper Quarry clasts. Dashed line represents SLD = CVX. The reference clasts displayed around the edge of the plot clearly show the differences in morphological and textural roughness, as well as irregularity as a whole. The least irregular clasts appear in the top right. Clasts with large-scale irregularity features (morphological roughness) appear in the top left, whereas clasts with small-scale embayments (textural roughness) appear in the bottom right.

In addition to the standard solidity versus convexity plot (Figure 4.9), three variations were produced with a third continuous variable represented by point colour: FF, AxlR, and log-transformed clast area (Figure 4.10a-c). FF (a) shows a clear dependence on SLD and CVX, decreasing as both axes decrease. This aligns with definitions of the SPs: FF is sensitive to overall irregularity, whereas SLD and CVX capture large scale (morphological) and small-scale (textural) irregularity respectively. The AxlR plot (b) shows a heterogeneous colour distribution, indicating that elongation is independent of irregularity. The clast area plot (c) shows a general grading of smaller to larger clasts across the diagonal from top left (CVX > SLD) to the bottom right (SLD > CVX). This gradient appears continuous, though with some scatter, and suggests smaller clasts tend to have higher convexity values relative to solidity, and larger clasts the opposite.

To further quantify the multivariate relationship between SLD, CVX, and area, a fourth plot was produced in which the difference between SLD and CVX (Δ = SLD - CVX) is plotted against log-transformed clast area (Figure 4.10d). A dashed line representing $\Delta = 0$ (SLD = CVX) is included on plots (c) and (d) to illustrate the transformation. A linear regression of Δ against log(area) reveals a moderate positive correlation ($R^2 = 0.372$). An estimate of clast size at the $\Delta = 0$ transition was calculated. The median area for clasts in the range $-0.01 < \Delta < 0.01$ was chosen, producing a median clast size of 0.00128 m^2 (equivalent circular diameter 40.4 mm) at this morphological transition point.

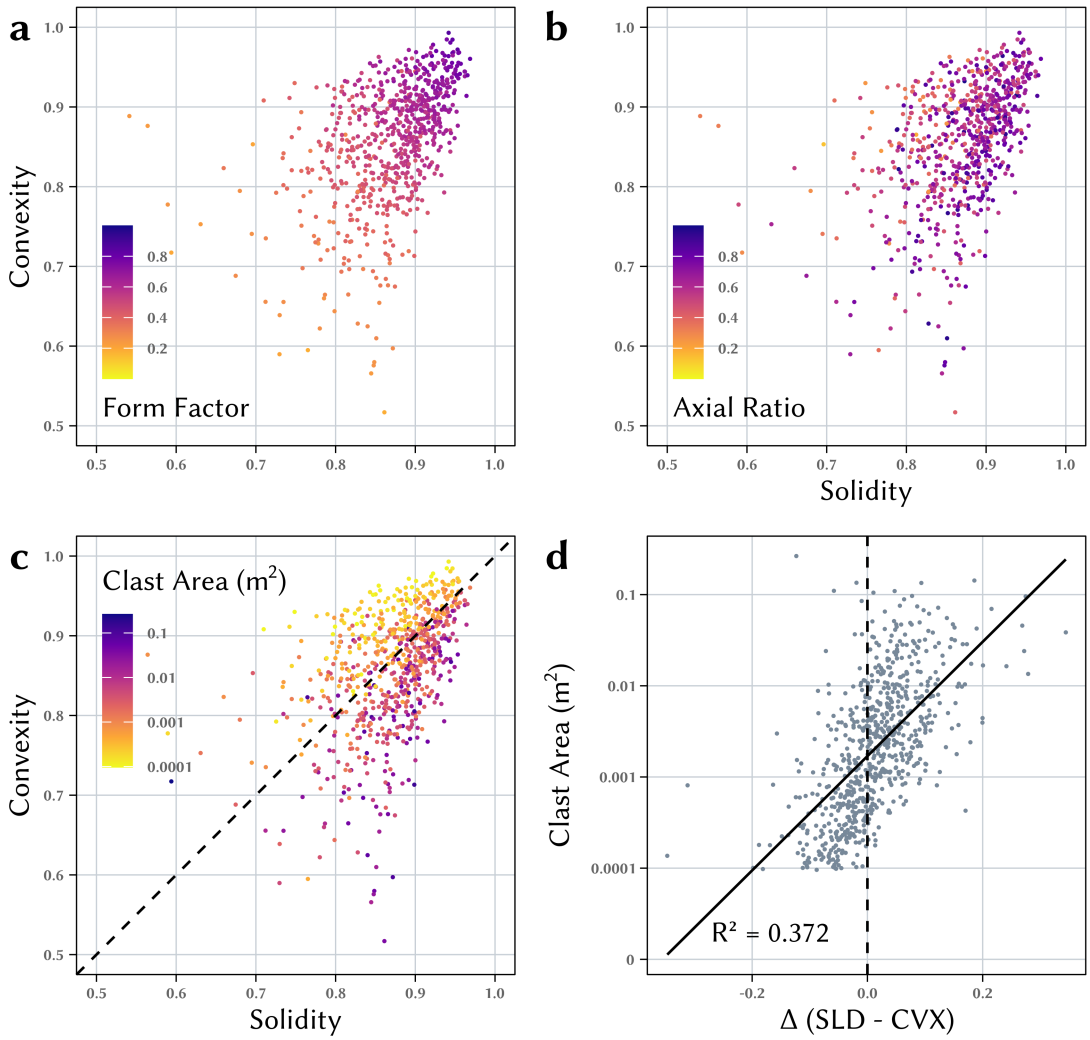

Figure 4.10 Solidity and convexity diagrams with a third parameter - **(a)** form factor, **(b)** axial ratio, and **(c)** clast area - displayed as point colour. Panel **(d)** shows Δ (SLD - CVX) versus clast area, with a linear regression applied. Dashed lines show SLD = CVX.

4.2.3 Spatial trends in clast morphometry

The relationship between clast size, shape (FF, SLD, CVX, and AxlR), and their vertical positions on the quarry face was analysed to identify potential gradients relative to the sill, with distance from the sill increasing with relative height in the exposure. The resulting scatter plots (Appendix D) show no gradient of clast size or shape against height in the exposure. Despite the absence of a correlation, such results are significant as they demonstrate a homogeneity of clast characteristics that are independent of height, and thus distance from the sill. This uniformity suggests a consistent fragmentation history, where the final vertical position of clasts is attributed to transport processes. This is discussed further in Section 5.3.

Spatial autocorrelation measures the degree to which values at one location are similar to values at nearby locations. Field observations suggest that clasts of similar size cluster as opposed to being randomly mixed. Spatial autocorrelation provides a statistically robust method for

verifying these observations, and quantifies the spatial scales at which these clusters operate.

Moran's *I* (Moran 1948) was calculated to measure the spatial autocorrelation of clast size (ϕ) across a series of 0.5 m wide lag distances, from 0 m to 5 m (Figure 4.11). A lag distance represents the range at which nearby clasts are considered neighbours. For example, if the Euclidean distance between two clast centroids is 0.3 m, that pair is allocated to the 0-0.5 m lag distance. Each point on the plot represents the midpoint of a lag distance. To assess statistical significance, a Monte Carlo permutation (n = 999) was performed for each lag distance. The yellow shaded region represents the null envelope (the 0.5 and 99.5 percentiles of the permutations). Values that fall outside of this range indicate a statistically significant spatial autocorrelation ($p<0.01$) that is highly unlikely to have occurred by chance.

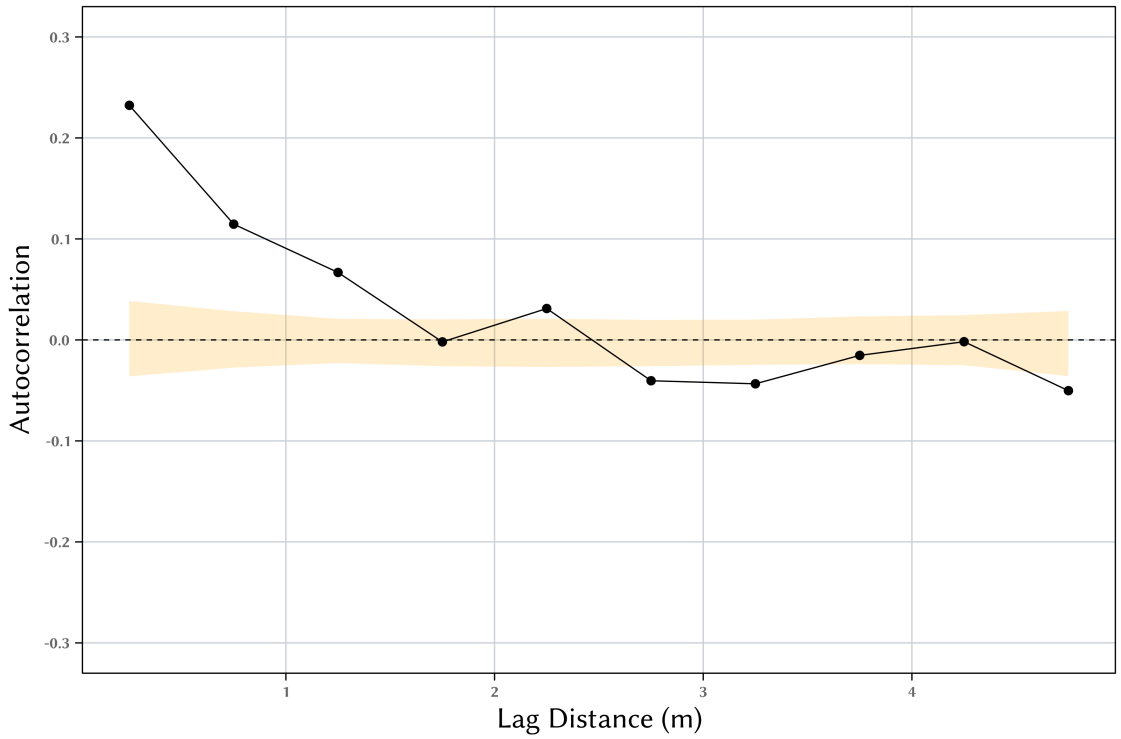

Figure 4.11 Moran's *I* correlogram for clast size (ϕ) across lag distances from 0 to 5 m. Points represent the observed Moran's *I* values for 0.5 m wide lag distances, plotted at their midpoint. The dashed line represents the expected value under a random spatial distribution. Values outside the null envelope (yellow shaded region) are statistically significant. Values closer to +1 indicate clustering of similar values, whereas values closer to -1 indicate clustering of dissimilar values. The positive autocorrelation at lag distances up to approximately 1.5 m indicates that clasts of similar size are clustered over this distance.

A Moran's *I* value of +1 indicates a perfect positive spatial autocorrelation, where similar values are perfectly clustered. A value of 0 indicates no spatial autocorrelation (random distribution), whereas a value of -1 indicates a perfect negative autocorrelation, where neighbouring values are very dissimilar. Figure 4.11 reveals significant positive spatial autocorrelation at small lag distances. Moran's *I* is at its maximum at the smallest lag distance of 0 to 0.5 m, where $I \approx 0.23$. This shows that clasts of similar sizes are significantly clustered between these distances. As lag distance increases, the degree of autocorrelation declines. Beyond 1.5 m, the observed Moran's *I* values fluctuate within or slightly below the null envelope indicating that clast size distribution becomes random at or above these distances. Overall, it can be determined that the mechanisms governing clustering of clast size operate over a localised, up to metre-scale range.

4.3 Vesicle morphometry

4.3.1 Vesicle size distributions

Figure 4.12 shows the vesicle size distributions for six clasts, which were visually categorised as coarsely vesicular, finely vesicular, or mixed. The distributions are presented as box plots and frequency histograms in panel (a) to effectively visualise general trends, and as cumulative frequencies in panel (b) to display the raw data directly. Vesicle size, plotted as equivalent circular diameter, spans two orders of magnitude from approximately 0.1 mm to 10 mm. The distributions are unimodal and broadly symmetric. Coarse clasts display a slight positive skew, with longer right tails. This quantitative analysis aligns with the initial visual classification, showing a clear separation between the three categories. The fine clast's distribution is distinctly offset towards the smaller diameters, while the coarse clasts form a group containing the largest vesicles. The mixed clast distributions fall neatly between the fine and coarse samples.

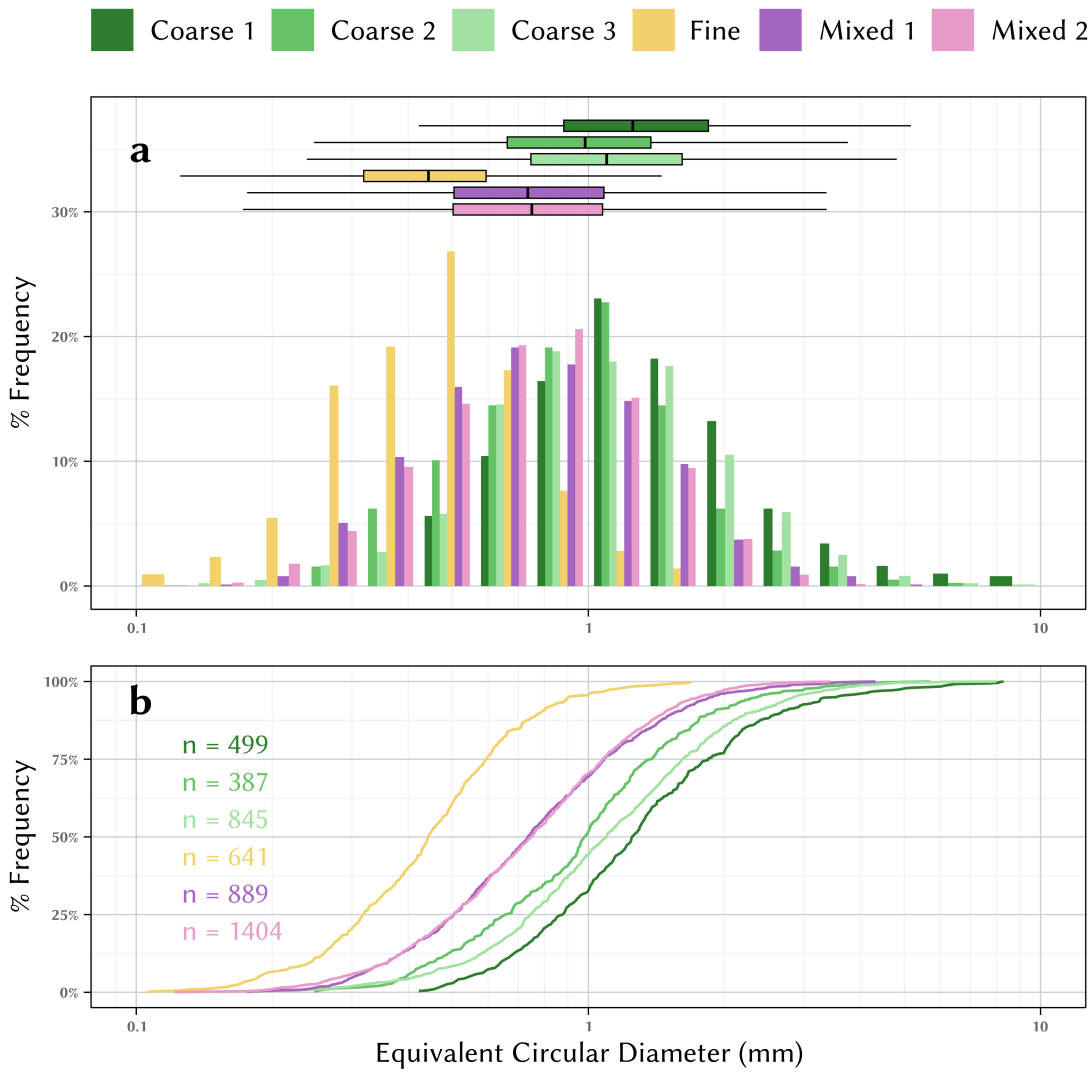

Figure 4.12 Vesicle size distributions in six clasts, visually classified as coarsely vesicular, finely vesicular, or mixed. Distributions are unimodal and broadly symmetric. There is a clear separation in vesicle size between the three categories; fine clasts are offset towards the smaller diameters, coarse clasts are offset towards the larger diameters, and mixed clasts fall in-between.

Figure 4.13 presents the vesicle size distributions weighted by estimated volume fraction. Volume distributions provide insights into bubble growth and coalescence. As such, the nucleation histories of the categorised vesicular clasts can be compared. It is critical to note that these volumes represent rudimentary conversions derived directly from the two-dimensional areas of vesicles. Due to resolution constraints, full vesicle number densities could not be calculated, and thus stereological 2D to 3D conversions such as Shea et al. (2010) could not be applied. Consequently, these results systematically under-represent the abundance of small vesicles. Despite these limitations, several general trends are observable. The fine clast displays a unimodal distribution restricted to smaller diameters. In contrast, the coarse clasts exhibit a bimodal or heavily negatively skewed distribution, characterised by a secondary peak at the largest diameters. Mixed clasts show a transitional distribution, with one sample showing a secondary peak similar to the coarse clasts.

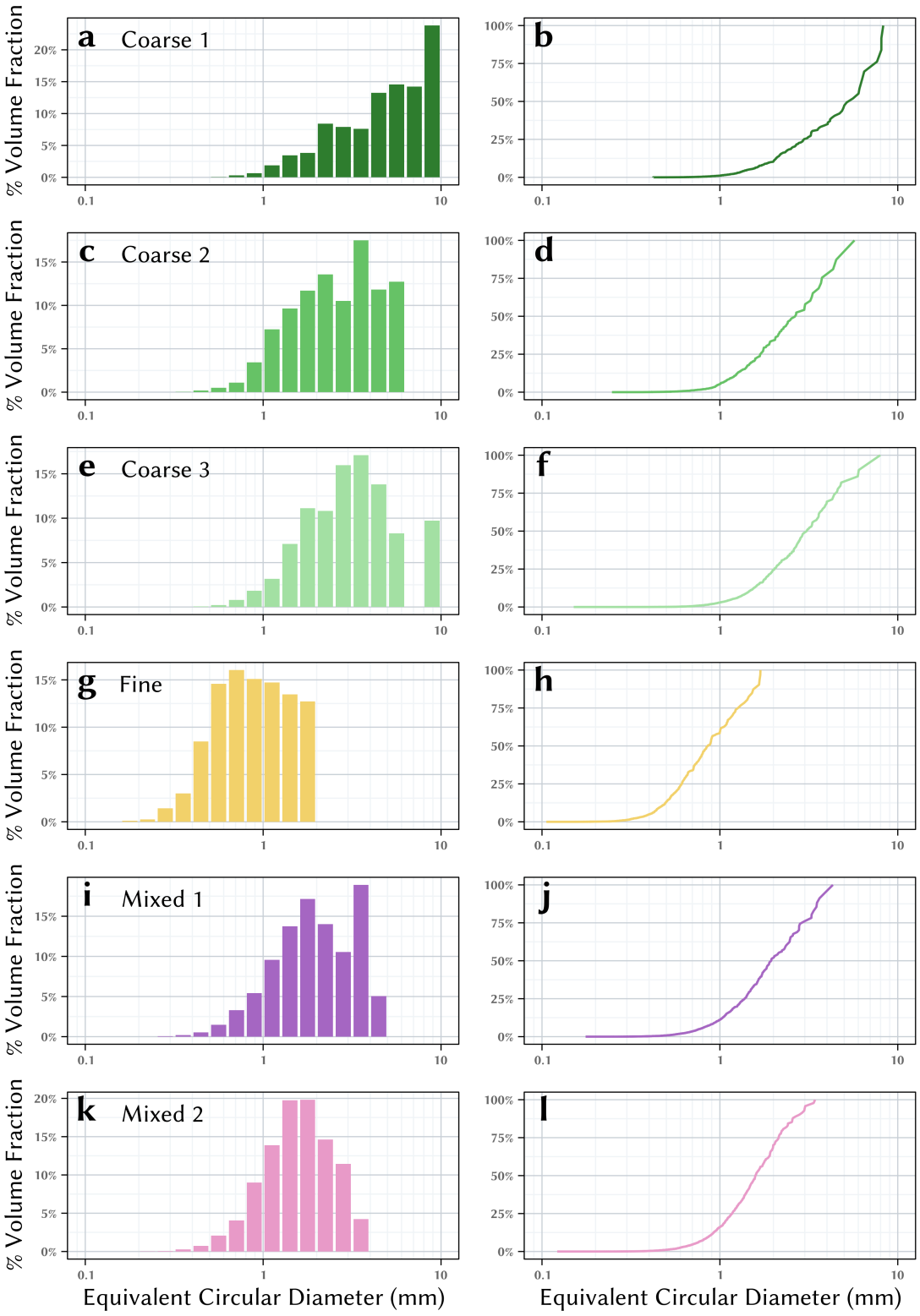

Figure 4.13 Vesicle size distributions as volume fraction in six clasts, visually classified as coarsely vesicular, finely vesicular, or mixed. Note that volumes are estimates derived from 2D areas without stereological correction, hence the abundance of small vesicles is systematically under-represented. Distributions are generally unimodal, though the coarse and one mixed clast show an additional peak at the largest diameters. The coarse distributions are more heavily skewed than the mixed or fine distributions.

4.3.2 Vesicle fabrics

Figure 4.14 presents rose diagrams of the apparent preferred orientation of vesicles in the six studied clasts. Vesicle orientation is defined as the angle of the major axis relative to the horizontal axis of the source image, which itself is not orientated to a fixed geographical horizon. Vesicles with an axial ratio ≥ 0.8 were excluded from the dataset to remove noise from those that are near-circular, with the final count per clast denoted as n. The orientation data is grouped into 10° bins, with the length of each bin representing vesicle frequency. Absolute angles are not comparable between plots, as clasts have been rotated following fragmentation.

In all six samples, a strong preferred orientation of vesicles is evident. The orientations also roughly correspond to the apparent orientation angle of the host clast, denoted by the dashed line. Furthermore, the degree of orientation clustering appears to correlate with median vesicle size, M, measured as equivalent circular diameter (mm). Coarsely vesicular clasts, which contain the largest vesicles, display the tightest distribution clusters. Mixed and fine samples display visibly wider distribution clusters with decreasing vesicle size, showing a weaker, though still strong preferred orientation. This systematic alignment suggests that a consistent strain mechanism drove vesicle elongation; potential mechanisms and their timing are discussed in Section 5.1.

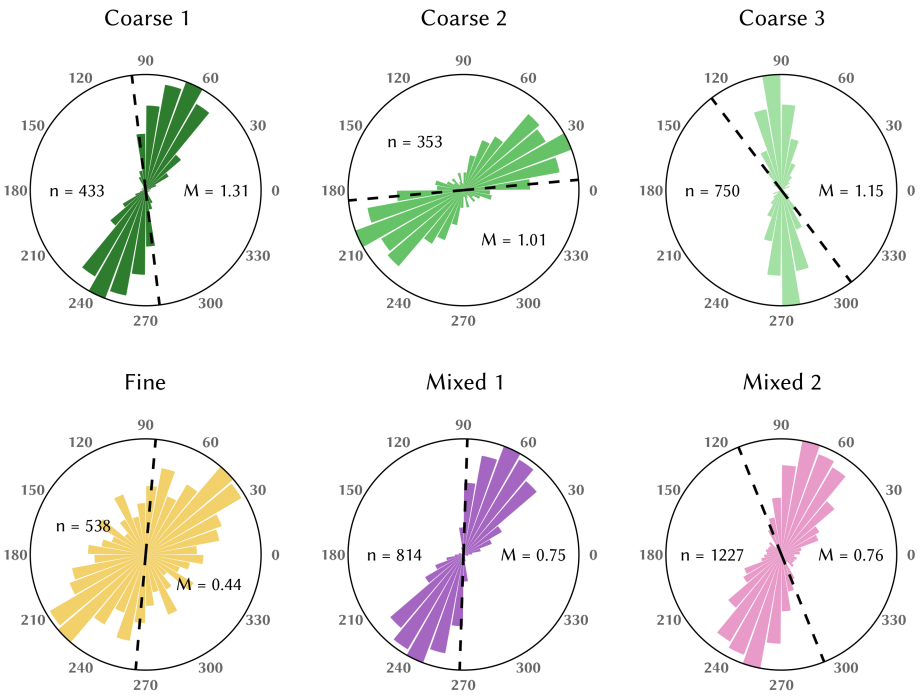

Figure 4.14 Apparent preferred orientation of vesicles in six clasts, visually classified as coarsely vesicular, finely vesicular, or mixed. Vesicles with an axial ratio ≥ 0.8 were excluded to minimise noise from near-circular vesicles. A strong preferred vesicle orientation is evident in all clasts. Dashed black lines denote the orientation angles of host clasts, which weakly align with vesicle elongations. M denotes the median vesicle size (equivalent circular diameter, mm) within each clast, with larger median sizes displaying tighter orientation clusters. Angles are measured counter-clockwise from the image horizontal; therefore, absolute orientations are arbitrary and are not comparable between clasts.

4.4 Geochemistry and rock classification

Whole-rock major and trace element composition data for a peperite clast from Hopper Quarry was obtained by XRF spectrometry. The full dataset is available in Appendix D. The results indicate the sample has undergone significant alteration and erroneously suggests a basaltic melt composition. Additionally, a high Loss on Ignition (LOI) value of 8.36 wt% reflects an abundance of volatile-rich minerals, namely chlorite and epidote. Consequently, classification or viscosity modelling using the major elements is unreliable and should be treated with caution (J.G. Fitton, personal communication, December 2, 2025).

Classification using immobile trace elements yields expected results. Use of a Th-Co discrimination diagram (Figure 4.15) (Hastie et al. 2007) identifies the clast as a high-K calc-alkaline andesite, which is consistent with established compositions of the lower BVG (e.g., McConnell et al. 2002; Millward 2004b) and indicative of a calc-alkaline magma that has assimilated K-rich pelite from the underlying Skiddaw Group. For this research, an andesite composition is assumed for further analyses.

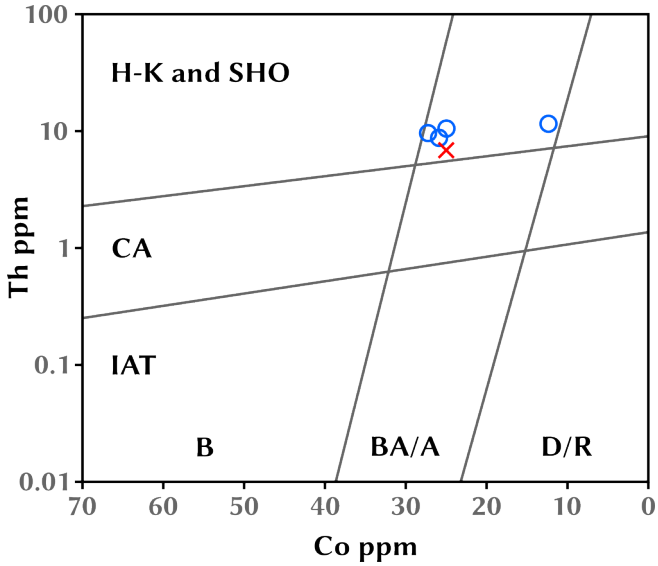

Figure 4.15 Th-Co discrimination diagram developed by Hastie et al. (2007). Red cross indicates the position of a peperite clast from Hopper Quarry, identifying the intruding magma as a high-K calc-alkaline andesite. Blue circles represent a sample of andesite dykes from the BVG (McConnell et al. 2002). **B**, basalt; **BA**/**A**, basaltic andesite and andesite; **D**/**R**, dacite and rhyolite; **IAT**, island arc tholeiite; **CA**, calc-alkaline; **H-K**, high-K calc-alkaline; **SHO**, shoshonite.

Chapter 5

Discussion

The peperite exposure at Hopper Quarry records a complex process of magma emplacement into a poorly, or unconsolidated, water-rich volcaniclastic sediment. This host sediment likely originated as subaerially erupted pyroclastics that were extensively reworked and deposited in a shallow subaqueous, likely lacustrine environment (Suthren 1977; Branney and Soper 1988; Petterson et al. 1992; Woodhall 2000; Millward 2004b). Consequently, emplacement of the at least eight andesite sills identified on Fleetwith Pike (McConnell and Kneller 1993) occurred under conditions of relatively low confining pressure, including the best exposed sill at Hopper Quarry. This discussion has two primary aims: first, to reconstruct the syn-magmatic processes of peperite genesis by interpreting textural and morphological field evidence, and second, to evaluate the application and implications of quantitative image analysis to peperite shape, size, and spacing.

5.1 Vesiculation history

Vesicles reflect the late-stage degassing history of intrusions, lavas, and pyroclasts (Shea et al. 2010; Cashman and Scheu 2015). Here, textural evidence suggests the sill was predominantly non-vesicular, or only weakly vesicular, prior to emplacement within the wet sediment. Hence, the local confining pressure remained above the volatile saturation pressure at the time of intrusion. Localised areas show potentially moderate vesicularity; image analysis has shown that the vesicle area reaches approximately 20% in the most vesicular clasts. While the main sill body is not exposed at Hopper Quarry, the adjacent exposed interior of the sill at Dubbs quarry is entirely vesicle free. This observation suggests that the interiors of all eight sills identified on Fleetwith Pike (McConnell and Kneller 1993) share a similar non-vesicular texture. Additionally, clast vesicularity is heterogeneous and shows no systematic arrangement at all outcrop scales. Strongly vesicular zones are sparse and discontinuous, and the spatial distribution of vesicle size is random, with non- and coarsely vesicular clasts often adjacent (Figure 4.3). Variability in the vesicle size distributions is interpreted to reflect locally-induced vesiculation at the sill margin during contact with the wet sediment, rather than representing full sill vesiculation prior to emplacement. In this interpretation, subsequent fragmentation and dispersal of the vesiculated sill margin accounts for the random spatial distribution and rotation of vesiculated clasts.

There was no significant post-fragmentation vesiculation; no clasts are zoned with respect to vesicularity (Doyle 2000) and some vesicles are infilled with host sediment (Figure 4.2a), which demonstrates these cavities existed during magma-sediment mingling. A post-fragmentation

vesiculation scenario would be expected to produce rim-to-core zoning textures, including the dense cooling rinds typical of breadcrust bombs (Browning et al. 2020). This reflects a competition between cooling and vesiculation timescales, with faster cooling inhibiting vesiculation at the margins (Colombier et al. 2023). In contrast, vesicle spatial distributions within Hopper Quarry clasts are homogenous or show size gradients unrelated to clast shape and margins. This supports a model of localised vesiculation at the sill margins. The presence of clasts showing a textural transition from coarsely vesicular to non-vesicular (Figure 4.3e) captures a quenched volatile saturation gradient at the magma-sediment interface, with magma closer to the margin reaching supersaturation earlier.

The described vesicle textures constrain vesiculation to a short, syn-emplacement time frame preceding fragmentation of the sill. Additionally, vesicle volume distributions (VVDs) (Figure 4.13) record this event's nucleation and coalescence history (Shea et al. 2010), with differences between the categorical clast types reflecting different growth records. While these distributions are calculated from 2D vesicle sizes without stereological correction, systematically under-representing smaller vesicles, the general trends remain indicative of a relative vesiculation history. A single stage of nucleation and growth is inferred by a distinct primary mode (Klug et al. 2002; Lautze and Houghton 2007), evidenced in the VVD of a finely vesicular clast. Coarsely vesicular clast VVDs are more complex, being highly skewed or producing a second mode. This describes a single stage of nucleation and growth with accompanying coalescence (Klug et al. 2002; Lautze and Houghton 2007); the coalesced bubbles contribute an increasing proportion of the total vesicularity. This is clearly observable at the exposure in the form of the largest vesicles within coarsely vesicular clasts (Figure 4.12c). Here, the largest vesicles display more complex, bulbous, often amoeboid shapes that indicate they are products of coalescence (Klug et al. 2002; Lautze and Houghton 2007; Gurioli et al. 2008).

Vesicles are commonly deformed, showing elongation in a strong preferred orientation within individual clasts (Figure 4.14). The preservation of this elongation indicates that bubbles had insufficient time to relax and minimise their surface energy prior to sufficient yield strength developing to counteract surface tension forces; cooling and viscosity increases were rapid enough to preserve vesicles in their deformed state (Rust et al. 2003; Lautze and Houghton 2007). Deformation is controlled by the competing stresses from shearing that deforms, and surface tension that minimises interfacial area (Rust et al. 2003), the ratio of which is the capillary number, Ca:

$$\mathrm{Ca} = \frac{a\dot{\gamma}\eta_s}{\sigma} \tag{5.1}$$

where a is the undeformed bubble radius, $\dot{\gamma}$ is the shear rate, η_s is the suspending fluid viscosity, and σ is the surface tension. This equation can be used to estimate shear rates when melt viscosity and surface tension are known. When Ca > 1, deformation forces dominate over the resisting surface tension forces. Using a median vesicle radius (a) of ≈0.5 mm for a coarsely vesicular clast and a typical silicate melt surface tension (σ) of 0.36 N m^{-1} - based on experimental studies of basalt and andesite surface tension values (Walker and Mullins 1981) - the critical shear rate ($\dot{\gamma_{crit}}$) required to reach this threshold (Ca = 1), and hence for elongation to readily occur, can be estimated using Equation 5.2.

$$\dot{\gamma}_{crit} = \frac{\mathrm{Ca}\sigma}{a\eta_s} \tag{5.2}$$

A typical liquidus andesite melt at 1000°C with a viscosity of ≈ 10^4 Pa s (Lesher and Spera 2015) has a critical shear rate of 7.2 × 10^{-2} s^{-1}. Conversely, as the melt approaches the glass transition and its viscosity approaches $10^{12.5}$ Pa s (Otterloo et al. 2015), a critical shear rate of 2.3 × 10^{-10} s^{-1}. Thus, at liquidus temperatures, moderate shear rates are required to drive elongation. However, as the melt approaches the glass transition, the required shear rate becomes negligible.

The exponential rise in viscosity effectively ”locks” the vesicles in their deformed state, as the restorative force of surface tension becomes too small to counteract even minimal late-stage strain.

Vesicle elongation is interpreted to result from either of two mechanisms: deformation by flow (Branney and Suthren 1988), or deformation of the clasts following fragmentation. Deformation by flow is supported by the model of a local vesiculation front at the sill margin, where shear rates are highest during emplacement due to steep velocity gradients. A high strain rate environment is preserved in the margins of intrusions through strain textures, such as the observed preferred orientation of vesicles (Allgood et al. 2024). The second mechanism would imply a strong correlation between the elongation orientation of the vesicles and host clast. However, only a rough, inconsistent alignment is observed (Figure 4.14) and may be coincidental. Therefore, deformation by flow is considered the more likely mechanism.

Vesiculation begins with the supersaturation of volatiles within the melt (Sparks 1978). For vesiculation to occur preferentially at the sill margins, the conditions triggering supersaturation must have been localised. Lowering ambient pressure to the volatile saturation pressure is the primary driver of vesiculation (Navon and Lyakhovsky 1998). While the vertical pressure reduction associated with magma ascent is not applicable to horizontal sill propagation, localised pressure drops can occur during the brittle failure of host rock. Magma emplacement in shallow crust is typically regarded as a dominantly brittle process (e.g., Rubin 1995); magma propagates via the opening of tensile fractures. Where near-instantaneous fracture opening outpaces magma flow, a zone of extreme low pressure is created at the fracture tip into which volatiles rapidly exsolve.

However, the intrusion of magma into wet, unconsolidated sediment is unlikely to follow a brittle emplacement scenario. Host rocks with low mechanical strength accommodate intrusion through ductile deformation around the tip of the intruding magma, often forming magma fingers (Schofield et al. 2012). Furthermore, the inclusion of water presents fluidisation of the host as an intrusion pathway (Schofield et al. 2010). Under these conditions, the magma and sediment may be physically decoupled by a persistent vapour film, which acts as a mechanical buffer. In this state, the magma may flow under low-resistance conditions more comparable to a lava, as opposed to those of a confined sill. Consequently, the mechanism of instantaneous pressure loss inherent to brittle fracture is unlikely to be a driver of vesiculation during peperite formation.

Despite the absence of a decompression mechanism during intrusion, the development of a localised vesiculation structure may still occur due to an increase in the volatile concentration of the melt. This phenomenon typically occurs via ‘second boiling’, where the growth of groundmass crystals brings the residual melt into the supersaturation field. Such vesicle layering is emphasised to be common in shallow igneous intrusions, where the steep thermal gradient at the margins facilitates the early onset of volatile exsolution relative to the insulated interior (Toramaru et al. 1996).

An alternative interpretation suggests the entire sill could have been clastic and vesiculated, with the non-vesicular interior reflecting bubble collapse or reabsorption (Saubin et al. 2016; Schipper et al. 2021; Unwin et al. 2021). Similar processes have been inferred to explain peperite domains with localised areas of low amygdule concentrations, potentially reflecting upward migration, bubble collapse, or reabsorption within a hotter part of the sill (Orth and McPhie 2003). Such a process would demand a reinterpretation of vesicle textures. Regardless, vesicles were preserved preferentially at the sill margins.

5.2 Fragmentation mechanisms

Mechanisms of magma fragmentation can be divided into magmatic fragmentation and hydromagmatic fragmentation (e.g., Wohletz 1983; Gonnermann 2015). The absence of widespread vesiculation throughout the peperite margin indicates that magmatic fragmentation, driven by exsolution and expansion of internal volatiles, played a minimal role in the fragmentation process. Such a process would preferentially produce vesicular clasts, which are not abundant in the outcrop.

Four clast-forming processes are recognised to occur during hydromagmatic fragmentation: contact-surface interaction; bulk interaction; cooling-contraction granulation, also known as quench fragmentation; and dynamic stressing, also known as autobrecciation (Kokelaar 1986). At Hopper Quarry, the blocky nature of clasts suggests fragmentation of magma in the brittle regime. Combined with closely packed and often in situ clast spatial arrangements, a brittle, non-explosive fragmentation mechanism such as cooling-contraction granulation or dynamic stressing is inferred.

Evidence of in situ fragmentation is most notable in the lower exposure, with increasing proximity to the sill, where clasts are closely packed and often framework supported (Figure 4.2d). In addition, the widespread preservation of jigsaw-fit textures (Figure 4.2) are commonly attributed to cooling-contraction granulation, especially in subaqueous settings (Hanson and Hargrove 1999; Doyle 2000; Colombier et al. 2019), although autobrecciation may also locally give rise to jigsaw-fit breccia. This architecture, along with large, angular peperite blocks, strongly resembles an autobrecciated block lava. Block lavas develop thick, brittle crusts from cooling during emplacement, which become increasingly fractured from strain accumulating during continued flow (Anderson et al. 1998). However, the upwards transition to matrix-supported clasts at Hopper Quarry distinguishes it from simple flow brecciation and indicates interaction with the host sediment. This aligns with the previously discussed emplacement mechanism through which the intrusion may be physically decoupled from the surrounding sediment, thus being comparable to a subaerial lava. Additionally, this structure is consistent with quench fragmentation models of hyaloclastite formation, in which deposits typically grade outwards from a coherent magma core into in situ closely-packed breccia and finally rotated or dispersed clasts (Otterloo et al. 2015; Colombier et al. 2019). This zonal architecture attests to a brittle, in situ fragmentation origin followed by minimal clast displacement.

The interpretation of in situ fragmentation is further supported by the spatial autocorrelation of clast size (Figure 4.11), where clasts form size-dependent clusters independent of their position on the exposure. This suggests that fragmentation intensity operated at a localised, up to metre-scale range, with domains of smaller clasts representing a higher intensity, perhaps reflecting locally elevated strain or cooling rates. The preservation of these clusters reinforces an in situ origin, as significant syn- or post-fragmentation transport would work to disrupt such domains.

From the scale-independence of clast irregularity (Figure 4.7, Figure 4.8), it is inferred that a consistent style of brittle fragmentation occurred across all clast sizes, suggesting that the magma was not subjected to substantial secondary fragmentation, such as abrasion during mingling. This is corroborated by the unimodal distributions of clast size and shape (Figure 4.5, Figure 4.6), where a single mode is inferred to show that fragmentation operated under relatively constant physical conditions. In volcanic tephra studies, such unimodal peaks are interpreted as a single primary fragmentation mechanism. Conversely, multimodality is typically ascribed to secondary fragmentation, such as by inputs from pyroclastic density currents (Eychenne et al. 2015), or to a range of contributing factors including magma heterogeneity and contributions

from a phreatomagmatic component (Costa et al. 2016). The absence of a secondary mode in the peperite clasts is interpreted as similar to the smaller tephra counterparts; the clast population represents a primary fragmentation event without subsequent modification.

Brittle fragmentation is favoured when melt viscosity and/or strain rates are high (Skilling et al. 2002). To quantify the conditions required for such brittle failure, the structural relaxation timescale of the melt (τ_r) can be considered, which governs the transition from ductile to brittle behaviour in the liquid phase. This timescale is estimated using the Maxwell relationship for a viscoelastic fluid:

$$\tau_r = \frac{\eta_r}{G} \tag{5.3}$$

where η_r is the melt viscosity and G is the shear modulus. Across a range of melt compositions and temperatures, viscosity varies over many orders of magnitude, whereas G is relatively insensitive to these changes; it can be considered a constant value of $\approx$ 10 GPa (Dingwell and Webb 1989). When the timescale of deformation is shorter than the structural relaxation timescale, the melt's mode of deformation changes from viscous to elastic. This limit corresponds to a critical strain rate of $\approx 10^{-2}/\tau_r$, above which brittle failure occurs (Papale 1999).

For a typical liquidus andesitic melt with a viscosity of $\approx 10^4$ Pa s at 1000°C (Lesher and Spera 2015), the structural relaxation timescale is a very short $\gtrapprox 10^{-6}$ s and a critical strain rate of $\gtrapprox 10^4$ s^{-1} is calculated. Such strain rates are unachievable during non-explosive interactions. However, this calculation assumes a uniform temperature across the sill, whereas the margins will have cooled rapidly on contact with the water vapour and wet sediment. As a volcanic melt approaches the glass transition, its viscosity typically reaches between 10^{12} and 10^{13} Pa s, regardless of composition (Otterloo et al. 2015). Using an average working value of $10^{12.5}$ Pa s in Equation 5.3 yields a structural relaxation timescale of $\approx$ 316 s and a critical strain rate of $\gtrapprox$ 3.16×10^{-5} s^{-1}. This low critical threshold indicates that chilled margins effectively lose the ability to relax, making brittle fragmentation inevitable even under the slow strain rates induced by dynamic stressing or cooling-contraction granulation.

Discrete populations of fine, angular clasts suspended within fully homogenised sediment point to a more energetic, though highly localised, fragmentation and dispersal (Figure 4.2). The small scale and scarcity of these features suggest limited, transient explosivity driven by unstable contact-surface interaction. In such cases, the vapour layer at the magma-sediment interface is unstable, resulting in direct contact between the magma and wet sediment; high-frequency oscillations drive fine fragmentation and turbulent mixing with the host (Kokelaar 1986). This fragmentation is very efficient, producing particles characterised by a rough, complex surface morphology due to rapid cooling (Zimanowski et al. 1991). Film instability has been attributed to both internal thermodynamic imbalances and external kinetic triggers. Internally, it has been experimentally demonstrated that instability is controlled by the wet-sediment/magma mass ratio (R_s). When $R_s < 1$, convection is insufficient to balance heat transfer, causing the vapour film to rapidly expand to a thickness beyond thermal equilibrium. The vapour then spontaneously condenses, driving an energetic collapse of the film in which liquid water impacts the magma with force (Wohletz 2002). Instability can also be forced by external kinetic factors, such as shock waves generated from hydromagmatic explosivity or seismic tremors (Zimanowski et al. 1991).

Despite these localised instabilities, explosivity was not self-perpetuating. While high hydrostatic pressure suppresses contact-surface interaction explosivity, the sills at Honister were emplaced into a shallow lacustrine environment (e.g., Branney and Soper 1988; Petterson et al. 1992; Woodhall 2000; Millward 2004b), suggesting pressure was not a limiting factor. Instead, suppression of explosivity was likely the result of multiple factors; the higher density and viscosity of the wet sediment compared to pure water would act to inhibit explosivity (White 1996), and a low volatile release rate accompanied by low magmatic flow rates could cause insufficiently

vigorous interaction to initiate self-perpetuating contact-surface interaction explosivity (Kokelaar 1986).

The presence of clasts with intricate, irregular boundaries (Figure 4.2) likely reflects small-scale changes in the propagation direction of quench fractures caused by internal heterogeneities, particularly vesicles (Doyle 2000). These clasts appear as a distribution in Figure 4.9 spanning the diagonal from low solidity/high convexity to high solidity/low convexity values. This trend shows that the morphological impact of vesicularity is scale-dependent. Where clast size is small and approaches vesicle size, margins are defined by smooth bubble walls, creating deep yet smooth embayments of high morphological roughness (low solidity/high convexity). In contrast, where clast size is significantly greater than vesicles, the vesicles impart a high textural roughness but overall clast form remains simple (low convexity/high solidity). Overall, clast morphology has been influenced by pre-existing vesicularity, forming blocky clasts bound by irregular margins rather than the typically seen planar to curviplanar margins. Highly vesicular magma is mechanically weaker and more susceptible to fine fragmentation than dense magma (Spieler et al. 2004; Otterloo et al. 2015). The breakup of vesicular material is recorded by fine clasts with vesicular, often sediment-filled margins adjacent to larger clasts with similar margins (Figure 4.2). However, the preservation of some large, vesicle-bounded clasts implies that the overall fragmentation intensity was insufficient to finely fragment all these clasts.

5.3 Clast-sediment mingling

Cooling-contraction granulation or dynamic stressing cannot account for the highly chaotic arrangement and greater dispersion of matrix-supported clasts observed higher in the exposure. This transition from an in situ brecciation to a matrix-supported domain indicates an additional process was necessary, which either acted to disperse previously fragmented clasts or simultaneously fragmented and transported the magma. One potential mechanism is small-scale hydromagmatic explosivity through contact-surface interaction or bulk interaction (e.g., Busby-Spera and White 1987; Hanson and Hargrove 1999). However, such explosive events would presumably cause significant disruption to the domain, making the widespread preservation of closely-packed peperite unlikely.

Furthermore, the observation that clast size and shape are independent of distance from the sill (Appendix D) strongly implies that the fragmentation mechanism was uniform across clasts. If explosive fragmentation was the primary driver of dispersal, a change in clast size and shape would be expected with distance from the fragmental source. Instead, morphological consistency is interpreted as a consistent mechanism of fragmentation, with subsequent dispersal of clasts. A more likely mechanism of clast dispersal is a passive displacement of previously fragmented clasts driven by fluidisation and density contrasts within a magma-sediment slurry (Skilling et al. 2002).

Fluidisation is evidenced where pockets of clasts are observed cross-cutting otherwise undeformed bedding structures in the host sediment (Figure 4.4c). In such settings, host sediment is displaced to make way for the advancing peperite. Sediment is fluidised within a vapour film at the magma-sediment interface and transported from high to low pressure, generally parallel to the interface (Kokelaar 1982). For large quantities of sediment to be mobilised, fluidisation was likely continuous, requiring persistent vapour generation. Because this process is confined to the interface, the surrounding host sediment remains largely undisturbed. For fluidisation to occur, pore water vapour must expand rapidly enough to achieve vapour velocities necessary to suspend the sediment particles (Busby-Spera and White 1987). Kokelaar (1982) placed a

depth constraint of approximately 1.6 km for the fluidisation of wet sediment under uniform heating and lithostatic pressures; below this level, the volume expansion of water near its critical point would be insufficient to cause fluidisation. Schofield et al. (2012) revised this limit under hydrostatic conditions to approximately 2.2 km, which may be a better cut-off estimate for the shallow sub-aqueous setting at Honister, though this is highly dependent on the proportions of water and wet sediment.

Density contrasts between the magma and host sediment can drive mingling (Skilling et al. 2002). High degrees of vesiculation can reduce magma density relative to the overlying wet sediment, promoting clast detachment and buoyant rise via Rayleigh-Taylor instabilities, a process observed in fluidal rhyolitic peperites (Donaire et al. 2002). This specific mechanism of vesiculation-driven buoyant rise is considered unlikely at Hopper Quarry; clasts are generally blocky to curvi-planar rather than fluidal, and vesicularity appears low. However, the buoyant rise of a bulk clast-sediment slurry may instead drive dispersal. Fluidisation can generate a magma-sediment slurry with a bulk density lower than the host sediment, facilitating the passive upward displacement of clasts (Kokelaar 1982; Busby-Spera and White 1987). Fluidisation also acts to dilate the granular host sediment, reducing yield strength and facilitating motion. The observation that peperite is often more extensively developed at the upper intrusive contacts (e.g., Brooks 1995; Doyle 2000) reinforces the idea that magma-sediment density contrasts play an important control in mingling (Skilling et al. 2002). While not a focus of this research, this observation provides a plausible explanation for the size difference between the peperitic margins at Hopper and Dubbs quarries. The restricted lower margin at Dubbs Quarry may reflect inhibited mingling, whereas the more extensive Hopper Quarry margin likely results from more extensive fluidisation and density-driven dispersion. It is important to note, however, that these features represent two distinct sills.

Further evidence for sediment fluidisation is provided by fine-grained sediment infilling both vesicles (Figure 4.2a) and fractures within clasts. These infills demonstrate the high mobility of the host sediment when fluidised by pore water vapour. The fracture fills are interpreted as momentary fluidisation caused by quenching-induced shrinkage fractures (Hanson and Wilson 1993; Brooks 1995). These fractures open abruptly, resulting in an instantaneous drop in pressure and explosive expansion as liquid pore water vaporises. This drives fluidisation of sediment into the newly created cavity (Walton and O'Sullivan 1950; Kokelaar 1982). Additionally, vesiculation of the host sediment has been observed. This is important, as it is the only unequivocal evidence for the generation of a gas phase in the sediment during peperite formation (Skilling et al. 2002).

5.4 Reconstruction of peperite formation processes

It is clear that the peperite at Hopper Quarry records a complex system of coupled, often simultaneous processes of magma emplacement, fragmentation, and mingling with a host sediment. Based on the discussed textural and quantitative data collected here, the following syn-magmatic processes are proposed, and are illustrated in Figure 5.1:

Process 1 **(Emplacement)** A poorly-vesicular andesite sill was intruded at shallow level into a wet, poorly consolidated or unconsolidated volcaniclastic sediment, parallel to the bedding. Undisturbed bedding with cross-cutting relations show that magma propagation was accommodated by the formation of a vapour film at the magma/sediment interface. This enabled displacement of the host via fluidisation, as well as ductile deformation of host bedding.

Process 2 **(Vesiculation)** Vesicle size distributions describe a single stage of vesiculation that occurred locally at the sill margins, driven by a volatile saturation gradient. Coalescence formed the largest vesicles and deformation by flow is preserved in a common elongation axis.

Process 3 **(Clast fragmentation)** Brittle fragmentation processes - cooling-contraction granulation and dynamic stressing - of the sill margins formed an initial population of blocky, in situ clasts. Clasts are angular, and often framework supported showing jigsaw-fit textures.

Process 4 **(Mingling)** Fluidisation of the sediment host at the interface in conjunction with bulk magma-sediment density contrasts facilitated clast dispersion from slight modification of jigsaw-fit textures to chaotic, matrix-supported arrangements. Transient, localised instabilities in the interface vapour film drove fine fragmentation, creating discrete clusters of fine clasts. Clast morphology remains independent of spatial location, thus mingling occured following, rather than as a result of fragmentation.

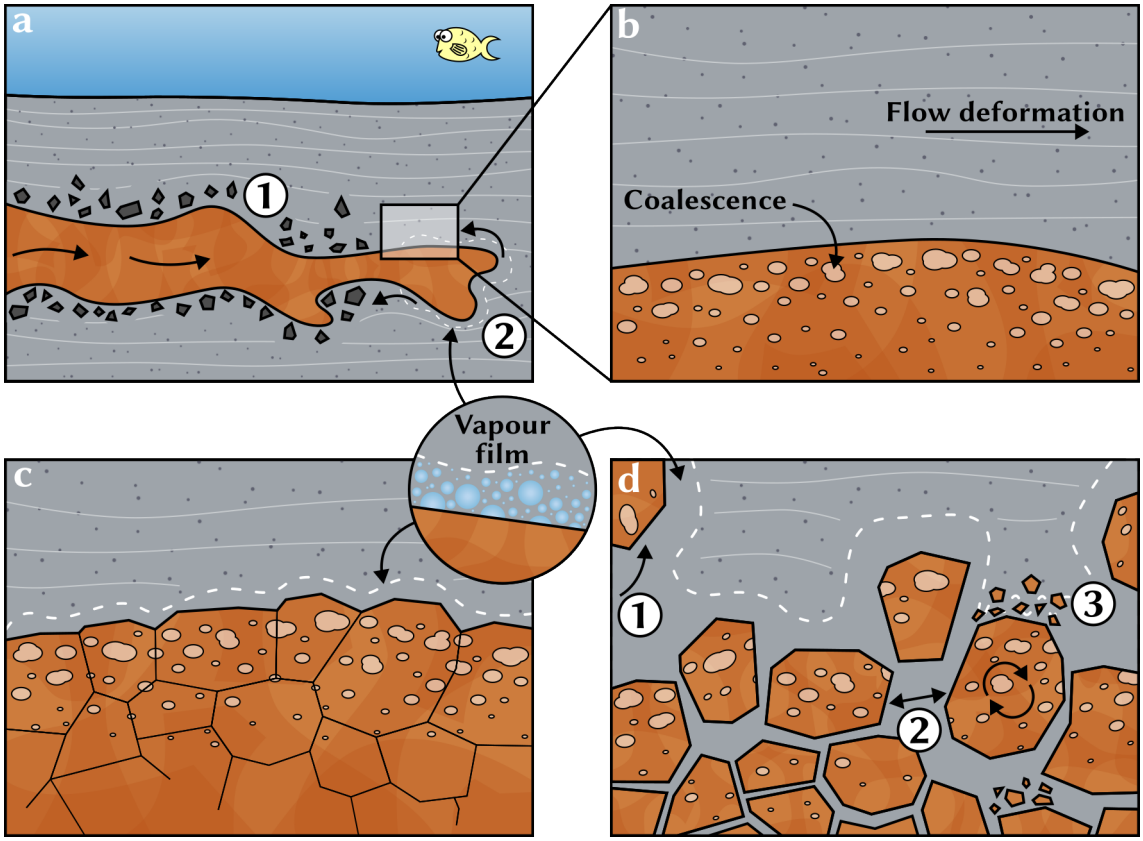

Figure 5.1 Schematic of the proposed emplacement and formation of a peperitic sill at Hopper Quarry. **(a)** Intrusion of magma into a poorly consolidated or unconsolidated, wet sediment through non-brittle processes: **(1)** ductile deformation and **(2)** fluidisation of the host. **(b)** Vesiculation of the sill margin. **(c)** Brittle fragmentation formed blocky, in situ clasts. **(d)** Clast dispersion driven by **(1)** bulk density contrasts and **(2)** fluidisation of the host. **(3)** Localised instabilities in the vapour film drove fine fragmentation of the melt.

5.5 Implications for quantitative peperite analysis and future work

This research demonstrates that the quantitative analysis of peperite deposits is viable through novel morphometric approaches utilising Structure-from-Motion (SfM) photogrammetry. SfM has been applied beyond its standard application of 3D modelling, with this study demonstrating its effectiveness in generating high-resolution, orthorectified 2D imagery suitable for the image analysis of the constituent particles within an outcrop. This workflow provides a non-destructive approach to gathering high-resolution morphological and textural data from lithified deposits beyond peperites, where the physical extraction of individual particles for analysis is impractical. Furthermore, this methodology preserves the spatial context of particles. This has allowed the analysis of spatial trends, revealing clustering patterns and morphological gradients, or lack thereof, and providing further insights into fragmentation and dispersion processes.

However, the effectiveness of this method is subject to the quality of the exposure. The great visibility of peperite clasts on relatively clean, unweathered surfaces at Hopper Quarry was critical to the success of clast delineation during image analysis. Even in this favourable setting, contrast between clasts and sediment did not allow for automated detection techniques, hence time-intensive manual outlining of clasts and vesicles was required. Consequently, while effective in this optimal setting, the application of this method to natural outcrops may be limited.

By applying these methods, this study represents the first application of 2D morphometric analysis to a peperite exposure, producing a dataset of clast shapes and distributions that serves as an initial baseline for blocky peperite. While distributions of size and shape factors constitute the primary quantitative output of this study, they remain underutilised as interpretive tools at this stage. A comprehensive discussion of the relationship between these parameters and fragmentation processes requires a larger comparative dataset across multiple localities, which are not currently available, to define the boundaries of a 'typical' peperite morphology. This is analogous to the use of particle shape comparisons in pyroclastic studies to distinguish magmatic processes (e.g., Dellino and La Volpe 1996; Büttner et al. 1999; Alfano et al. 2011); similarly, future comparisons between peperite localities will enable the identification of specific morphological and textural signatures associated with different formation processes.

Future quantitative research can leverage this dataset to assess morphological variations across peperite types. For example, this would provide a framework to distinguish between blocky and fluidal end-members (Busby-Spera and White 1987) based on distinct textural and morphological characteristics. Crucially, comparative studies should also target the upper flow breccias of block lavas. The block morphologies and fragmentation mechanisms of these sub-aerial settings closely parallel those of blocky peperite at Hopper Quarry, specifically the inferred mechanisms of brittle in situ fragmentation. Thus, determining whether shape analysis can distinguish between these different volcanic features, or if other diagnostic criteria are required, is an important next step. The integration of datasets from multiple peperite localities could lead to the development of a peperite phase diagram, where clast morphology and size distributions are used to predict specific formation mechanisms. Additionally, there is significant scope to relate quantitative characteristics such as surface area density and particle size distribution to sophisticated thermodynamic models. Finally, expanding the vesicle studies initiated in this study to include full bubble number densities, would offer further insight into the chronology of magma degassing and the relationship to fragmentation of the magma.

Chapter 6

Conclusions

Peperite exposed within quarries at Honister, Cumbria, document the intrusion and mingling of andesitic magma with wet, unconsolidated volcaniclastic sediments during the intense Ordovician volcanism of the British Isles. This study has presented an extensive analysis of one such exposure on the north-west face of Hopper Quarry, bridging traditional field observations with a novel morphometric approach to peperite analysis. By proposing a set of formation processes, this research achieves its primary aim of enhancing the understanding of peperite genesis. Central to these processes is the formation of blocky peperite through non-explosive, in situ cooling-contraction granulation of the sill margins. Following brecciation, dispersion of clasts involved fluidisation of the host sediment and was likely furthered by density contrasts between the bulk magma mixture and surrounding wet sediment. These results update the interpretation of peperite formation in the Borrowdale Volcanic Group established by Branney and Suthren (1988) through an in-depth analysis of a single exposure at Hopper Quarry, identifying non-explosive mechanisms as the primary drivers of fragmentation and dispersion. Beyond the geological model, this thesis has provided the first quantification of a peperite exposure combining outcrop scale photogrammetry with numerical image analysis:

- Structure-from-Motion photogrammetry was successfully applied at an outcrop scale to create a high-resolution orthomosaic of the peperite exposure, demonstrating that this is a viable method for morphological characterisation of lithified deposits where extraction of individual particles is not practical. This approach also preserves the spatial distributions of particles.
- A reproducible image analysis workflow was established using ImageJ macros to apply standard volcanic shape parameters to peperite clasts, as well as to quantify the size and shape distribution of internal vesicles.
- A quantitive data set was produced covering clast morphological and textural characteristics of the Hopper exposure. This serves as a baseline for an example of blocky peperite, providing abundant opportunity for comparison with future data sets of other peperite morphologies.

References

Alfano, F., C. Bonadonna, P. Delmelle, and L. Costantini (2011). "Insights on tephra settling velocity from morphological observations". In: *Journal of Volcanology and Geothermal Research* 208.3, pp. 86–98.

Allgood, C., E.W. Llewellin, M.C.S. Humphreys, S.A. Mathias, R.J. Brown, and C. Vye-Brown (2024). "Banding in the Margins of Basaltic Dykes Indicates Pulsatory Propagation During Emplacement". In: *Journal of Geophysical Research: Solid Earth* 129.4, e2023JB028007.

Anderson, S.W., E.R. Stofan, J.J. Plaut, and D.A. Crown (1998). "Block size distributions on silicic lava flow surfaces: Implications for emplacement conditions". In: *GSA Bulletin* 110.10, pp. 1258–1267.

Beddoe-Stephens, B., M.G. Petterson, D. Millward, and G.F. Marriner (1995). "Geochemical variation and magmatic cyclicity within an Ordovician continental-arc volcanic field: the lower Borrowdale Volcanic Group, English Lake District". In: *Journal of Volcanology and Geothermal Research* 65.1, pp. 81–110.

Branney, M.J. (1988). "The subaerial setting of the Ordovician Borrowdale Volcanic Group, English Lake District". In: *Journal of the Geological Society* 145.6, pp. 887–890.

Branney, M.J., B. Bonnichsen, G.D.M. Andrews, B. Ellis, T.L. Barry, and M. McCurry (2008). "'Snake River (SR)-type' volcanism at the Yellowstone hotspot track: distinctive products from unusual, high-temperature silicic super-eruptions". In: *Bulletin of Volcanology* 70.3, pp. 293–314.

Branney, M.J. and N.J. Soper (1988). "Ordovician volcano-tectonics in the English Lake District". In: *Journal of the Geological Society* 145.3, pp. 367–376.

Branney, M.J. and R.J. Suthren (1988). "High-level peperitic sills in the English Lake District: Distinction from block lavas, and implications for borrowdale volcanic group stratigraphy". In: *Geological Journal* 23, pp. 171–187.

Brooks, E.R. (1995). "Paleozoic fluidization, folding, and peperite formation, northern Sierra Nevada, California". In: *Canadian Journal of Earth Sciences* 32.3, pp. 314–324.

Browning, J., H. Tuffen, M.R. James, J. Owen, J.M. Castro, S. Halliwell, and K. Wehbe (2020). "Post-fragmentation vesiculation timescales in hydrous rhyolitic bombs from Chaitén volcano". In: *Journal of South American Earth Sciences* 104, p. 102807.

Buchanan, D.J. (1974). "A model for fuel-coolant interactions". In: *Journal of Physics D: Applied Physics* 7.10, p. 1441.

Busby-Spera, C.J. and J.D.L. White (1987). "Variation in peperite textures associated with differing host-sediment properties". In: *Bulletin of Volcanology* 49, pp. 765–776.

Büttner, R., P. Dellino, and B. Zimanowski (1999). "Identifying magma–water interaction from the surface features of ash particles". In: *Nature* 401, pp. 688–690.

Cas, R.A.F. (1992). "Submarine volcanism; eruption styles, products, and relevance to understanding the host-rock successions to volcanic-hosted massive sulfide deposits". In: *Economic Geology* 87.3, pp. 511–541.

Cashman, K.V. and B. Scheu (2015). "Magmatic Fragmentation". In: *The Encyclopedia of Volcanoes*. Ed. by H. Sigurdsson, B.F. Houghton, S.R. McNutt, H. Rymer, and J. Stix. 2nd ed. Elsevier, pp. 459–471.

Chen, S., Z. Guo, G. Pe-Piper, and B. Zhu (2013). "Late Paleozoic peperites in West Junggar, China, and how they constrain regional tectonic and palaeoenvironmental setting". In: *Gondwana Research*. Geological processes in the Early Earth 23.2, pp. 666–681.

Colombier, M., M. Manga, H. Wright, B. Bernard, R. deGraffenried, F. Cáceres, P. Samaniego, J. Vasseur, K. Jakata, P. Cook, and D.B. Dingwell (2023). "Pre-Eruptive Outgassing and Pressurization, and Post-Fragmentation Bubble Nucleation, Recorded by Vesicles in Breadcrust Bombs From Vulcanian Activity at Guagua Pichincha Volcano, Ecuador". In: *Journal of Geophysical Research: Solid Earth* 128.9.

Colombier, M., B. Scheu, U. Kueppers, S.J. Cronin, S.B. Mueller, K. Hess, F.B. Wadsworth, M. Tost, K.J. Dobson, B. Ruthensteiner, and D.B. Dingwell (2019). "In situ granulation by thermal stress during subaqueous volcanic eruptions". In: *Geology* 47.2, pp. 179–182.

Costa, A., L. Pioli, and C. Bonadonna (2016). "Assessing tephra total grain-size distribution: Insights from field data analysis". In: *Earth and Planetary Science Letters* 443, pp. 90–107.

Dadd, K.A. and N.A. Van Wagoner (2002). "Magma composition and viscosity as controls on peperite texture: an example from Passamaquoddy Bay, southeastern Canada". In: *Journal of Volcanology and Geothermal Research* 114.1, pp. 63–80.

Dellino, P. and L. La Volpe (1996). "Image processing analysis in reconstructing fragmentation and transportation mechanisms of pyroclastic deposits. The case of Monte Pilato-Rocche Rosse eruptions, Lipari (Aeolian islands, Italy)". In: *Journal of Volcanology and Geothermal Research* 71.1, pp. 13–29.

Dingwell, D.B. (1996). "Volcanic Dilemma: Flow or Blow?" In: *Science* 273.5278, pp. 1054–1055.

Dingwell, D.B. and S.L. Webb (1989). "Structural relaxation in silicate melts and non-Newtonian melt rheology in geologic processes". In: *Physics and Chemistry of Minerals* 16.5, pp. 508–516.

Donaire, T., R. Sáez, and E. Pascual (2002). "Rhyolitic globular peperites from the Aznalcóllar mining district (Iberian Pyrite Belt, Spain): physical and chemical controls". In: *Journal of Volcanology and Geothermal Research* 114.1, pp. 119–128.

Doyle, M.G. (2000). "Clast shape and textural associations in peperite as a guide to hydromagmatic interactions: Upper Permian basaltic and basaltic andesite examples from Kiama, Australia". In: *Australian Journal of Earth Sciences* 47.1, pp. 167–177.

Dullforce, T.A., D.J. Buchanan, and R.S. Peckover (1976). "Self-triggering of small-scale fuel-coolant interactions: I. Experiments". In: *Journal of Physics D: Applied Physics* 9.9, p. 1295.

Dürig, T., M.H. Bowman, J.D.L. White, A. Murch, D. Mele, A. Verolino, and P. Dellino (2018). "PARTIcle Shape ANalyzer PARTISAN – an open source tool for multi-standard two-dimensional particle morphometry analysis". In: *Annals of Geophysics* 61.6, VO671.

Eychenne, J., K. Cashman, A. Rust, and A. Durant (2015). "Impact of the lateral blast on the spatial pattern and grain size characteristics of the 18 May 1980 Mount St. Helens fallout deposit". In: *Journal of Geophysical Research: Solid Earth* 120.9, pp. 6018–6038.

Farquharson, J.I., M.R. James, and H. Tuffen (2015). "Examining rhyolite lava flow dynamics through photo-based 3D reconstructions of the 2011–2012 lava flowfield at Cordón-Caulle, Chile". In: *Journal of Volcanology and Geothermal Research* 304, pp. 336–348.

Fitton, J.G., M.F. Thirlwall, and D.J. Hughes (1982). "Volcanism in the Caledonian orogenic belt of Britain". In: *Andesites: Orogenic Andesites and Related Rocks*. Ed. by R.S. Thorpe. Wiley, pp. 611–636.

Galland, O., J.B. Spacapan, O. Rabbel, K. Mair, F.G. Soto, T. Eiken, M. Schiuma, and H.A. Leanza (2019). "Structure, emplacement mechanism and magma-flow significance of igneous fingers – Implications for sill emplacement in sedimentary basins". In: *Journal of Structural Geology* 124, pp. 120–135.

Gonnermann, H.M. (2015). "Magma Fragmentation". In: *Annual Review of Earth and Planetary Sciences* 43, pp. 431–458.

Goto, Y. and J. McPhie (1996). "A Miocene basanite peperitic dyke at Stanley, northwestern Tasmania, Australia". In: *Journal of Volcanology and Geothermal Research* 74.1, pp. 111–120.

Gurioli, L., A.J.L. Harris, B.F. Houghton, M. Polacci, and M. Ripepe (2008). "Textural and geophysical characterization of explosive basaltic activity at Villarrica volcano". In: *Journal of Geophysical Research: Solid Earth* 113 (B8).

Hajimirza, S., T.J. Jones, W.M. Moreland, H.M. Gonnermann, and T. Thordarson (2022). "Quantifying the Water-to-Melt Mass Ratio and Its Impact on Eruption Plumes During Explosive Hydromagmatic Eruptions". In: *Geochemistry, Geophysics, Geosystems* 23.5, e2021GC010160.

Hanson, R.E. and U.S. Hargrove (1999). "Processes of magma/wet sediment interaction in a large-scale Jurassic andesitic peperite complex, northern Sierra Nevada, California". In: *Bulletin of Volcanology* 60, pp. 610–626.

Hanson, R.E. and T.J. Wilson (1993). "Large-scale rhyolite peperites (Jurassic, southern Chile)". In: *Journal of Volcanology and Geothermal Research* 54.3, pp. 247–264.

Hastie, A.R., A.C. Kerr, J.A. Pearce, and S.F. Mitchell (2007). "Classification of Altered Volcanic Island Arc Rocks using Immobile Trace Elements: Development of the Th–Co Discrimination Diagram". In: *Journal of Petrology* 48.12, pp. 2341–2357.

Heap, M.J., T. Xu, and C. Chen (2014). "The influence of porosity and vesicle size on the brittle strength of volcanic rocks and magma". In: *Bulletin of Volcanology* 76.9, p. 856.

Hulme, G. (1974). "The Interpretation of Lava Flow Morphology". In: *Geophysical Journal International* 39.2, pp. 361–383.

Inman, D.L. (1952). “Measures for describing the size distribution of sediments”. In: *Journal of Sedimentary Research* 22.3, pp. 125–145.

Jerram, D.A. and H. Stollhofen (2002). “Lava–sediment interaction in desert settings; are all peperite-like textures the result of magma–water interaction?” In: *Journal of Volcanology and Geothermal Research* 114.1, pp. 231–249.

Jones, T.J., K.V. Cashman, E.J. Liu, A.C. Rust, and B. Scheu (2022). “Magma fragmentation: a perspective on emerging topics and future directions”. In: *Bulletin of Volcanology* 84.5, p. 45.

Jones, T.J., C.D. Reynolds, and S.C. Boothroyd (2019). “Fluid dynamic induced break-up during volcanic eruptions”. In: *Nature Communications* 10, p. 3828.

Kano, K.-I (1989). “Interactions between andesitic magma and poorly consolidated sediments: Examples in the neogene shirahama group, South Izu, Japan”. In: *Journal of Volcanology and Geothermal Research* 37.1, pp. 59–75.

Klug, C., K. Cashman, and C. Bacon (2002). “Structure and physical characteristics of pumice from the climactic eruption of Mount Mazama (Crater Lake), Oregon”. In: *Bulletin of Volcanology* 64.7, pp. 486–501.

Kokelaar, B.P. (1982). “Fluidization of wet sediments during the emplacement and cooling of various igneous bodies”. In: *Journal of the Geological Society* 139.1, pp. 21–33.

— (1983). “The mechanism of Surtseyan volcanism”. In: *Journal of the Geological Society* 140.6, pp. 939–944.

— (1986). “Magma-water interactions in subaqueous and emergent basaltic volcanism”. In: *Bulletin of Volcanology* 48.5, pp. 275–289.

Krumbein, W.C. (1936). “Application of logarithmic moments to size-frequency distributions of sediments”. In: *Journal of Sedimentary Research* 6.1, pp. 35–47.

Lamur, A., Y. Lavallée, F.E. Iddon, A.J. Hornby, J.E. Kendrick, F.W. von Aulock, and F.B. Wadsworth (2018). “Disclosing the temperature of columnar jointing in lavas”. In: *Nature Communications* 9.1, p. 1432.

Lautze, N.C. and B.F. Houghton (2007). “Linking variable explosion style and magma textures during 2002 at Stromboli volcano, Italy”. In: *Bulletin of Volcanology* 69.4, pp. 445–460.

Lesher, C.E. and F.J. Spera (2015). “Thermodynamic and Transport Properties of Silicate Melts and Magma”. In: *The Encyclopedia of Volcanoes*. Ed. by H. Sigurdsson, B.F. Houghton, S.R. McNutt, H. Rymer, and J. Stix. 2nd ed. Elsevier, pp. 113–141.

Liu, E.J., K.V. Cashman, and A.C. Rust (2015). “Optimising shape analysis to quantify volcanic ash morphology”. In: *GeoResJ* 8, pp. 14–30.

Maria, A. and S. Carey (2002). “Using fractal analysis to quantitatively characterize the shapes of volcanic particles”. In: *Journal of Geophysical Research: Solid Earth* 107 (B11), ECV 7–1–ECV 7–17.

Martin, U. and K. Nemeth (2007). “Blocky versus fluidal peperite textures developed in volcanic conduits, vents and crater lakes of phreatomagmatic volcanoes in Mio/Pliocene volcanic fields of Western Hungary”. In: *Journal of Volcanology and Geothermal Research* 159.1, pp. 164–178.

McBirney, A.R. and T. Murase (1970). “Factors governing the formation of pyroclastic rocks”. In: *Bulletin Volcanologique* 34.2, pp. 372–384.

McClintock, M.K and J.D.L White (2002). “Granulation of weak rock as a precursor to peperite formation: coal peperite, Coombs Hills, Antarctica”. In: *Journal of Volcanology and Geothermal Research* 114.1, pp. 205–217.

McConnell, B.J. and B.C. Kneller (1993). *The lower Borrowdale Volcanic Group of Ennerdale and upper Borrowdale*. Technical Report WA/93/38. British Geological Survey.

McConnell, B.J., J. Menuge, and J. Hertogen (2002). “Andesite petrogenesis in the Ordovician Borrowdale Volcanic Group of the English Lake District by fractionation, assimilation and mixing”. In: *Journal of The Geological Society* 159.4, pp. 417–424.

Millward, D. (2004a). *A stratigraphical framework for the upper Ordovician and Lower Devonian volcanic and intrusive rocks in the English Lake District and adjacent areas*. Research Report RR/01/07. British Geological Survey.

— (2004b). “The Caradoc volcanoes of the English Lake District”. In: *Proceedings of the Yorkshire Geological Society* 55.2, pp. 73–105.

Millward, D. and J.A. Evans (2003). “U–Pb chronology and duration of late Ordovician magmatism in the English Lake District”. In: *Journal of the Geological Society* 160.5, pp. 773–781.

Moran, P.A.P. (1948). “The Interpretation of Statistical Maps”. In: *Journal of the Royal Statistical Society Series B: Statistical Methodology* 10.2, pp. 243–251.

Navon, O. and V. Lyakhovsky (1998). “Vesiculation processes in silicic magmas”. In: *Geological Society, London, Special Publications* 145.1, pp. 27–50.

Nurfiani, D. and C. Bouvet de Maisonneuve (2018). “Furthering the investigation of eruption styles through quantitative shape analyses of volcanic ash particles”. In: *Journal of Volcanology and Geothermal Research* 354, pp. 102–114.

Orth, Karin and Jocelyn McPhie (2003). “Textures formed during emplacement and cooling of a Palaeoproterozoic, small-volume rhyolitic sill”. In: *Journal of Volcanology and Geothermal Research* 128.4, pp. 341–362.

Otterloo, J. van, R.A.F. Cas, and C.R. Scutter (2015). “The fracture behaviour of volcanic glass and relevance to quench fragmentation during formation of hyaloclastite and phreatomagmatism”. In: *Earth-Science Reviews* 151, pp. 79–116.

Papale, P. (1999). “Strain-induced magma fragmentation in explosive eruptions”. In: *Nature* 397, pp. 425–428.

Petterson, M.G., B. Beddoe-Stephens, D. Millward, and E.W. Johnson (1992). “A pre-caldera plateau-andesite field in the Borrowdale Volcanic Group of the English Lake District”. In: *Journal of the Geological Society* 149.6, pp. 889–906.

Piper, J.D.A., J.C. Stephen, and M.J. Branney (1997). “Palaeomagnetism of the Borrowdale and Eycott volcanic groups, English Lake District: Primary and secondary magnetization during a single late Ordovician polarity chron”. In: *Geological Magazine* 134.4, pp. 481–506.

Reynolds, D.L. (1954). “Fluidization as a geological process, and its bearing on the problem of intrusive granites”. In: *American Journal of Science* 252.10, pp. 577–613.

Rubin, A.M. (1995). “Propagation of Magma-Filled Cracks”. In: *Annual Review of Earth and Planetary Sciences* 23 (Volume 23, 1995), pp. 287–336.

Rust, A.C., M. Manga, and K.V. Cashman (2003). “Determining flow type, shear rate and shear stress in magmas from bubble shapes and orientations”. In: *Journal of Volcanology and Geothermal Research* 122.1, pp. 111–132.

Saubin, E., H. Tuffen, L. Gurioli, J. Owen, J.M. Castro, K. Berlo, E.M. McGowan, C.I. Schipper, and K. Wehbe (2016). “Conduit Dynamics in Transitional Rhyolitic Activity Recorded by Tuffisite Vein Textures from the 2008–2009 Chaitén Eruption”. In: *Frontiers in Earth Science* 4.

Schindelin, J., I. Arganda-Carreras, E. Frise, V. Kaynig, M. Longair, T. Pietzsch, S. Preibisch, C. Rueden, S. Saalfeld, B. Schmid, J.-Y. Tinevez, D.J. White, V. Hartenstein, K. Eliceiri, P. Tomancak, and A. Cardona (2012). “Fiji: an open-source platform for biological-image analysis”. In: *Nature Methods* 9.7, pp. 676–682.

Schipper, C.I., J.M. Castro, B.M. Kennedy, H. Tuffen, J. Whattam, F.B. Wadsworth, R. Paisley, R.H. Fitzgerald, E. Rhodes, L.N. Schaefer, P.A. Ashwell, P. Forte, G. Seropian, and B.V. Alloway (2021). “Silicic conduits as supersized tuffisites: Clastogenic influences on shifting eruption styles at Cordón Caulle volcano (Chile)”. In: *Bulletin of Volcanology* 83, p. 11.

Schofield, N.J., D.J. Brown, C. Magee, and C.T. Stevenson (2012). “Sill morphology and comparison of brittle and non-brittle emplacement mechanisms”. In: *Journal of the Geological Society* 169.2, pp. 127–141.

Schofield, N.J., C.T. Stevenson, and T. Reston (2010). “Magma fingers and host rock fluidization in the emplacement of sills”. In: *Geology* 38.1, pp. 63–66.

Scrope, G.P. (1827). *Memoir on the Geology of Central France: Including the Volcanic Formations of Auvergne, the Velay, and the Vivarsais*. London: Longman, Rees, Orme, Brown, and Green. 182 pp.

— (1858). *The Geology and Extinct Volcanos of Central France*. London: J. Murray. 258 pp.

Shea, T., B.F. Houghton, L. Gurioli, K.V. Cashman, J.E. Hammer, and B.J. Hobden (2010). “Textural studies of vesicles in volcanic rocks: An integrated methodology”. In: *Journal of Volcanology and Geothermal Research* 190.3, pp. 271–289.

Sheridan, M.F. and K.H. Wohletz (1983). “Hydrovolcanism: Basic considerations and review”. In: *Journal of Volcanology and Geothermal Research*. Explosive Volcanism 17.1, pp. 1–29.

Skilling, I.P., J.D.L. White, and J. McPhie (2002). “Peperite: A review of magma-sediment mingling”. In: *Journal of Volcanology and Geothermal Research* 114.1, pp. 1–17.

Sparks, R.S.J. (1978). “The dynamics of bubble formation and growth in magmas: A review and analysis”. In: *Journal of Volcanology and Geothermal Research* 3.1, pp. 1–37.

Spieler, O., B. Kennedy, U. Kueppers, D.B. Dingwell, B. Scheu, and J. Taddeucci (2004). “The fragmentation threshold of pyroclastic rocks”. In: *Earth and Planetary Science Letters* 226.1, pp. 139–148.

Suthren, R.J. (1977). "Volcanic and sedimentary facies of part of the Borrowdale Volcanic Group, Cumbria". PhD thesis. University of Keele.

Toramaru, A., A. Ishiwatari, M. Matsuzawa, M. Nakamura, and S. Arai (1996). "Vesicle layering in solidified intrusive magma bodies: a newly recognized type of igneous structure". In: *Bulletin of Volcanology* 58.5, pp. 393–400.

Unwin, H.E., H. Tuffen, E. Phillips, F.B. Wadsworth, and M.R. James (2021). "Pressure-Driven Opening and Filling of a Volcanic Hydrofracture Recorded by Tuffisite at Húsafell, Iceland: A Potential Seismic Source". In: *Frontiers in Earth Science* 9.

Walker, D. and O. Mullins (1981). "Surface tension of natural silicate melts from 1,200°–1,500° C and implications for melt structure". In: *Contributions to Mineralogy and Petrology* 76.4, pp. 455–462.

Walton, M.S. and R.B. O'Sullivan (1950). "The intrusive mechanisms of a clastic dike". In: *American Journal of Science* 248, pp. 1–21.

Westoby, M.J., J. Brasington, N.F. Glasser, M.J. Hambrey, and J.M. Reynolds (2012). "'Structure-from-Motion' photogrammetry: A low-cost, effective tool for geoscience applications". In: *Geomorphology* 179, pp. 300–314.

White, J.D.L. (1996). "Impure coolants and interaction dynamics of phreatomagmatic eruptions". In: *Journal of Volcanology and Geothermal Research* 74.3, pp. 155–170.

White, J.D.L., J. McPhie, and I.P. Skilling (2000). "Peperite: a useful genetic term". In: *Bulletin of Volcanology* 62.1, pp. 65–66.

Wohletz, K.H. (1983). "Mechanisms of hydrovolcanic pyroclast formation: Grain-size, scanning electron microscopy, and experimental studies". In: *Journal of Volcanology and Geothermal Research*. Explosive Volcanism 17.1, pp. 31–63.

— (1986). "Explosive magma-water interactions: Thermodynamics, explosion mechanisms, and field studies". In: *Bulletin of Volcanology* 48.5, pp. 245–264.

— (2002). "Water/magma interaction: some theory and experiments on peperite formation". In: *Journal of Volcanology and Geothermal Research* 114.1, pp. 19–35.

Wohletz, K.H., B. Zimanowski, and R. Büttner (2013). "Magma–water interactions". In: *Modeling Volcanic Processes: The Physics and Mathematics of Volcanism*. Ed. by R.M.C. Lopes, S.A. Fagents, and T.K.P. Gregg. Cambridge: Cambridge University Press, pp. 230–257.

Woodhall, D.G. (2000). *Geology of the Keswick district*. British Geological Survey Sheet Description, England and Wales, Sheet 29.

Zimanowski, B. and R. Büttner (2002). "Dynamic mingling of magma and liquefied sediments". In: *Journal of Volcanology and Geothermal Research* 114.1, pp. 37–44.

Zimanowski, B., R. Büttner, P. Dellino, J.D.L. White, and K.H. Wohletz (2015). "Magma–Water Interaction and Phreatomagmatic Fragmentation". In: *The Encyclopedia of Volcanoes*. Ed. by H. Sigurdsson, B.F. Houghton, S.R. McNutt, H. Rymer, and J. Stix. 2nd ed. Elsevier, pp. 473–484.

Zimanowski, B., R. Büttner, V. Lorenz, and H.-G. Häfele (1997). “Fragmentation of basaltic melt in the course of explosive volcanism”. In: *Journal of Geophysical Research: Solid Earth* 102 (B1), pp. 803–814.

Zimanowski, B., G. Fröhlich, and V. Lorenz (1991). “Quantitative experiments on phreatomagmatic explosions”. In: *Journal of Volcanology and Geothermal Research* 48.3, pp. 341–358.

Appendix A

Metashape Photogrammetry

This appendix provides additional detail on the Agisoft Metashape photogrammetric workflow described in Subsection 3.1.1. A total of 1072 photographs were used for the reconstruction of Hopper Quarry.

Image alignment

Using *Workflow* → *Align Photos*, a tie point cloud was produced (Figure A.1). This is a collection of points representing the same physical location in a sequence of overlapping images. The geometric relationships between the images were calculated through these points.

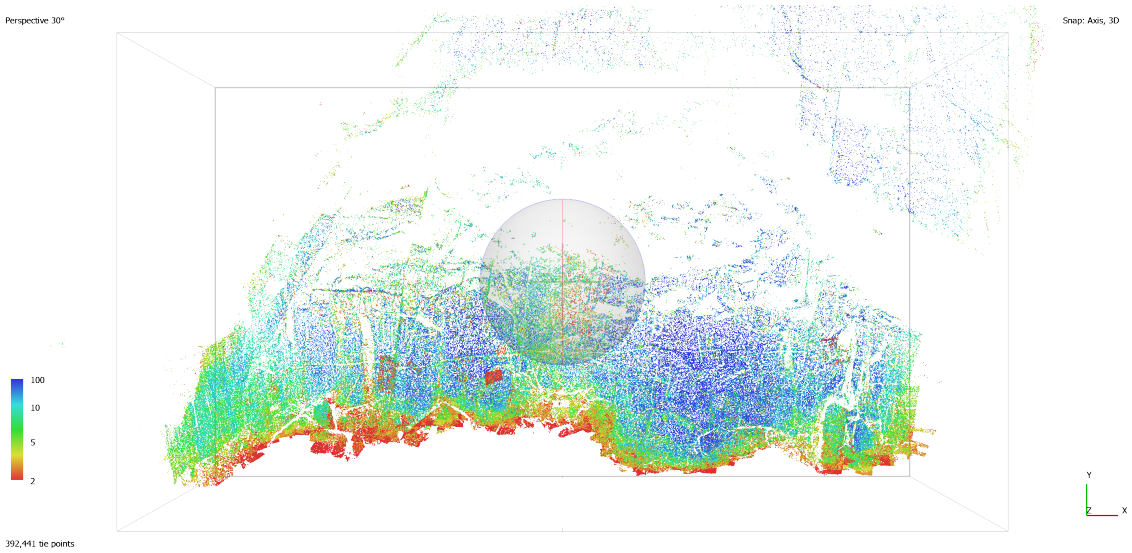

Figure A.1 Screen capture of the tie point cloud generated in Agisoft Metashape. Colour represents the number of images each tie point is visible in.

Model mesh and texture

From the tie point cloud, a model mesh was created using *Workflow* → *Build Model* (Figure A.2). This mesh was textured with the imagery using *Workflow* → *Build Texture* (Figure A.3).

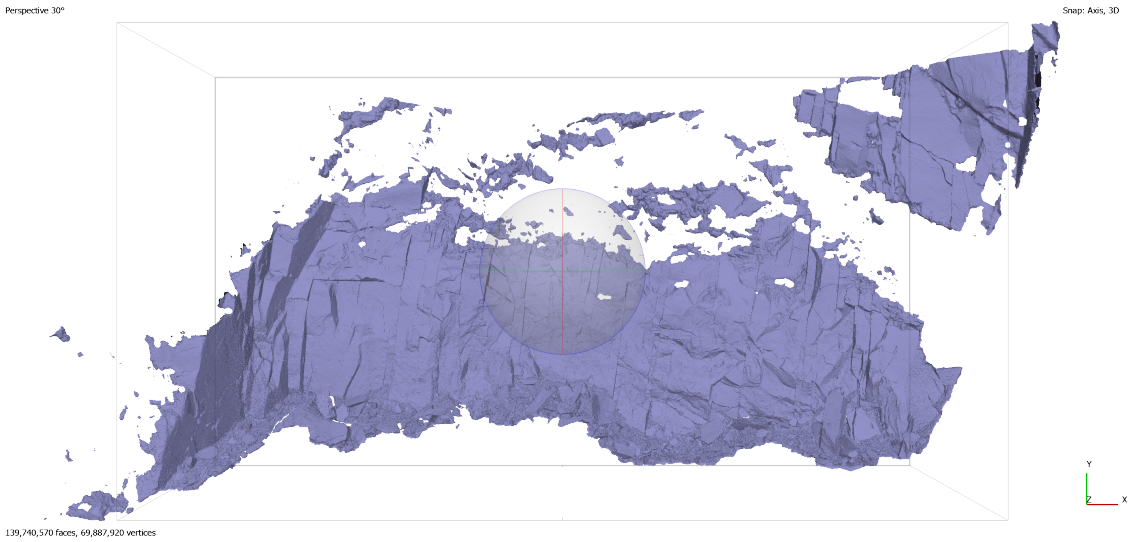

Figure A.2 A 3D model mesh of Hopper Quarry produced from a tie point cloud.

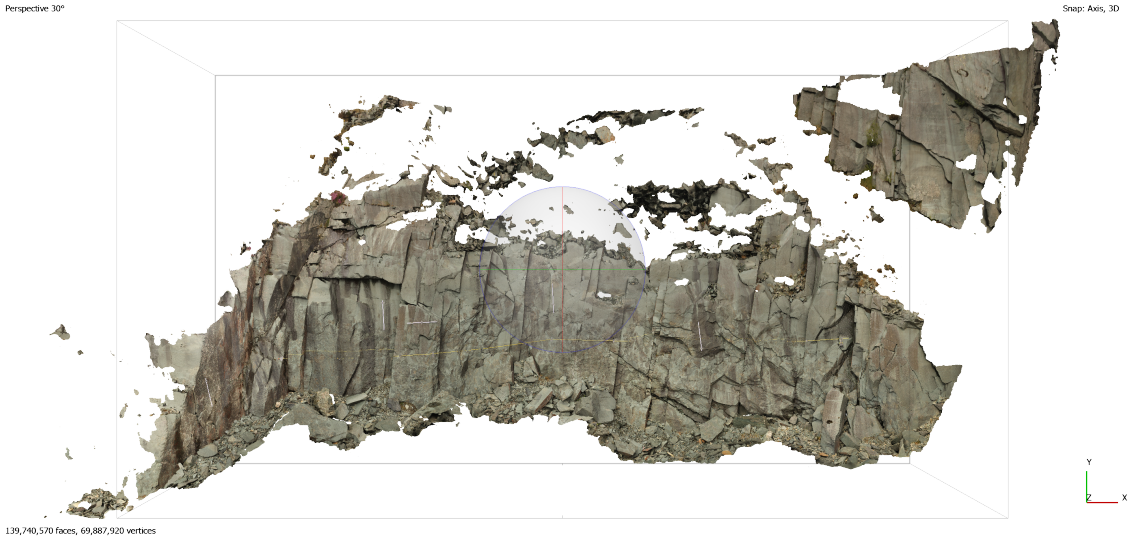

Figure A.3 Textured model of Hopper Quarry.

Scaling and orientating the model

The model was scaled by placing markers on reference objects (i.e. metre rules) and defining the known length between these markers using the *Scale Bar* function. To orientate the model, markers were distributed across the quarry face and assigned a Z-coordinate of 0. The model orientation was then updated to minimise the Z-axis error on these markers. This transformation effectively rotated the model to a best-fit plane where the quarry face aligned with the XY plane. Markers placed for scale and orientation are shown in Figure A.4.

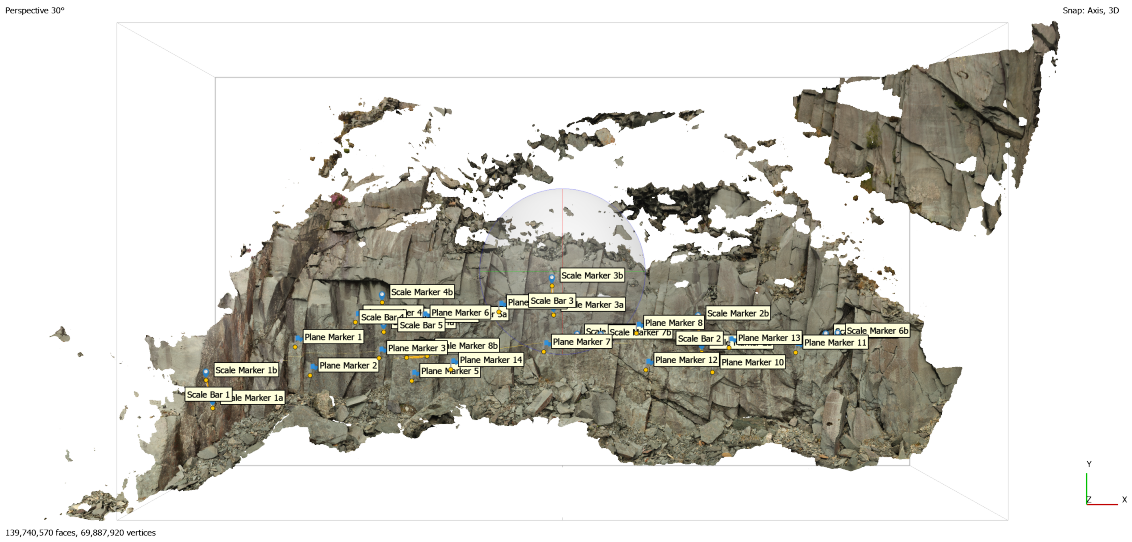

Figure A.4 Markers and scale bars placed on the 3D model of Hopper Quarry to define scale and orientation.

Orthomosaic crop

An orthomosaic of the quarry face was produced from the scaled and orientated model using *Workflow → Build Orthomosaic*. A planar projection was used to preserve true distance. This orthomosaic was cropped to the extent of visible peperite and exported as a TIFF (Figure A.5).

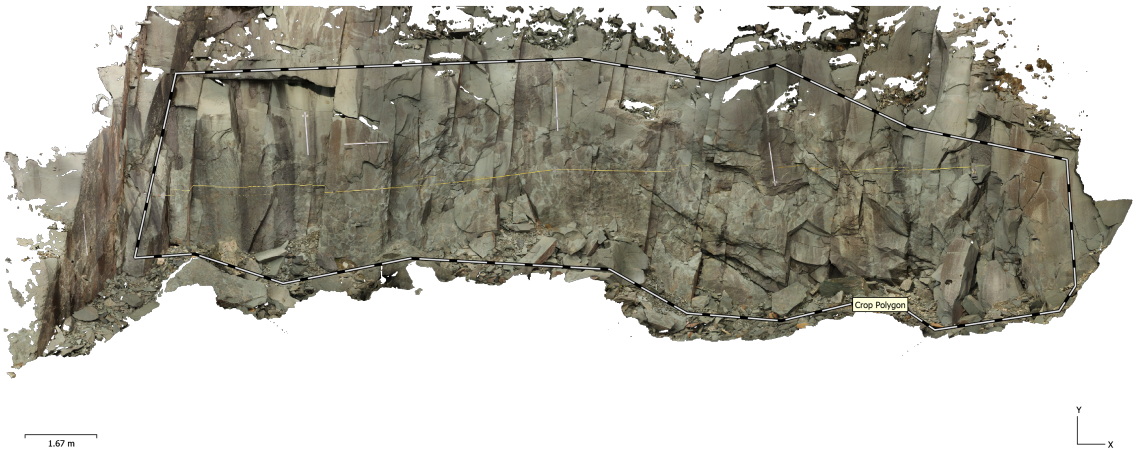

Figure A.5 Crop region of the orthomosaic exported as a TIFF.

Appendix B

Quantification of uncertainty in manual clast tracing

This appendix provides additional detail on the uncertainty analysis of clast outlines described in Subsection 3.2.1. In addition, number distributions of shape parameters separated into Groups A, which represent well-defined clast margins, and B, which represent ambiguous clast margins, are included to assess potential systematic differences related to clast outlining difficulty.

Coefficients of variation across clast metrics

Coefficients of variation were calculated for each primary measurement (Table B.1) and shape parameter (Table B.2) based on repeated clast tracings.

Table B.1 Coefficients of variation (CV) for primary measurements calculated from five repeated manual tracings of a representative clast from Group A and Group B

Symbol	Group A CV (%)	Group B CV (%)
A_{clast}	0.198	0.630
A_{ch}	0.419	0.685
P_{clast}	0.707	2.111
P_{ch}	0.337	0.438
a	0.100	0.303
b	0.105	0.858

Table B.2 Coefficients of variation (CV) for shape parameters calculated from five repeated manual tracings of a representative clast from both Group A and Group B

Shape Parameter	**Group A CV (%)**	**Group B CV (%)**
Form Factor	1.246	4.170
Solidity	0.279	0.696
Convexity	0.602	1.794
Axial Ratio	0.052	1.127

Shape parameter number distributions by group

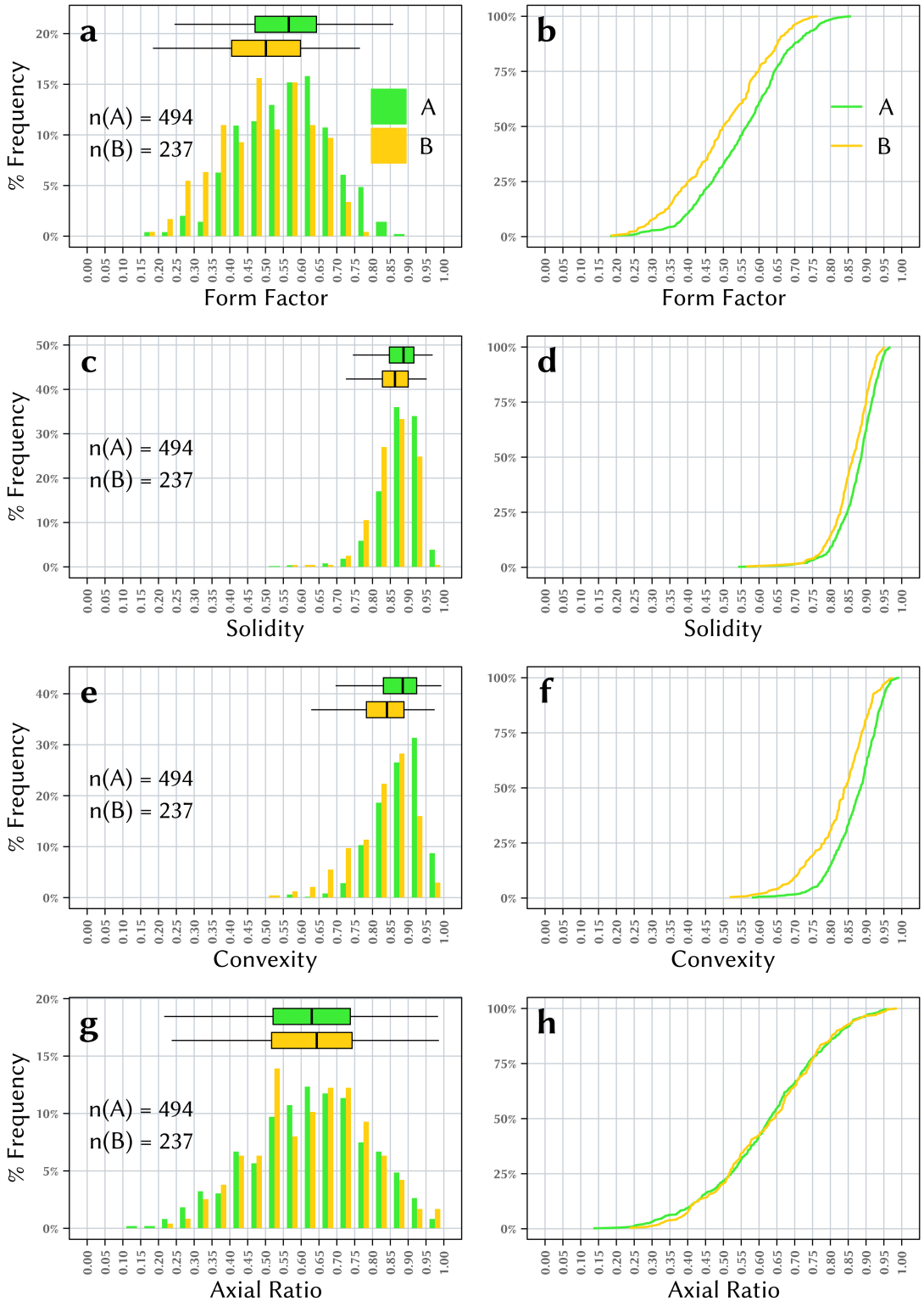

Figure B.1 Number distributions of the shape parameters form factor, solidity, convexity, and axial ratio separated into Groups A and B. Group A represents clasts with clearly defined margins. Group B represents those with more ambiguous margins. Measured from a subsample of outlined clasts from Hopper Quarry.

Appendix C

ImageJ macros

This appendix presents the ImageJ macros used for the quantitative analysis of peperite. Listing C.1 provides the macro for the size, shape, and spatial analysis of peperite clasts. The macro is based on the version provided by Liu et al. (2015), with a number of modifications for this study. Notably, the convex hull calculations were rewritten to fix unintentional merging of closely packed clast outlines. This is achieved by isolating each clast in a separate mask before calculating its convex hull. In addition, the macro automatically sets image scale, calculates centroid positions for spatial analysis, and measures mean grey values for grouping clasts. Listing C.2 calculates the area, axial ratio, and direction of elongation (elongation angle) of vesicle populations within individual peperite clasts. The elongation angle of the clast itself is also calculated for comparison with the vesicles.

Listing C.1 ImageJ macro for size, shape, and spatial analysis of peperite clasts at Hopper Quarry.

```
// Peperite clast shape analysis macro for FIJI / ImageJ

// Based on Liu, E.J., Cashman, K.V., & Rust, A.C., (2015). Optimising Shape Analysis to quantify volcanic ash morphology. GeoResJ
// Edited to fix incorrect convex hull calcutions for closely spaced clasts and include additional measurements
// It is significantly less time efficient than the original as masks must be generated for each clast

// INPUTS: a thresholded 8-bit (greyscale) image of separated clasts

// OUTPUTS: a CSV file saved on the desktop containing:
// centroid X and Y, area, perimeter, convex hull area, convex hull perimeter, form factor, solidity, convexity, axial ratio, concavity index, bounding box width and height, major axis, minor axis feret and minimum feret diameters, mean grey value

run("Set Scale...", "distance=1 known=0.000352051 unit=m global"); // Set scale: 1 pixel = 0.000352051 m

run("Set Measurements...", "area centroid perimeter bounding fit shape feret's mean redirect=None decimal=9"); // Set measurements

run("Analyze Particles...", "size=750-Infinity pixel circularity=0.00-1.00 add clear include"); // Analyse particles

n = roiManager("count");

// Arrays to store measurements
centroidX = newArray(n);
centroidY = newArray(n);
area = newArray(n);
perimeter = newArray(n);
areaCH = newArray(n);
perimeterCH = newArray(n);
FF = newArray(n);
BBX = newArray(n);
BBY = newArray(n);
major = newArray(n);
minor = newArray(n);
feret = newArray(n);
minferet = newArray(n);
meanGrey = newArray(n);

origTitle = getTitle(); // Remember original image

// Loop through each ROI (clast)
for (i=0; i<n; i++) {
    selectWindow(origTitle);
    roiManager("Select", i);

```

```
    // Measure clast
    run("Clear Results");
    run("Measure");
    centroidX[i] = getResult("X", 0);
    centroidY[i] = getResult("Y", 0);
    area[i] = getResult("Area", 0);
    perimeter[i] = getResult("Perim.", 0);
    FF[i] = getResult("Circ.", 0);
    BBX[i] = getResult("Width", 0);
    BBY[i] = getResult("Height", 0);
    major[i] = getResult("Major", 0);
    minor[i] = getResult("Minor", 0);
    feret[i] = getResult('Feret', 0);
        minferet[i] = getResult('MinFeret', 0);
    meanGrey[i] = getResult("Mean", 0);

    // Create mask
    run("Create Mask");
    maskTitle = getTitle();
    selectWindow(maskTitle);

    // Compute convex hull of only this clast
    run("Create Selection");
    run("Convex Hull");
    run("Clear Results");
    run("Measure");
    areaCH[i] = getResult("Area", 0);
    perimeterCH[i]= getResult("Perim.", 0);

    close(maskTitle); // Close mask
}

// Write results to table
run("Clear Results");
run("Select None");
for (i=0; i<n; i++) {
    setResult("X Centroid", i, centroidX[i]);
    setResult("Y Centroid", i, centroidY[i]);
    setResult("Area", i, area[i]);
    setResult("Perimeter", i, perimeter[i]);
    setResult("CH Area", i, areaCH[i]);
    setResult("CH Perimeter", i, perimeterCH[i]);
    setResult("Form Factor", i, FF[i]);
    setResult("Solidity", i, area[i]/areaCH[i]);
    setResult("Convexity", i, perimeterCH[i]/perimeter[i]);
    setResult("Axial Ratio", i, minor[i]/major[i]);
    setResult("Concavity Index", i, sqrt((pow(1-(area[i]/areaCH[i]),2)+(pow(1-(perimeterCH[i]/perimeter[i]),2)))));
    setResult("Major Axis", i, major[i]);
    setResult("Minor Axis", i, minor[i]);
    setResult("BX width", i, BBX[i]);
    setResult("BY height", i, BBY[i]);
    setResult("Feret d", i, feret[i]);
    setResult("MinFeret d", i, minferet[i]);
    setResult("Mean Grey Value", i, round(meanGrey[i]));
}
updateResults();

// Output results to CSV
path = getDirectory("home") + "Desktop/clast_measurements.csv";
saveAs("Results", path);
```

Listing C.2 ImageJ macro for the shape analysis of vesicle populations within individual peperite clasts at Hopper Quarry.

```
// Vesicle shape analysis macro for FIJI / ImageJ

// INPUTS: an 8-bit (greyscale) image where vesicles are black and inside a 50% grey clast (optional)

// OUTPUTS: CSV files saved on the desktop containing:
// 1) Vesicle metrics: area, major axis, minor axis, axial ratio, elongation angle
// 2) Clast elongation (optional)

imgName = getTitle();

// Set image scale
Dialog.create("Set scale");
Dialog.addNumber("Distance (pixels):", NaN);
Dialog.addNumber("Known distance:", NaN);
Dialog.addString("Units:", "units");
Dialog.show();

pixDist = Dialog.getNumber();
knownDist = Dialog.getNumber();
units = Dialog.getString();

run("Set Scale...", "distance=" + pixDist + " known=" + knownDist + " unit=" + units);

// VESICLE ANALYSIS //

setThreshold(0, 30); // Threshold vesicles (black) from background

run("Set Measurements...", "area fit redirect=None decimal=9"); // Set measurements

run("Analyze Particles...", "size=0-Infinity pixel circularity=0.00-1.00 add clear include"); // Analyse particles

// Arrays to store measurements
n = roiManager("count");
area = newArray(n);
major = newArray(n);
minor = newArray(n);
angle = newArray(n);

// Loop through and measure each ROI (vesicle)
for (i=0; i<n; i++) {
    roiManager("Select", i);
    run("Measure");
    area[i] = getResult("Area", i);
    major[i] = getResult("Major", i);
    minor[i] = getResult("Minor", i);
    angle[i] = getResult("Angle", i);
}

// Write results to table
run("Clear Results");
run("Select None");
for (i=0; i<n; i++) {
    setResult("Area", i, area[i]);
    setResult("Major", i, major[i]);
    setResult("Minor", i, minor[i]);
    setResult("Axial Ratio", i, minor[i]/major[i]);
    setResult("Elongation angle", i, angle[i]);
}
updateResults();

// Output results to CSV
path = getDirectory("home") + "Desktop/" + imgName + "_vesicle_measurements.csv";
saveAs("Results", path);

// CLAST ELONGATION ANGLE //

roiManager("reset");
setThreshold(0, 136); // Threshold clast (up to 50% grey) including edge vesicles
run("Analyze Particles...", "size=0-Infinity pixel circularity=0.00-1.00 add clear include");
nClast = roiManager("Count");

// Measure clast elongation angle
if (nClast == 1) {
    roiManager("Select", 0);
    run("Measure");
    angleClast = getResult("Angle", 0);
    run("Clear Results");
    setResult("Elongation angle", 0, angleClast);
    updateResults();

    // Output result to CSV
    path = getDirectory("home") + "Desktop/" + imgName + "_clast_elongation.csv";
    saveAs("Results", path);
}
else {
    showMessage("No clast detected or multiple grey regions found - skipping clast measurment");
}
```

Appendix D

Supplementary results

This appendix presents supplementary results that provide additional context to the observations reported in the main text.

Clast metrics against relative height

Figure D.1 shows scatter plots of clast size and the four SPs - FF, SLD, CVX, and AxlR - plotted against relative height. Relative height represents the vertical position of clasts on the quarry face; higher values correspond to increasing distance from the sill. Data points for all five metrics are widely distributed across relative height, with no apparent trend.

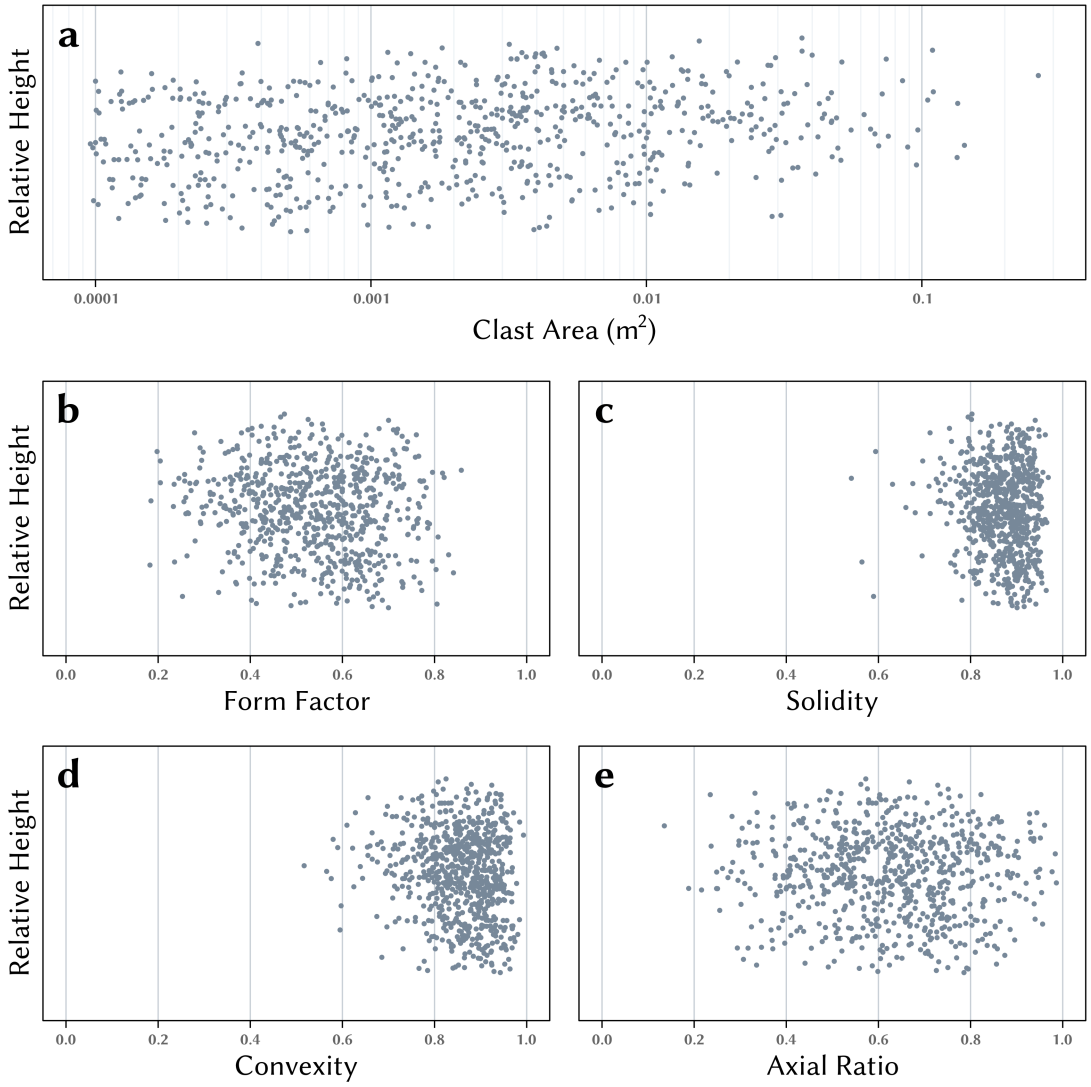

Figure D.1 Variation in clast metrics with relative height up the peperite exposure at Hopper Quarry. The plots show **(a)** clast area and four shape parameters - **(b)** form factor, **(c)** solidity, **(d)** convexity, and **(e)** axial ratio - each plotted against height.

XRF whole-rock composition

Sample preparation was performed at Durham University, with subsequent whole-rock analysis at the University of Leicester using a Rigaku ZSX PrinusIV spectrometer. Major element results are reported as oxide weight percent, recalculated to include Loss on Ignition (LOI).

Table D.1 Whole-rock major and trace element composition of the peperite clast sample from Hopper Quarry. Elements with concentrations below the lower limit of detection are displayed as <LLD.

Major elements (wt %)		*Trace elements (ppm)*			
SiO_2	48.51	**As**	<3.1	**Rb**	110.1
TiO_2	1.20	**Ba**	743.5	**Sb**	<1.3
Al_2O_3	16.98	**Ce**	47.8	**Sc**	18.0
Fe_2O_3	7.98	**Co**	24.8	**Se**	<0.2
MnO	0.24	**Cr**	101.4	**Sm**	<9.6
MgO	3.76	**Cs**	6.6	**Sn**	2.1
CaO	8.15	**Cu**	108.2	**Sr**	145.3
Na_2O	2.67	**Ga**	19.2	**Th**	7.1
K_2O	2.75	**Gd**	6.1	**Tl**	1.1
P_2O_5	0.22	**Hf**	4.9	**U**	2.2
SO_3	0.16	**La**	31.4	**V**	238.6
LOI	8.36	**Mo**	<1.1	**W**	<2.8
Total	100.98	**Nb**	17.0	**Y**	29.3
		Nd	27.1	**Yb**	2.5
		Ni	57.6	**Zn**	76.1
		Pb	13.5	**Zr**	190.1